ÉCOLE DE TECHNOLOGIE SUPÉRIEURE
UNIVERSITÉ DU QUÉBEC

THESIS PRESENTED TO
ÉCOLE DE TECHNOLOGIE SUPÉRIEURE

IN PARTIAL FULFILLMENT OF THE REQUIREMENTS FOR
A MASTER'S DEGREE IN ENVIRONMENTAL ENGINEERING
M. Eng.

BY
Gary Paul MOODY

REDUCING PARTICULATE MATTER EMISSIONS FROM RESIDENTIAL WOOD BURNING STOVES BY ELECTROSTATIC PRECIPITATION: A CFD MODELING STUDY

MONTREAL, DECEMBER 1, 2010

© Copyright 2010 reserved by Gary Moody

THIS THESIS HAS BEEN EVALUATED

BY THE FOLLOWING BOARD OF EXAMINERS

Dr. Robert Hausler, project supervisor
Département de génie de la construction à l'École de technologie supérieure

Dr. Patrice Seers, board president
Département de génie mécanique à l'École de technologie supérieure

Dr. Mathias Glaus, board member
Département de génie de la construction à l'École de technologie supérieure

THIS THESIS HAS BEEN PRESENTED AND DEFENDED

BEFORE A BOARD OF EXAMINERS AND PUBLIC

NOVEMBER 2, 2010

AT ÉCOLE DE TECHNOLOGIE SUPÉRIEURE

RÉDUCTION DES ÉMISSIONS DE PARTICULES FINES PROVENANT DES POÊLES À BOIS PAR MOYEN DE PRÉCIPITATION ÉLÉCTROSTATIQUE: UNE MODÉLISATION NUMÉRIQUE

Gary Paul MOODY

RÉSUMÉ

Les émissions de matière particulaire fine ($MP_{2.5}$) provenant des poêles à bois résidentiels sont une source majeure de pollution atmosphérique en Amérique du nord et en Europe du nord en hiver. Cette pollution a été liée à de nombreux problèmes de santé respiratoires. Nous pouvons réduire ces émissions par l'utilisation d'un précipitateur électrostatique (PES) à la sortie du tuyau d'échappement des gaz de combustion. Cette étude avait comme hypothèse qu'un tel dispositif pouvait opérer de façon efficace et ainsi contribuer à une réduction substantielle des émissions de particules fines provenant du secteur de chauffage au bois résidentiel. Un modèle numérique en 2-D d'un PES a été crée et simulé avec un logiciel commercial de mécanique des fluides numériques. Le modèle et le procédé comportaient plusieurs améliorations par rapport aux modèles trouvés dans la littérature, dont : l'utilisation d'une distribution de particules polydispersées, l'utilisation d'un écoulement semi-établi à l'admission des gaz et l'utilisation d'un modèle de chargement des particules qui tient compte des chargements par diffusion et par champs. La technique a été validée par des données expérimentales, et les valeurs de rendement correspondaient avec moins de 5% d'écart aux valeurs expérimentales. Un modèle de référence basé sur les dimensions d'un tuyau d'échappement standard de 0,15 m de diamètre a été simulé et le rendement global était de 75%. L'utilisation répandue de ce dispositif pourrait mener à une réduction de 64% des émissions de $MP_{2.5}$ provenant du secteur de chauffage au bois résidentiel au Québec. Il y a plusieurs défis opérationnels et de sécurité qui doivent être surmontés avant de pouvoir commercialiser un tel dispositif.

Mots-clés : particules fines, précipitation électrostatique, modélisation, mécanique des fluides numérique.

REDUCING PARTICULATE MATTER EMISSIONS FROM WOOD BURNING STOVES BY ELECTROSTATIC PRECIPITATION: A CFD MODELING STUDY

Gary Paul MOODY

ABSTRACT

Emissions of $PM_{2.5}$ from residential fuel wood heating appliances are a major source of winter air pollution in many parts of North America and northern Europe. This pollution has been linked to respiratory health problems. One possible method of reducing these emissions is via an electrostatic precipitator (ESP) installed at the top of the flue pipe of the appliance. This study investigated the hypothesis that such a device can operate efficiently and contribute to a significant reduction in $PM_{2.5}$ emissions from fuel wood combustion. A 2-D axisymmetric numerical model of an ESP was created and simulated using commercial computational fluid dynamics software. The model and simulation procedure included several enhancements over similar studies found in the literature such as: the use of a poly-disperse particle distribution, the use of a partially developed gas flow velocity profile and the use of a sum-of-charges particle charging model that includes diffusion and field charging mechanisms. The simulation technique was validated using experimental data and provided collection efficiency values within 5% of the experimental values. A reference model based on the dimensions of a standard flue pipe (diameter of 0,15 m) was simulated and found to have an overall collection efficiency of 75%. Based on these results, the emissions of $PM_{2.5}$ from residential fuel wood combustion in Quebec province could be reduced by 64% in one scenario. Several safety and operational issues need to be resolved before such a device can be launched commercially.

Keywords: particulate matter, simulation, electrostatic precipitation, computational fluid dynamics.

TABLE OF CONTENTS

Page

LIST OF TABLES

Page

LIST OF FIGURES

Page

LIST OF ABREVIATIONS, INITIALS AND ACRONYMS

CFD	Computational fluid dynamics
CMD	Count median diameter
CNC	Condensation nucleus counter
CWS	Canada-wide standards
DC	Direct-current
DMA	Differential mobility analyser
DPM	Discrete phase model
EPA	U.S. Environmental Protection Agency
ES	Electrostatic
GC-MS	Gas-chromatography and mass spectrometry
GUI	Graphical user interface
IARC	International Agency for Research on Cancer
ICRP	International Commission on Radiological Protection
MFP	Mean free path
MMD	Mass median diameter
NAAQS	National Ambient Air Quality Standard
NFR	Number flow rate
N-S	Navier-Stokes equations
PDE	Partial differential equation
PM	Particulate matter
$PM_{2.5}$	Fraction of PM captured with 50% efficiency at diameter 2,5 μm and greater efficiency at smaller diameters
UCM	Unresolved complex mixture
UDF	User defined function
UDS	User defined scalar
V-I	Voltage-current

LIST OF SYMBOLS AND UNITS OF MEASURE

Scalar quantities

A_{xs}	cross-sectional area of the ESP (m^2)
a	particle dielectric factor
$Be(p)$	dimensionless diffusion charging rate
b_{eq}	equivalent mobility ($m^2/V/s$)
b_{ion}	ion electrical mobility ($m^2/V/s$)
C_c	Cunningham slip correction factor
D_e	effective ion diffusivity (m^2/s)
$D_{\rho_{ion}}$	ion diffusion coefficient, ρD_e (kg/m/s)
d_p	particle diameter (m)
E_c	critical value of the electric field at the wire surface (V/m)
e	electronic charge (C)
$F(p,w)$	dimensionless field charging rate
I	total current (A)
i	current per unit length (A/m)
k	Boltzmann's constant (J/K)
m_p	particle mass (kg)
$\dot{m}_p$	particle mass flow rate (kg/s)
N	number of particle injection streams entering cell
N_p	total particle number density (m^{-3})
N_{tot}	total number of particles injected into the domain
n	particle injection index
n_c	integer number of elementary charges
n_{cap}	number of particles captured for each tracking sample
n_p	fractional number density for the given particle diameter (m^{-3})
$\dot{n}_{d_p}$	particle number flow rate for particle diameter d_p (s^{-1})
n_t	number of tries for stochastic tracking
P	static gas pressure (Pa)
p	dimensionless charge
p_0	standard pressure (101 325 Pa)
q_p	total charge on a particle (C)
R	radius of the outer cylinder (m)
r	radial distance from the wire surface (m)
r_p	particle radius (m)
r_w	wire radius (m)
S	ESP collection surface area (m^2)
S_m	mass source term ($kg/m^3/s$)
S_φ	source term for scalar variable φ
$S_{\rho_{ion}}$	ion charge density source term ($C/m^3/s$)
T_0	standard temperature (293 K)
T_p	particle temperature (K)
t	time (s)

$\overline{U}_x$	mean axial gas flow speed (m/s)
V	applied voltage at the wire (V)
V_c	cell volume (m^3)
$\dot{V}_{flow}$	volume flow rate (m^3/s)
w	dimensionless electric field magnitude

Greek symbols

Δt	particle residence time in a cell ($t_{out} - t_{in}$)
δ	non-standard temperature and pressure correction factor
ε_o	permittivity of free space (F/m)
ε_r	dielectric constant
η_{ov}	overall weighted-average collection efficiency (%)
η	collection efficiency (%)
η_{d_p}	fractional collection efficiency for particle size d_p
λ	molecular mean free path of the carrier gas (m)
μ	fluid dynamic viscosity (kg/m/s)
ρ	mass density of the flue gas (kg/m^3)
ρ_{ion}	ion charge density (C/m^3)
ρ_p	particle mass concentration (kg/m^3)
ρ_{pc}	particle charge density (C/m^3)
ρ_{tot}	total space charge density (C/m^3)
σ_g	geometric standard deviation
τ	dimensionless time
φ	FLUENT scalar variable

Vector quantities (**bold**)

$\mathbf{B}$	vector sum of body forces per unit volume (N/m^3),
$\mathbf{E}$	electrostatic field (N/C or V/m)
$\mathbf{F}_D$	aerodynamic drag force (N/m^3)
$\mathbf{F}_{ES}$	electrostatic force acting on the particle (N)
$\mathbf{F}_g$	gravitational force (N)
$\mathbf{g}$	gravitational acceleration (m/s^2)
$\mathbf{j}$	total current density (A/m^2)
$\mathbf{j}_{ion}$	ion current density (A/m^2)
$\mathbf{j}_p$	particle current density (A/m^2)
$\mathbf{U}$	gas flow velocity vector (m/s)
$\mathbf{v}$	Lagrangian particle velocity vector (m/s)
$\mathbf{V}^{cell}$	Eulerian particulate velocity vector (m/s)
$\dot{\mathbf{v}}_p$	Lagrangian particle acceleration (m/s^2)

INTRODUCTION

The current scientific consensus regarding global climate change is that urgent action is needed to reduce energy use from fossil fuels and develop alternative sources. Since wood can be classified as a renewable, carbon neutral resource (excluding harvesting and transportation) it will most likely gain in popularity over the coming years in North America and elsewhere. The reasons for this are the relative abundance of wood resources and the existing infrastructure in the form of residential fireplaces and wood stoves. It is also seen as a less costly option in the short term than installing a cleaner system such as a geothermal heat pump.

According to data published by Environment Canada (2009), wood burning for residential heating in Quebec during 2007 produced well over half of the total man-made atmospheric particulate matter (PM) emissions in the size range below 2,5 μm, commonly referred to as $PM_{2.5}$. This is the concentration of PM captured with 50% efficiency at diameter 2,5 μm and greater efficiency at smaller diameters. These $PM_{2.5}$ emissions are one of the main causes of urban smog events in large urban centres such as the greater Montreal area. Smog events are an indicator of poor air quality, with subsequent effects on the health of the population. Currently, smog alerts are issued on a regular basis during the winter in the Montreal metropolitan area. Any increase in the use of wood for residential heating will most likely lead to an increase the number of smog alerts. During a smog alert, the population is advised not to burn wood, however, with the exception of the borough of Hampstead, there are no strictly enforced municipal by-laws prohibiting wood burning during smog events in the Montreal area. In April 2009, the City of Montreal (2009) took the step of adopting a municipal by-law banning the installation of new solid fuel stoves in residential properties. This by-law may prevent the situation from worsening in the future, but it does nothing to reduce the problem caused by the estimated 50,000 wood burning stoves currently installed on the island of Montreal alone.

A particularly difficult situation is when a smog alert is issued during a very cold spell lasting several days, as occurred in Montreal during the winter of 2008/2009, when the smog episode lasted 4 days. When the demand on the electrical grid is very high, Hydro-Québec (the Quebec provincial electric utility company) issues a general request for its customers to reduce their electricity use. Since the majority of houses in Quebec are heated using electricity as a primary energy source, it is often not possible to substantially reduce consumption without compensating by using a wood burning stove in order to maintain a comfortable interior temperature. In such situations, some people are less likely to heed the smog advisory and will burn wood regardless. One solution would be to strengthen regulations and enforce them with penalties. However, such legislation would not be easy to pass on a wide scale since the population is divided on the issue. This is evidenced by the above-mentioned adoption of relatively weak measures by the City of Montreal. Even at the provincial level, the Government of Quebec (2009) has only recently implemented emissions standards based on the U.S. EPA standard.

Considering the above, there appears to be a need for a technological solution to the problem. One possibility is to reduce the emissions to acceptable levels through a suitable control device installed at the top of the chimney stack. Therefore, the main objective of this study is to develop a numerical model of a downstream emissions control device and carry out simulations to evaluate the theoretical PM collection efficiency of the device under various operating conditions. The results can then be used to draw conclusions on the feasibility of such a device, as well as to produce an estimate of the possible reduction in $PM_{2.5}$ emissions from woodstoves in the province of Quebec, Canada. The simulations will include all major physical effects on the individual particles and the interactions between them and the surrounding continuous phase (the combustion gas flow).

The review of the literature (Chapter 1) will include the environmental and health effects of PM emissions from wood combustion, followed by a review of the characteristics and properties of PM. Also included is a review of current emissions control methods, with a focus on electrostatic precipitation. Finally, some background on using Computational Fluid

Dynamics (CFD) for the simulation of electrostatic precipitators will be covered. Chapter 2 will describe the methodology used to obtain the results. The results are presented in Chapter 3, followed by a discussion of the results in Chapter 4.

CHAPTER 1

REVIEW OF THE LITERATURE

1.1 Wood fuel combustion and its effects

The use of wood as a source of fuel for heating goes back to the early beginnings of civilization. Despite the arrival of more concentrated sources of energy, wood remains to this day a much used energy source, even in industrialized nations. The reasons for the continued use of wood are both rational and sentimental. On the rational side, a wood burning stove can serve as a backup system in case of a prolonged blackout, such as occurred during the Quebec ice storm of 1998 which, according to Lecomte *et al.* (1998), was a catastrophe that produced the largest estimated insured loss ($1,4 billion) in the history of Canada. During very cold spells, the primary heating system may not be able to maintain a comfortable temperature, and the use of a secondary heating system, most often a wood stove, becomes necessary. The sentimental reasons are difficult to quantify, except to say that humans have always had an attraction to fire since it was first mastered. Also, the radiant heat produced by a wood stove is very appealing in the depths of winter.

It is instructive to consider one of the worst recorded incidences of PM in the atmosphere. This was the Great Smog of 1952 in London, U.K. The smog episode lasted for 5 days during December, and was caused by a cold, dense fog beneath a stationary temperature inversion layer, which trapped smoke released in large quantities by citizens keeping their houses warm, as well as copious industrial emissions produced by burning coal. The death toll following the event was at least 4 000 people, but according to Davis *et al.* (2002) the final death toll may have been as high as 12 000. In such acute smog episodes, it is relatively easy to determine the cause of death, but at lower PM concentrations the health effects are less clear. The effects become more subtle, such as the deterioration of existing ailments, which are less drastic but nonetheless contribute to a general degradation of health. Since then, governments have enacted clean air policies with standards to be respected in order to

prevent such events reoccurring. Luckily, oil and gas were becoming more readily available, and this went a long way to reducing pollution levels.

1.1.1 Ambient PM levels

Any discussion of air pollution and its effects on the health of the population must mention current national air quality standards. The Canada-wide Standards (CWS) are set by the Canadian Council of Ministers of the Environment (2006). The current CWS for ambient $PM_{2.5}$ is set to 30 $\mu g/m^3$ measured as an average over a 24 hour period. The achievement is to be based on the 98^{th} percentile ambient measurement annually, averaged over 3 consecutive years. The province of Quebec is not a signatory to the CWS, but it is pursuing similar standards for $PM_{2.5}$ independently. By comparison, the United States EPA (2006) has a primary 24-hour $PM_{2.5}$ National Ambient Air Quality Standard (NAAQS) standard that is met when the 3-year average of the 98^{th} percentile of the 24-hour concentration at each population-oriented station is less than or equal to 35 $\mu g/m^3$.

Air quality monitoring is usually based on measurements of the ambient concentrations of pollutants in the atmosphere over a network of sampling stations. Most sampling stations are located in areas of high population density, since this is where the majority of the man-made sources of pollutants are located and also more people are exposed, potentially causing greater health effects. Indeed, air pollution due to wood fuel burning in urban and suburban areas during winter is a well documented effect, as is shown by a study of urban air pollutants carried out in Montreal over the period 1999-2002 by Environment Canada (2004). Winter evening concentrations of $PM_{2.5}$ in the residential area of *Rivière-des-Prairies* were on average 25% higher than those measured in the downtown area. One of the conclusions of the report is that the weather conditions have a great effect on the concentrations of PM. Windy conditions will disperse the PM rapidly, but temperature inversion events will prevent the PM from dispersing and usually lead to a smog event.

1.1.2 Fuel wood use and air pollution

Statistics for 2007 from Natural Resources Canada (2010) show that 3,2% of the total housing stock in Quebec uses wood as the primary heating source, and 13,5% use wood as a secondary fuel source for residential heating. The Criteria Air Contaminants database provided by Environment Canada (2009) shows that in the province of Quebec during 2007, residential wood fuel burning was responsible for 60% (47 437 tonnes) of the total man-made emissions of $PM_{2.5}$. It is clear from these data that residential wood fuel burning is the dominant source of man-made $PM_{2.5}$ emissions in Quebec, despite the low percentage of residences that rely on wood as their primary heating source.

Similar studies carried out in site specific locations (at the city level) in North America (see Fairley, 1990 and Larson *et al.*, 2004) and in Europe (Naeher *et al.*, 2007) during the winter show that this problem is commonplace. An increase in the use of wood as a primary heating source would most likely result in an increase in $PM_{2.5}$ emissions, with an accompanying rise in negative health effects, as discussed below.

1.1.3 Health effects of wood combustion

In this section a review of the health effects will be carried out in order to justify our efforts to reduce emissions of PM into the atmosphere. Many scientific studies have been carried out to investigate the effects of PM on human health. Authors of a recent review paper on the health effects of wood smoke remark as follows:

> "The sentiment that woodsmoke, being a natural substance, must be benign to humans is still sometimes heard. It is now well established, however, that wood-burning stoves and fireplaces as well as wildland and agricultural fires emit significant quantities of known health-damaging compounds." (Naeher et al., 2007, p. 68)

A study of emissions from residential wood combustion by McDonald *et al.* (2000) identified over 350 chemical species in the combustion gases, in addition to PM. A recent assessment of the carcinogenity of household biomass fuel combustion carried out by Straif *et al.* (2006) of the International Agency for Research on Cancer (IARC) classified such activity as being: Class 2A – probably carcinogenic in humans. This includes the gaseous components as well as the particulate matter.

Concentrating on the PM emissions, it will be shown that the majority of particles emitted from wood combustion are in the submicron size range. This is a health concern since particles in this size range are not trapped by the human respiratory system, and can penetrate into the alveolar region of the lung where gas exchange takes place. Indeed, according to a particle deposition model produced by the International Commission on Radiological Protection (ICRP) and presented by Hinds (1999), the peak in particle deposition in the alveolar region occurs at a particle diameter of 0,15 μm. Submicron particles produced by wood burning have been shown by Khalil and Rasmussen (2003) to be the dominant source (80%) in ambient $PM_{2.5}$ levels at a location in Washington State, U.S.A, during winter. These particles are very mobile and can cause substantial human exposure by penetrating back into houses in the neighbourhood.

Having examined the evidence from all the main exposure, epidemiological and toxicological studies, Naeher *et al.* (2007) summarizes the health effects as follows:

> "Toxicology ... exposure to woodsmoke results in significant impacts on the respiratory immune system and at high doses can produce long-term or permanent lesions in lung tissues. ... these effects seem most strongly associated with the particle phase." (Naeher et al., 2007, p. 97)

> "Epidemiology ... exposure to the smoke from residential woodburning is associated with a variety of adverse respiratory health

> effects, which are no different in kind and, with present knowledge, show no consistent difference in magnitude of effect from other combustion-derived ambient particles." (Naeher et al., 2007, p. 98)

The review also noted that the effects of wood smoke exposure were most severe in people with pre-existing respiratory or cardiovascular conditions, especially asthma. Also at risk are young children and the elderly, whose immune systems are weaker.

1.2 Particulate emissions from wood combustion

It is important to have an understanding of the composition and physical properties of particulate matter produced during wood combustion since they differ from those of other common types of PM, such as fly ash from coal burning or motor vehicle exhaust. In this work we deal only with PM from wood combustion, unless explicitly mentioned otherwise.

1.2.1 Formation & characterization of particulate matter

According to McKendry (2002), wood is composed of cellulose (approx. 40-50% by weight), hemicelluloses (approx. 20-30% by weight) and lignin (approx. 5-30% by weight), in addition to 1-3% inorganic components and tar. The tar is composed of wax, resin, and other complex organic species produced by the living tree, while the inorganic component is mostly alkali salts, mainly of potassium.

Combustion can be defined as an exothermic oxidization at high temperature. A closer examination of the combustion of a wood log reveals three distinct processes, usually underway simultaneously, as described by Borman and Ragland (1998):

A. Drying - moisture escapes the wood through evaporation at the surface as the temperature increases;

B. Devolatilization - the volatile organic components within the wood are broken down into simpler molecules, mainly H_2, CO and CH_4, which subsequently combust in air and form flue gases;
C. Char burning - the component remaining after devolatilization is almost pure carbon, which is oxidized to form CO_2.

The devolatilization process is not 100% efficient and a range of partially oxidized organic species are formed and agglomerate to form particles that are then emitted from the wood. Other particles, usually of ultrafine diameter (less than 0,1 μm) are formed by condensation of gas phase molecules as they cool upon exiting the firebox.

During a normal operating cycle of a woodstove, PM emissions are usually highest during the start-up phase when devolatilization is occurring, and low temperature and draft lead to inefficient combustion and hence the presence of smoke. However, the absence of wood smoke does not mean that PM emissions are zero. Particulate emissions are usually at a minimum in the middle of the cycle, where little or no visible smoke is generated, but are still far from being zero. In fact, a study by Hueglin *et al.* (1997) showed that the peak in the particle number emissions during the start-up phase is $8,4 \times 10^{13}$ m^{-3} (at a particle diameter of 0,23 μm) compared to a peak of $1,6 \times 10^{13}$ m^{-3} (at a particle diameter of 0,16 μm) during the intermediate phase, which typically exhibits the lowest emissions. In addition, the shape of the particle size distribution can also vary considerably during the operating cycle.

The composition of PM from wood combustion has been experimentally determined by several recent studies using advanced instrumentation such as laser optical particle counters and differential mobility analyser/condensation nucleus counter (DMA/CNC) pair. This allows both particle size distributions and composition to be determined with accuracy, although generally there is some variability in the results from different researchers due to the large number of parameters that cannot easily be controlled (for example; wood species and humidity, woodstove type, combustion conditions, etc.).

In a study carried out by Schauer *et al.* (2001) it was determined that the particle composition was dominated by organic compounds with a small amount of elemental carbon. Compositional analysis on three different wood species yielded results as shown in Table 1.1. The organic carbon content varied from 44% to 59% of total particle mass, in addition to 1% - 3% of elemental carbon. The main trace elements were potassium, chlorine and sulphur.

Table 1.1 Compositional analysis of PM from residential wood combustion for three wood species
Data from Schauer *et al.* (2001 p. 1719)

Composition	**Wood species**		
	Eucalyptus	Oak	Pine
Organic carbon [a]	44	59	56
Elemental carbon [a]	2,6	3,2	1,4
Ionic chloride [a]	1,7	0,2	0,3
Ionic nitrate [a]	0,45	0,44	0,19
Ionic sulphate [a]	0,24	0,41	0,12
Ionic ammonium [a]	0,45	0,10	0,09
Elemental sulphur [b]	trace	0,15	trace
Elemental chlorine [b]	1,29	0,13	0,18
Elemental potassium [b]	0,81	0,65	0,28

a - measured as percentage of PM mass
b - measured by X-ray fluorescence as percentage of PM mass

Approximately 50% of the organic carbon content could be extracted and analysed by gas-chromatography and mass spectrometry (GC-MS) techniques. Since hardwood species are mostly used for heating in Quebec, we will focus on the data for oak only. In order to get a clearer picture of the PM composition, the data for oak were transformed into a pie chart of percentages of total PM mass, as seen in Figure 1.1. The main point of interest here is that most of the particulate mass is not explicitly identifiable, even using advanced analytical methods. Fully 36,5% of the PM mass is unidentified in addition to 28,2% of unextractable organics, and the authors of the study did not propose any possible species, except to say that they are highly branched and cyclic organic compounds when referring to the unresolved complex mixture (UCM). For PM produced by oak combustion, the main constituent of the identifiable organic carbon was levoglucosan (1,6-anhydro-β-D-glucose), at 9,8% of the total particulate mass.

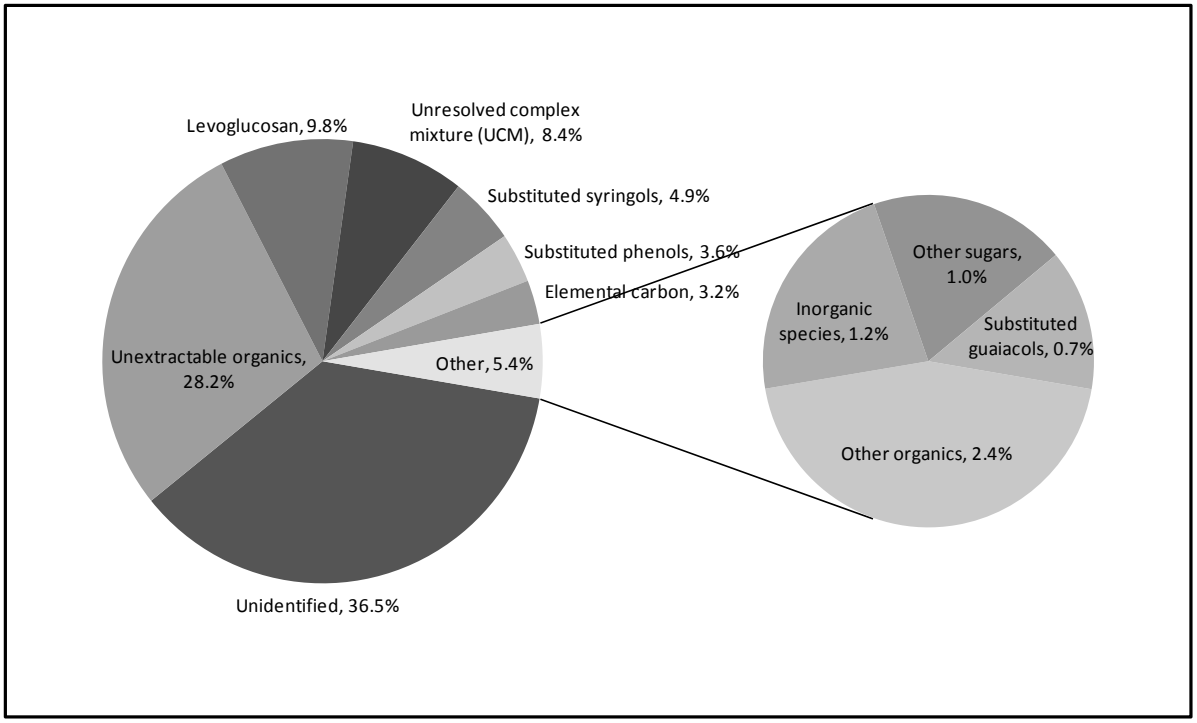

Figure 1.1 Constituents of PM from oak combustion, percentage of total PM mass.
Data from Schauer *et al.* (2001, p. 1719-1721)

Chemical analyses performed by Johansson *et al.* (2003) on the inorganic fractions of submicron particles collected during residential wood combustion showed that the main constituent elements are potassium, sulphur, chlorine and oxygen, with small amounts of sodium, magnesium and zinc. In addition, they determined that the dominant alkali compound present in the particles was potassium sulphate (K_2SO_4, 69% mass fraction), followed by potassium chloride (KCl, 24% mass fraction). They also found that the combustion of more herbaceous biomass, such as straw, hay or forest residue, resulted in the relative abundance of the alkali compounds in the particles being reversed (i.e. KCl dominant). Hence, the relative abundance of the constituent elements in the fuel determines the composition of the resulting PM.

For the purposes of our study, the most important physical property that must be determined is the particle mass density. A recent study by Coudray *et al.* (2009) used a scanning electron microscope to analyze particles produced by wood combustion in order to estimate their

mass density. They found that mass densities ranged between 1 100 and 3 000 kg/m^3 for particles of sub-micron diameter. It is likely that the particles have a relatively low melting point, since that of a β-D-glucose is 423 K at standard pressure. Hence, the particles are likely to be in a liquid form on formation, and solidify as their temperature falls while travelling in the flue gas. As for the dielectric constant (ε_r) of the particles, it is only possible to estimate a value based on the values of its known constituents. A value for the ε_r of levoglucosan could not be found in any chemical or physical reference tables, but values for sucrose, which is also a sugar, were found to range from 1,5 to 3,3.

1.2.2 Experimental data from biomass combustion

Experimental evidence suggests that most particle size distribution curves fit a lognormal distribution. Details of the lognormal distribution can be found in Wark and Warner (1981). The experimental particle data can be plotted on a log-probability chart of cumulative percent less than stated size versus logarithm particle diameter and if the distribution is lognormal, this will result in a straight line. The particle diameter with a cumulative percent of 50% equals the Count Median Diameter (CMD), and is equivalent to the geometric mean diameter (d_g) based on count. In a similar fashion, the geometric standard deviation (σ_g) can be determined from the graph by measuring the diameter at the 84th percentile ($d_{84\%}$) and using the following relation from Wark and Warner (1981):

$$\sigma_g = {d_{84\%}}\Big/{d_g} \tag{1.1}$$

The CMD and σ_g together completely define the lognormal distribution, and another useful property described by Wark and Warner (1981) is the fact that σ_g is constant for lognormal distributions based on values other than number count, for example mass and volume distributions. This property enables us to easily convert from number to mass distributions for example, using the Hatch-Choate equations originally derived by Hatch and Choate (1929). In the above case, the conversion equation is as follows:

$$\mathrm{MMD} = \mathrm{CMD}\, e^{(3 \ln^2 \sigma_g)} \quad (1.2)$$

where MMD is the Mass Median Diameter, which is always greater than or equal to the CMD. Similar equations exist for conversion between CMD and various different diameters, such as the mean and modal diameters. In order to put the difference between the CMD and the MMD into perspective, consider that in a typical sample of atmospheric particulate, the particles in the size range 0-1 μm constitute only 3% of the total sample mass, but make up 99,99% of the number of particles, according to Wark and Warner (1981, p. 146).

Several experimental studies have been carried out to better characterize the emissions from wood burning stoves of different types, including residential and industrial scale appliances. Generally, these studies focus on the different chemical species produced during wood combustion, but also include some data on the PM emissions. In two separate studies carried out by Johansson *et al.* (2003) and Johansson *et al.* (2004) values for the CMD were found to be in the submicron range from 0,1 to 0,3 μm for a range of different types of wood burning appliances, including both old and modern wood stoves and pellet stoves. Hedberg *et al.* (2002) measured a MMD of 0,5 μm from burning birch wood logs in a commercial wood stove. Kleeman, Schauer and Cass (1999) measured particle mass distributions from burning several types of wood (pine, oak and eucalyptus) and found similar profiles with MMDs ranging from 0,1 to 0,2 μm. Finally, a study by Hueglin *et al.* (1997) measured the particle number distributions from three phases of wood burning and showed that the greatest emissions were during the start-up phase, with a CMD of 0,24 μm. The lowest emissions were during the intermediate phase, with a CMD of 0,16 μm. In summary, it is clear that there is wide scientific consensus that the PM emissions from wood combustion are mainly in the sub-micron range (diameters ranging from 0,1 to 1 μm).

Apart from the particle size distributions, it is also important to measure the particle emissions rate. The emissions rates are also influenced by many variables, as for the size distributions. The emissions rate determined from the study by Schauer *et al.* (2001) for oak combustion is 5,1±0,5 grams of PM emitted per kilogram of wood burned (g/kg). The study

by Hedberg *et al.* (2002) for the combustion of birch wood obtained an average emission rate of 1,3 g/kg. McDonald *et al.* (2000) obtained emission rates from 2,3 to 7,2 g/kg for mixed hardwood and oak combustion in wood stoves under a range of operating conditions. Based on these results, an average emission rate for hardwoods is calculated as 4,0 g/kg. The average burn rate for these tests was calculated to be 4,6 kg/h. The average emission rate in terms of grams per hour is a more useful measure, and is calculated to be 15,7 g/h. It is interesting to note that this emissions rate is well above the maximum rate required for U.S EPA (1988) stove certification (7,5 g/h).

1.2.3 Particulate emissions control methods

Currently the most widely explored and applied means of reducing PM emissions from wood stoves focus on increasing the efficiency of the combustion process in the stove itself. The most popular methods for achieving this fall into two categories: catalytic and non-catalytic. The simplest method is non-catalytic, which achieves increased combustion efficiency through the addition of three modifications to the traditional wood stove. These are the addition of insulating bricks in the firebox, an increased baffle size, and the introduction of pre-heated secondary air into the top part of the firebox. Catalytic stoves on the other hand, have a more complex design based on the addition of a catalyst-coated structure through which the exhaust gases flow and burn much of the smoke, making them more efficient and hence less polluting than non-catalytic stoves. However, the catalytic stoves are significantly more expensive, and the catalyst unit degrades relatively quickly with time.

The main problem with the focus on improving combustion efficiency is that existing stoves cannot easily be retrofitted with the above technologies, and the existing stove must be replaced altogether. The province of Quebec now requires by law that new/replacement installations meet the U.S. EPA (1988) standard. Many wood stoves now on the market have certified emissions rates under 4,0 g/h, however the lifespan of a wood stove can be up to 30 years, so existing older and more polluting stoves will continue to be used and to pollute the air more than new stoves for many years to come.

Another important factor is that despite the technological advances in stove design mentioned above, the actual PM emissions produced depend on the user following the basic rules of wood burning. These are always provided in the user guide for new stoves, and the most important one according to the Canada Mortgage and Housing Corporation (2008) is to burn only well seasoned (dry) split hardwood. It is necessary to follow the operating instructions carefully, as incorrect operation can greatly increase PM emissions. However, it is human nature not to follow instructions, and one can conclude that in general the actual emissions from any given stove will be greater than those obtained under optimal conditions during certification (as evidenced by the experimental results mentioned in section 1.2.2).

Taking the above facts into consideration, it is clear that even the most advanced wood stove can be made to operate inefficiently through user misuse. Therefore, our hypothesis is that if an emissions control device could be installed downstream from the stove itself (at the chimney exit) emission rates could theoretically be controlled regardless of how the stove is operated. Existing installations could simply be retrofitted at the chimney exit and could in theory be applied to all existing stove installations regardless of type.

There are currently no known widely available commercial means for particulate emissions control downstream from residential wood stoves in North America. The main emissions control methods discussed in this section are listed in Table 1.2. They are all used by industry, most notably by coal-fired power stations and the cement manufacturing industry, where very large quantities of PM are produced and must be efficiently controlled to prevent widespread environmental problems. Most often, several different control devices are installed in combination. It must be noted that the scale of these control devices is also industrial, and much of the engineering challenge lies in reducing the scale of these devices to the residential scale while retaining their high collection efficiencies.

Mechanical filtration using closely spaced fibres to capture particles is the most common type of filtration for particle sampling. Modern filter designs are highly effective in certain applications. The wide range of different types of filter materials available, each with its own

characteristic properties and performance, are one of the reasons for their popularity. Industrial filtration takes the form of a so-called baghouse, large house-sized chambers containing the filter material.

Table 1.2 Summary table of emissions control devices and characteristics
Adapted from Vallero (2008)

Type	Collection efficiency (range 0,1-1,0 µm)	Maximum temperature (K)	Pressure drop (Pa)
Settling chamber	very low	n/a	n/a
Cyclone	very low	673	490-1 180
Mechanical filter	low	353-563	980-1 960
Dry scrubber	low	773	980
Wet scrubber (Venturi)	medium	813	8 600
Electrostatic precipitator	high	673	100

There are however several reasons why filtration is never used as the primary PM control device in coal fired utilities. Firstly, placing a filter into the flue gas flow creates an obstruction to the flow. This in turn causes a pressure drop on either side of the filter, which is proportional to the thickness of the filter. Pressure drop therefore restricts the flow, and if the pressure drop is greater than the normal pressure difference causing the flow, then the flow will be completely obstructed. For obvious reasons, this cannot be allowed to happen in a residential chimney, where the draft created during operation of the wood stove is quite small at less than 100 Pa for a standard residential chimney stack, as calculated using the formula by Perry and Green (1984).

Mechanical filters tend to clog up with use, causing an increase in pressure drop and a decrease in efficiency over time. Regular replacement of filters is normally required in industrial applications, making them unattractive options for residential use. Most common filters are unsuited for use in extreme conditions, such as those that exist in chimney stacks (high temperature, presence of corrosive chemical species, etc.). Therefore, the performance of filters in such conditions is likely to be unsatisfactory. Based on the above facts,

mechanical filtration is not deemed to be a suitable PM control device for residential applications.

Another common control device is the cyclone, which uses the principle of centrifugal separation of particles from the gas flow. Cyclones are systematically installed at coal-fired utilities, and they act as cost efficient pre-cleaners. In a cyclone, the dirty gas enters through a horizontal duct at the top of a vertical cylinder. The gas is forced into a helical downwards motion at first, forming a vortex, the particles are forced outwards to the cyclone walls through the centrifugal force and their own inertia. The particles slide down the walls and are collected at the bottom of the device. Detailed analyses of cyclone collection performance have been carried out in order to maximize their efficiencies. The main result presented by Wark and Warner (1981) is as follows:

$$\eta \propto \frac{\text{centrifugal force}}{\text{drag force}} \propto \frac{v_p \rho_p d_p^2}{R_c \mu_g} \tag{1.3}$$

where η is the collection efficiency, v_p is the particle velocity, ρ_p is the particle mass density, R_c is the cyclone radius and μ_g is the gas viscosity. The collection efficiency is proportional to the square of the particle diameter so that efficiencies are low for small particles. A low inlet gas/particle velocity, as would be the case for a wood stove flue gas, means low cyclone collection efficiency. In addition, efficiency decreases with increasing gas viscosity, as is the case for high temperature flue gas. From this, it is clear that cyclones are not well suited to collect submicron particles, due mainly to the low inertia of such particles.

Next there are scrubbers, which are devices that pass the flue gases through some filtering medium, which can be solid or liquid, hence the terms wet or dry scrubber. According to the description by Vallero (2008), in a wet scrubber the particle-laden gas stream passes through a liquid spray in order to capture the particles in the liquid. The captured particles are then removed from the gas flow on a collecting surface, which can be a type of inertial collector. The dry scrubber passes the flue gas through a bed of solid matter, such as fine gravel, that is continuously re-circulated by an external mechanism. This matter acts as a filter, cleaning the

gas is a similar fashion, but without the problem of clogging. Both wet and dry scrubbers are large, complex devices, which require frequent maintenance and consume power and water (wet scrubber). It is clear that these devices are unsuitable for adaptation to a smaller scale for residential use.

As can be seen from Table 1.2, the electrostatic precipitator (ESP) is the only emissions control device able to capture submicron particles with high efficiency and a low pressure drop from a hot flue gas. It is for these reasons that ESPs have been in use for many decades in essentially all the worlds coal-fired utilities. Industrial ESPs have reached a high degree of sophistication in their design and operation, and they are also large and costly devices. Nonetheless, their operational characteristics mentioned above theoretically make them well suited for use in small scale residential applications.

1.2.4 Electrostatic precipitators

Electrostatic precipitators exist in a wide range of different geometries and scales, from tens of millimetres to tens of meters in size. Some devices are designed only to charge particles and not to capture them hence they have slightly different designs. But one thing they all have in common is a corona discharge region that generates an ion flux that subsequently charges the particles. The most common geometries are the wire-plate and the wire-cylinder.

According to Hinds (1999) in an industrial ESP the particle-laden flue gas is passed through a series of vertical metal collector plates. A high direct-current (DC) voltage is applied to thin vertical wires hung between pairs of grounded collector plates (a wire-plate geometry). The high voltage causes an intense non-uniform electrostatic field to be generated between the wire and plate. In the initial stage, the uncharged particles gain electrical charge through bombardment by ions generated in a thin corona discharge region surrounding the wires. The corona discharge region is essentially a highly ionised gas referred to as plasma. The corona discharge occurs when the electric field strength at the wire surface is above a critical value required to ionise the surrounding air. This creates a self sustaining avalanche of ions and

electrons, which then move with high velocity along the electric field lines towards their opposite polarity source or sink. In the case of a negative wire polarity, the electrons move out of the corona discharge region and attach themselves to electronegative gas (O_2) molecules in air to form high concentrations of negative ions. The particles then gain negative charge as they move through this negative ion flow. If the inner wire polarity is positive, then high concentrations of positive ions will flow to the grounded plate, and the resulting charge on the particles will be positive. This mechanism, first described by Pauthenier and Moreau-Hanot (1932), is known as field charging, and according to Hinds (1999) is the dominant charging mechanism for particles greater than 1 μm in diameter.

The ion generation mechanisms are actually quite complex and very different for positive and negative corona, and this is in itself an entire domain of research. However, for the purposes of this study, the above description is sufficient. All coronas generate ozone from oxygen in the air. Industrial ESPs are usually operated at negative potential since higher voltages can be attained, and hence higher efficiencies, however this results in increased ozone generation. According to Hinds (1999), negative corona produces about ten times as much ozone as positive corona. Obviously this is an important consideration, since ozone is itself a pollutant at low altitudes.

A second mechanism for particle charging in the presence of a unipolar ion flux such as that created by corona discharge is known as diffusion charging, as described by Fuchs (1947). Here, the particles become charged by random collisions with ions due to their Brownian motion. Again according to Hinds (1999), diffusion charging is the dominant mechanism for particles of diameter less than 0,2 μm and a transition zone exists between 0,2 and 1 μm, where both field and diffusion charging mechanisms are operating. Any model dealing with particles in the sub-micron size range must take both mechanisms into account. Creating a unified model for field and diffusion charging in the transition zone has been the subject of much research in this field. However, an analysis of particle charging models carried out by Lawless (1996) determined that a simple sum of charges approach to estimating the total charge on a particle in the transition zone resulted in values which were comparable with

experimental data obtained by Fjeld, Gauntt and McFarland (1983) and Kirsch and Zagnit'ko (1990), among others. The sum of charges model presented by Lawless provides a basis for calculating the total charge on a particle of a given diameter in the simulation. Readers are referred to Chapter 2 for more details of this model.

In the second phase, the charged particles are accelerated towards the collector plates by the electrostatic force on them. Bernstein and Crowe (1981) showed that the overall collection efficiency of the device depends on a number of parameters, including: the applied E-field, the particle charge, the gas flow properties and the collector geometry. Finally, the accumulated dust is removed by rapping the collector plates occasionally.

Most current research on ESPs is focussed on large-scale industrial cleaning devices for coal-fired utilities. Many different designs have been tested to try and maximise the collection efficiency and minimize operating cost. In a recent review of ESP research, Jaworek *et al.* (2007) noted that collection efficiencies reached a minimum (70-80%) in the transition zone between 0,1 and 1 μm. This is known as the penetration window, and is due to reduced charge and increasing mobility of the particle with a decrease in size. Hence finding ways to increase efficiencies in the transition zone is the goal of current and future research in industrial ESP design. The existence of this efficiency trough in the transition zone described above (where particle collection is particularly difficult) is of great importance for this study since, as we have seen in the preceding sections, the peak emission of wood combustion particles often lies in the transition zone, and these are the particles that can penetrate furthest into the alveolar region of the lung and have damaging health effects.

An experimental and theoretical study of small scale ESP performance in the ultra-fine and submicron size range was carried out by Zhuang *et al.* (2000), where they built and tested a wire-cylinder type ESP with a diameter of 0,03 m and length of 0,15 m. Artificial aerosols (including NaCl, SiO_2 and Al_2O_3) were used to simulate particles at concentrations comparable to emissions from wood combustion. They measured collection efficiency as a function of particle diameter and found that a maximum efficiency of 80% was reached at a

diameter of 0,085 μm for alumina particles under a given set of charging conditions and flow field parameters.

Only one experimental evaluation of a prototype ESP specifically designed for reducing PM emissions from residential heating appliances could be found in the literature, namely that by Schmatloch and Rauch (2005). This device was tested using emissions from a commercially available pellet boiler. A modified wire-cylinder geometry was used with a positive ionisation voltage of up to 20 kV, resulting in an overall collection efficiency of nearly 90% (by particle number) over a particle size range from 0,02 to 0,6 μm. The details of several important parameters were absent from the paper, including the gas flow velocity.

1.3 Simulation techniques

Experimental setups for PM measurement from wood stoves are often complex, requiring the use of a range of sophisticated sampling and measuring instruments that may not readily be available to researchers. Although numerical simulations cannot replace an experimental study, they do allow different models and parameters to be tested in a relatively short space of time and within a limited budget. The results can then be compared with experiment to assess the validity of the simulation model. Once it has been shown to agree with experiment with some degree of accuracy, it can be used to simulate any number of different setups.

In order to get a good understanding of the operation of an ESP, it is necessary to understand the physical mechanisms at work in the device. The theory is relatively straightforward for particle motion in a vacuum, but is more complicated when we model a real-world situation, such as a particle moving in a turbulent gas flow. Simulation techniques in such situations are limited to numerical techniques that make use of the speed and memory of modern computers. The field of CFD has grown in parallel with the development of the microprocessor, and has become the standard for modeling in the scientific and engineering fields.

1.3.1 Computational Fluid Dynamics overview

The field of fluid dynamics is based on the following three fundamental physical principles:

A. Conservation of mass (continuity equation)
B. Conservation of energy (energy equation)
C. Conservation of momentum (momentum equation)

The set of equations describing these principles are known as the Navier-Stokes (N-S) equations, the details of which can be found in any book on fluid dynamics, such as that by Hughes and Brighton (1999). These equations are non-linear partial differential equations (PDE), which cannot be solved analytically for most real-world problems. This problem is solved through the use of CFD methods. Commercial CFD software packages are generally very versatile and user friendly and can be put to use on any number of problems and provides rapid results, without the need for major programming and intimate knowledge of the N-S equations involved.

The aim of CFD is to replace the N-S equations with numerical equivalents and use the power of the microprocessor to advance the numerical equivalents step by step in a series of iterations in time until a final numerical description (or solution) of the principal flow-field variables (velocity, pressure, turbulence, temperature, etc.) is obtained. Thus, any solution obtained using CFD is only an approximation, although it can be a very good approximation, depending on the desired precision. It is not the intention of this work to delve into the details of CFD and the reader is referred to Wendt (1995) for details on the basic theory.

1.3.2 CFD simulation of an ESP

Initial attempts to simulate the operation of an ESP using a CFD approach involved the use of numerical methods custom written for the purpose. For example Watanabe (1989) proposed a method for calculating individual fly-ash particle trajectories in a wire-plate ESP. Such custom methods lack the power and flexibility of a commercial CFD package, but

nonetheless produced a basic working model in general agreement with the experimental data. Since then, a number of similar simulations have been presented in the literature, with the more complete models using CFD numerical methods to calculate the turbulent gas flow field, the electric field, and the ion current including their effects on particle trajectories.

A simulation carried out by Choi and Fletcher (1997) made use of a commercial CFD package and took into account the effect of the particle space charge on the electric field and ion current. They concluded that in cases where there is a high mass loading of submicron charged particles, effects on the ion current and E-field distributions are significant and must not be neglected. The effect of a space charge is to restrict the ion current in the ESP resulting in a reduction in the collection efficiency. In a more recent simulation based on the above technique, Skodras *et al.* (2006) used a commercial CFD package to model an industrial wire-plate ESP over the particle size range 2 – 10 μm. It was found that collection efficiency for the smallest (2 μm) particles was less than 50%. They concluded that, for a given particle diameter, the inlet velocity and the electrical potential of the inner wire are the main factors that influence collection efficiency.

In summary, we will attempt to build a model and carry out a simulation based on the above works, and apply it to an ESP with a wire-cylinder geometry so that the collection efficiency of such a device may be modeled for particle sizes in the range 0,1 - 1,0 μm. This will in turn determine whether such a device is theoretically feasible for use in a residential installation.

CHAPTER 2

METHODOLOGY

2.1 The ESP model

This section will cover the theoretical details and steps involved in building the ESP model. Firstly, the physical basis for the ESP model will be established, followed by a description of the steps involved in applying CFD software to run the simulation and test the model. Finally, the assumptions and limitations of the model will be presented.

The construction of an ESP model requires an understanding of the processes at work, as well as their interactions. A schematic diagram showing the main processes and their interactions is shown in Figure 2.1.

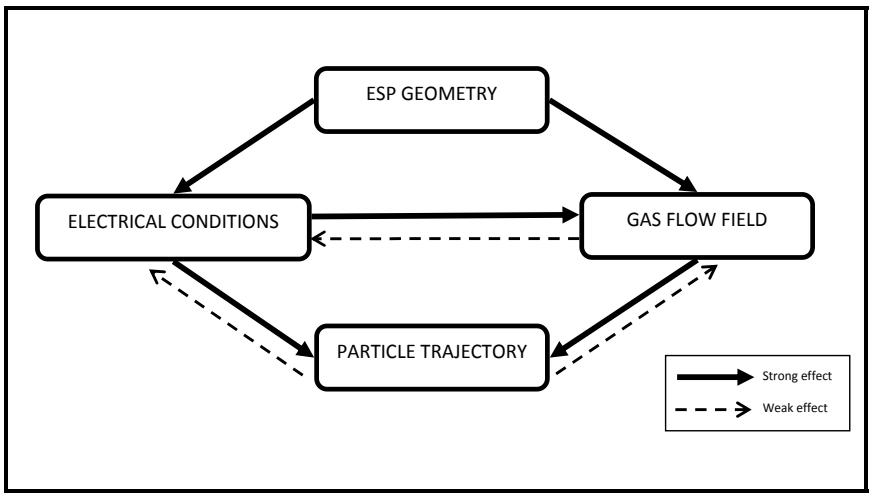

Figure 2.1 Schematic diagram of the main components and interactions in an ESP.
Adapted from Schmid and Vogel (2003, p. 119)

As can be seen from Figure 2.1, there are three separate systems that mutually interact, or are coupled, namely the gas flow field, the electrostatic field and charge distribution, and finally the particle flow. What we are ultimately interested in is the individual particle trajectories,

but we cannot solve for this system in isolation of the other two systems if we wish to create a realistic simulation. Each of these three systems must be solved simultaneously since they are coupled, and in this way the different interactions are able to influence the overall solution process in a realistic way. Once the system has converged, it can be said that each system has reached its equilibrium (or steady) state, and the testing of collection efficiencies can proceed. The most effective means of creating such a model without spending an inordinate amount of time on programming is to use commercial simulation software. Since the model must account for the effects of gas flow through the flue pipe and the turbulence generated thereby, only software capable of modeling complex fluid dynamics problems should be used. The software deemed most fit for this purpose is FLUENT, by Fluent Inc. (2006a). The *École de technologie supérieure* is in possession of a license for this software.

2.1.1 Gas flow field

As mentioned in section 1.3.1, CFD involves the numerical solution of the N-S equations for a given geometry (in 2 or 3 dimensions) and set of initial/boundary conditions. The basic steady state mass continuity equation in the notation of Fluent (2006a) is given as

$$\nabla \cdot (\rho \mathbf{U}) = S_m \tag{2.1}$$

Where ρ is the gas mass density (kg/m^3), **U** is the gas velocity vector (m/s) and S_m is the mass source term, usually equal to zero if there are no sources of mass in the volume under consideration.

If we assume the incompressible flow of a Newtonian fluid (as will be the case for this study), the steady state equation for the conservation of momentum as stated by Hughes and Brighton (1999) can be written as

$$\rho(\mathbf{U} \cdot \nabla \mathbf{U}) = -\nabla P + \mu \nabla^2 \mathbf{U} + \mathbf{B} \tag{2.2}$$

where P is the static pressure (Pa), μ is the dynamic viscosity of the fluid (kg/m/s), and **B** is the sum of body forces per unit volume (N/m^3), which, according to Choi and Fletcher (1997), for the case of an ESP can be written as

$$\mathbf{B} = \rho\mathbf{g} + \mathbf{F}_\mathrm{D} + \rho_{ion}\mathbf{E} \tag{2.3}$$

where **g** is the gravitational acceleration (m/s^2), $\mathbf{F}_\mathrm{D}$ is the aerodynamic drag force (N/m^3), ρ_{ion} is the ion charge density (C/m^3) and **E** is the electrostatic field (N/C). The form of the equation that is solved by FLUENT will depend on the geometry of the system. For example, an axisymmetric geometry requires the addition of an extra term of the form $(1/r)$ to the left hand side of equation 2.2.

The simplest interior (within solid boundaries) flow regime is laminar (plug) flow, where the velocity profile perpendicular to the main flow direction is constant. This simple, if unrealistic, type of flow was used before more sophisticated models were devised, and is useful in certain situations where no turbulence is expected. In most real-world situations however, the use of a turbulence model is required. The turbulence model employed for this study is the realizable k-epsilon *(k-ε)* model as described by Shih *et al.* (1995), which was designed to address the deficiencies in the standard k-ε model, and is fully integrated in the FLUENT software. The type of turbulence model chosen will also modify the form of the two equations au-dessus.

2.1.2 Electrostatics in a 2-D axisymmetric geometry

A commonly used ESP geometry is the wire-cylinder geometry shown in Figure 2.2, which has several practical and computational advantages, such as:

A. Cylindrical symmetry allows the use of a 2-D axisymmetric computational plane for modeling as shown by the shaded rectangular section in the figure;
B. The central wire facilitates the formation of a thin central corona discharge region;

C. Most residential wood stove flue pipes are cylindrical in shape.

Therefore, the simple wire-cylinder geometry presented here will be used as the reference case for the ESP model to be developed in the following chapters.

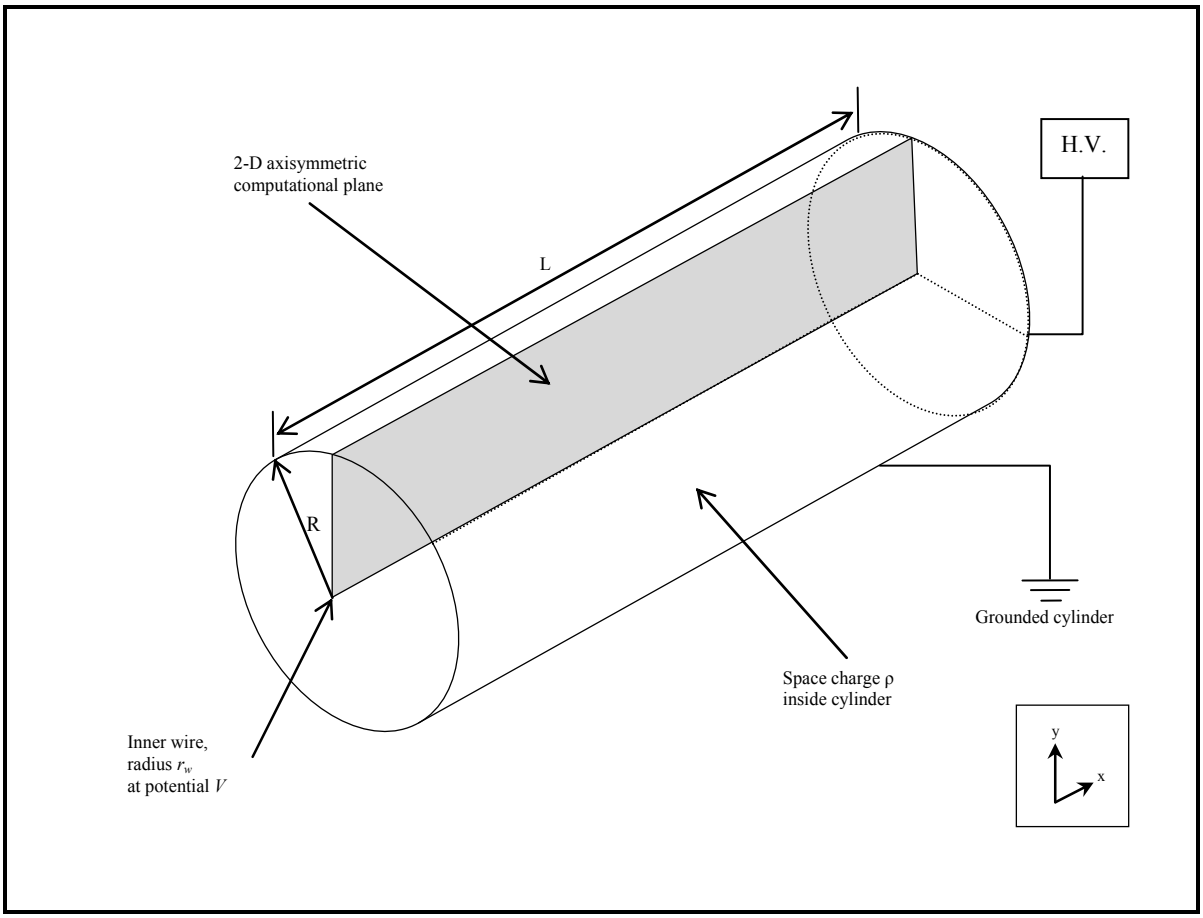

Figure 2.2 Schematic of the wire-cylinder geometry.

As described in section 1.2.4, corona discharge is initiated when the voltage applied to the inner wire exceeds a critical value. The empirical formula developed by Peek (1929) for a smooth, circular wire can be described as

$$E_c = 3 \text{ x } 10^6 \left[1 + 0{,}03\sqrt{\delta / r_w}\right] \qquad (2.4)$$

where E_c is the critical value of the electric field at the wire surface (V/m), r_w is the wire radius (m) and δ is defined as

$$\delta = {}^{T_0 P}/_{T p_0} \tag{2.5}$$

where T_o is the standard temperature (293 K) and p_0 is the standard pressure (101 325 Pa), T and P are the simulation temperature and pressure respectively. Since the current is zero at the critical voltage, the space charge in the cylinder is zero, and the equation for the electric field as a function of radius from the inner wire surface to the outer cylinder can easily be derived as shown by Hinds (1999)

$$E(r) = \frac{V}{r\, ln\left({}^{R}/_{r_w}\right)} \tag{2.6}$$

where V is the applied voltage at the wire (V), r is the radial distance from the wire surface (m), and R is the radius of the outer cylinder (m). This relation is only valid while there is no space charge present, i.e. the ion current is zero. The value of the critical wire voltage, known as the corona inception voltage (V_c) is then given by

$$V_c = E_c r_w\, ln\left({}^{R}/_{r_w}\right) \tag{2.7}$$

Hence the thinner the inner wire, the greater E_c becomes, but a smaller value of V_c is required to initiate corona discharge. Once the wire voltage increases beyond the critical voltage, the corona discharge becomes established and an ion current begins to flow from the wire to the grounded collection cylinder. The presence of this ion space charge in turn affects the electrostatic field and an equilibrium condition is reached where there is (for negative wire voltage) an electrically neutral corona region near the wire, free electrons and negative ions in the space between the corona discharge region and the outer cylinder. A simple schematic of a cylindrical ESP is shown in Figure 2.3.

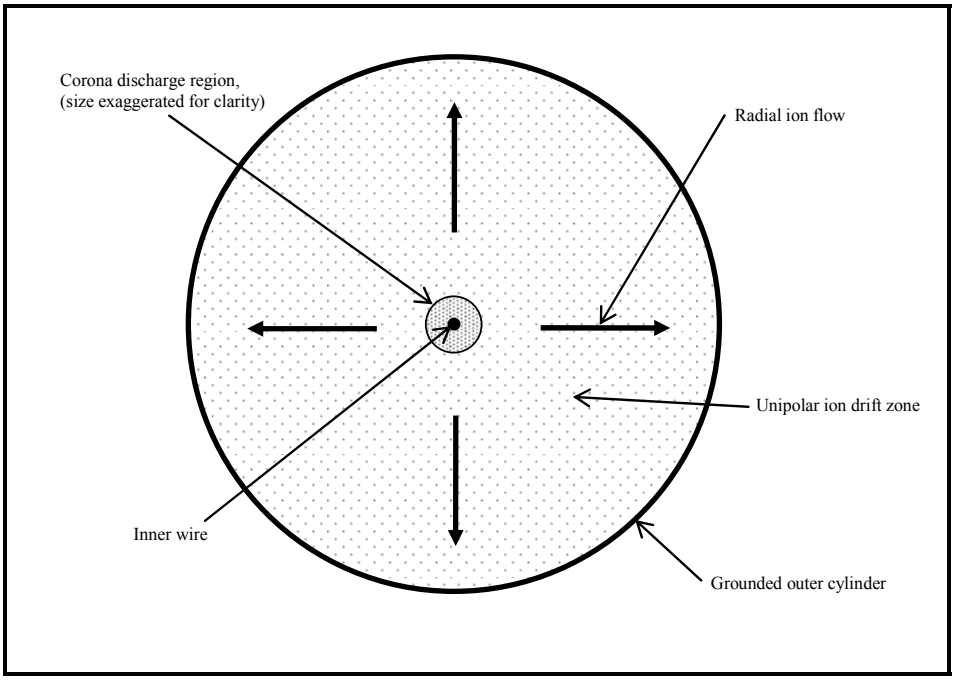

Figure 2.3 Plan view of a cylindrical ESP.

When there is significant space charge in the cylinder, the simple relation of equation 2.6 no longer holds, and it is necessary to use Poisson's equation to describe the electrostatic system, as explained by Duffin (1990)

$$\nabla^2 V = -\frac{\rho_{tot}}{\varepsilon_0} \tag{2.8}$$

where ρ_{tot} is the total space charge density (C/m^3) and ε_o is the permittivity of free space (F/m). The total space charge present within a closed volume is the sum of the contributions from both sources

$$\rho_{tot} = \rho_{ion} + \rho_{pc} \tag{2.9}$$

where ρ_{pc} is the particle charge density (C/m^3). The electric field vector (E-field) can be calculated using the following relation

$$\mathbf{E} = -\nabla V \tag{2.10}$$

The direction of the vector E-field is opposite to the potential gradient, i.e. from positive to negative potential. Next, it is necessary to have an expression for the current density in the ESP. According to Skodras *et al.* (2006), this can be defined as

$$\mathbf{j} = \rho_{ion} b_{ion} \mathbf{E} + \rho_{ion} \mathbf{U} + \rho_{pc} \mathbf{V}^{cell} \tag{2.11}$$

where $\mathbf{j}$ is the total current density (A/m^2), $\mathbf{V}^{cell}$ is the Eulerian particulate velocity vector (m/s) and b_{ion} is the electrical mobility of the ions (m^2/V/s), defined as the velocity of a particle with charge q in an E-field of unit strength. The first term on the right of this equation is the ion current density contribution, which depends on b_{ion} and the E-field. The ion electrical mobility is of great importance when simulating ESP performance, since it determines the magnitude of the ion current, which influences the charging rate of the particles, as will be seen later. The value of b_{ion} is usually assumed to be constant and depends on the polarity of the ions, and is greater for negative ions than positive ions. The second term is the convective transport term due to the gas flow. The third term is due to the particulate space charge, which transports charge at a velocity of $\mathbf{V}^{\text{cell}}$, as will be explained in section 2.1.3. In an ESP with an intense E-field present, the first term is dominant, and the third term only becomes important at high particle charge densities. Nonetheless, for completeness all the terms are included in the model.

We can then determine the total current flow from the following relation for charged particles in motion

$$I = \int_S \mathbf{j} \cdot d\mathbf{S} \tag{2.12}$$

where I is the total current (A) across an area S (m^2), and d$\mathbf{S}$ is the vector area normal to its plane. Following equation 2.8, the second fundamental equation needed to describe ESP operation is the steady-state current continuity equation, which is based on the fundamental principle of conservation of charge

$$\nabla \cdot (\mathbf{j} - D_e \nabla \rho_{ion}) = 0 \tag{2.13}$$

where D_e is the effective ion diffusivity (m^2/s). The second term in brackets is a diffusive term. We can see that equations 2.8 and 2.13 are strongly interdependent (coupled) by way of equation 2.11.

In the above we have presented the equations in vector form. It is then necessary to carry out a transformation to the desired coordinate system so they can be applied to specific geometry. What we are really interested in is the force exerted on charged particles in an ES field generated within a given geometrical configuration. It is possible to solve equations 2.8 & 2.13 analytically in the 1-D case for a cylindrical geometry, and this allows a relation between the current per unit length and the wire voltage in the ESP to be developed, as described by Oglesby and Nichols (1970)

$$V = V_c + r_w E_c \left[\sqrt{1 + \frac{i}{2\pi\epsilon_0 b_{eq}} \cdot \left(\frac{R}{r_w E_c}\right)^2} - 1 - ln\left(\frac{1+\sqrt{1+\frac{i}{2\pi\epsilon_0 b_{eq}}\cdot\left(\frac{R}{r_w E_c}\right)^2}}{2} \right) \right] \quad (2.14)$$

where i is the current per unit length of the ESP (A/m) and b_{eq} is the equivalent mobility taking into account the much lower mobility (by a factor of 100 or more) of the particles, as determined by Oglesby and Nichols (1970)

$$b_{eq} = \left(\rho_{ion}/\rho\right) b_{ion} \quad (2.15)$$

where b_{eq} is the equivalent mobility ($m^2/V/s$). The space charge ratio (ρ/ρ_{ion}) is equal to unity when no particle charge is present, but can reach high values when high concentrations of charged particles are present in the ESP. It can be seen that for $i = 0$, $V = V_c$ as expected. Here they have assumed that the radius of the corona glow region is equal to the wire radius, which is an approximation. A similar expression derived by Waters and Stark (1975) uses a different boundary condition based on the approximate radius of the glow region. These equations allow us to plot approximate voltage-current (V-I) curves for a particular

cylindrical ESP configuration, and under given particle loading conditions (a given value of b_{eq}). This will be useful during the simulation procedure, described in the next section.

In this section we have presented the vector equations required to describe the electrostatic processes behind the operation of an ESP. The main variables that need to be solved for in the model are the potential field (V), the E-field (**E**), and the ion charge density (ρ_{ion}). Due to their interdependent nature, these variables need to be solved simultaneously during the simulation, in addition to the effects of the gas flow field and the particle flow.

2.1.3 Particle charging

As was mentioned in Chapter 1, particle charging mechanisms are an ongoing field of research, and many models exist, each with its own limitations and applicability. It was determined that any simulation that involves particles in the submicron domain must include both field and diffusion charging mechanisms. In this size range, these two mechanisms are approximately equal in magnitude, with the field charging mechanism becoming dominant at greater particle diameters. In the review carried out by Lawless (1996), the sum-of-charges model is seen to fit experimental results as well as any of the other more sophisticated models they compared. This model was therefore selected as the charging model for the current simulation.

First of all, it is important to understand the quantum nature of electrical charge, the smallest unit of which is the electronic charge e, with a value of 1,6 x 10^{-19} C. Hence, any amount of particle charge can be quantified using the following equation

$$q_p = n_c e \tag{2.16}$$

where q_p is the total charge on the particle and n_c is the integer number of elementary charges. Electrons by definition have a negative charge. An ion is a molecule or atom that has either an excess or a deficiency of electrons, relative to the positively charged protons.

The same principle can be applied to any particle. For example, a particle with an excess of negative ions attached to it is negatively charged.

The model presented by Lawless (1996) consists of charging rate equations in dimensionless form. Hence there are no simple analytical forms of these equations and they must be integrated numerically in order to calculate the particle charge q_p at time t. The classical continuum diffusion charging rate is given by

$$dp/d\tau = Be(p) \equiv p/(e^p - 1) \tag{2.17}$$

where *Be(p)* is the dimensionless diffusion charging rate, also known as the Bernoulli function, p is the dimensionless charge, given by

$$p = \frac{q_p e}{4\pi\varepsilon_0 r_p k T_p} \tag{2.18}$$

and τ is dimensionless time, given by

$$\tau = \frac{\rho_{ion} b_{ion} t}{\varepsilon_0} \tag{2.19}$$

where r_p is the particle radius (m), k is Boltzmann's constant (J/K), T_p is the particle temperature (K) and t is the time in seconds.

The classical field charging rate equation as described by Lawless (1996) in dimensionless notation is

$$dp/d\tau = \mathrm{F}(p, w) \equiv aw/4\left(1 - \frac{p}{aw}\right)^2, \quad -aw \le p \le aw$$

$$\mathrm{F}(\mathrm{p}, \mathrm{w}) \equiv 0\,, \quad p > aw \tag{2.20}$$

where *F(p,w)* is the dimensionless field charging rate, *w* is the dimensionless electric field magnitude given by

$$w = {r_p eE}/{kT} \tag{2.21}$$

and *a* is a term which accounts for the dielectric properties of the particle material as follows

$$a = \frac{3\varepsilon_r}{(\varepsilon_r+2)} \tag{2.22}$$

where ε_r is the dielectric constant (or relative permittivity) of the particle material. For highly conductive materials such as metals, ε_r is essentially infinite and *a* tends to a value of 3. The quantity *aw* is the field saturation charge, the value of charge beyond which no further charge is added to the particle via the field charging mechanism, essentially due to the repulsion of like charges.

Thus, the sum-of-charges charging model can be stated as follows

$$\begin{aligned} {dp}/{d\tau} &= F(p,w) + Be(p)\,, & 0 \le p \le aw \\ {dp}/{d\tau} &= Be(p)\,, & p > aw \end{aligned} \tag{2.23}$$

The above descriptions of the sum-of-charges model must be applied to the ESP simulation in such a way that the charge on each particle can be numerically integrated over time along its trajectory through the ESP, as so-called Lagrangian variables (variables associated with individual moving particles), and then consequently summed for each computational cell to obtain so-called Eulerian variables (variables associated with each fixed cell) attributed to each cell in the domain. These operations are not standard functions of the FLUENT program, but required the addition of so-called User Defined Functions (UDF) that are written by users of the program to accomplish non-standard tasks such as the above-mentioned integrations. These will be discussed in section 2.1.6 au-dessous. In order to

calculate the Eulerian variable for the particle space charge ρ_{pc} (C/m^3), the following summation is used, as presented by Skodras *et al.* (2006)

$$\rho_{pc} = \frac{\sum_{n=1}^{N}\left(\frac{\dot{m}_p^n}{m_p^n}\right) q_p \Delta t^n}{V_c} \tag{2.24}$$

where n is the particle injection index, from 1 to N, m_p is the particle mass (kg), $\dot{m}_p$ is the particle mass flow rate (kg/s), Δt is the particle residence time in the cell ($t_{out} - t_{in}$), and V_c is the cell volume (m^3). The particle mass concentration ρ_p (kg/m^3) can be calculated in a similar fashion to equation 2.24, and this allows the Eulerian particulate velocity $\mathbf{V}^{cell}$ to be calculated using the following equation

$$\mathbf{V}^{cell} = \frac{\sum_{n=1}^{N} \dot{m}_p^n \int_{t_{in}}^{t_{out}} \mathbf{v}^n dt}{\rho_p V_c} \tag{2.25}$$

where $\mathbf{v}^n$ is the nth particle velocity, and the integral is the distance travelled in the cell for each particle. The Eulerian particulate velocity is usually close to the gas flow velocity, except in the region near the inner wire where there is a significant body force acting on the particles due to the intense E-field.

2.1.4 Particle trajectories

The particle trajectories can be calculated by integrating the classic force balance differential equation as stated below

$$m_p \dot{\mathbf{v}}_p = \mathbf{F}_D + \mathbf{F}_g + \mathbf{F}_{ES} \tag{2.26}$$

where $\dot{\mathbf{v}}_p$ is the particle acceleration (m/s^2), $\mathbf{F}_g$ is the gravitational force, and $\mathbf{F}_{ES}$ is the electrostatic force acting on the particle. In ESP applications, the gravitational force is insignificant compared to the drag and ES forces, and can be neglected without affecting the results.

The aerodynamic drag force $\mathbf{F}_D$ is dependent on the particle Reynolds number, as described by Hinds (1999). For particle Reynolds numbers much smaller than unity, which is usually the case for submicron particles, the particle is said to be in the Stokes drag regime. A modified Stokes drag force per unit particle mass can be calculated using the following formula from Ounis, Ahmadi and McLaughlin (1991)

$$\mathbf{F}_D = \frac{3\pi\mu d_p}{C_c}(\mathbf{U} - \mathbf{v}) \tag{2.27}$$

where **v** is the particle velocity vector (m/s) and C_c is the Cunningham slip correction factor, which accounts for the discrete molecular nature of gas at submicron scales and smaller. The factor is calculated using the following formula described in Fluent Inc. (2006a)

$$C_c = 1 + {}^{2\lambda}/_{d_p}\left[1{,}257 + 0{,}4e^{\left(\frac{-0{,}55d_p}{\lambda}\right)}\right] \tag{2.28}$$

where λ is the molecular mean free path (MFP) of the carrier gas (m). The Cunningham slip correction becomes appreciable for particle diameters smaller than 1 μm (C_c = 1,17) , and halves the drag force at a particle diameter of 0,18 μm. The drag force is calculated automatically by FLUENT, with the appropriate value of C_c entered as a parameter.

We can calculate the ES force exerted on any charge q_p using the relation

$$\mathbf{F}_{\mathrm{ES}} = q_p\mathbf{E} \tag{2.29}$$

We can see that in order to calculate the ES force on a particle, we need to know the net charge on the particle (and its polarity), and also have a knowledge of the E-field at every point within the ESP. The ES force is calculated by way of a UDF, as described in section 2.1.6.

The complete force balance equation 2.26 is solved for the Lagrangian variables of particle velocity and position along the trajectory by implementing the Discrete Phase Model (DPM) in FLUENT, which is based on the Euler-Lagrange approach. This approach uses Lagrangian variables for the discrete phase, which can exchange mass, momentum and energy with the fluid. For more details, please refer to the FLUENT User Guide.

2.1.5 Computational grid generation

Before any simulations can begin, it is necessary to generate a computational grid within the limits of the domain to be modeled. As was explained in section 2.1.2, a cylinder can be modeled using a 2-D axisymmetric plane as the domain, and a schematic representation of this plane is shown in Figure 2.4.

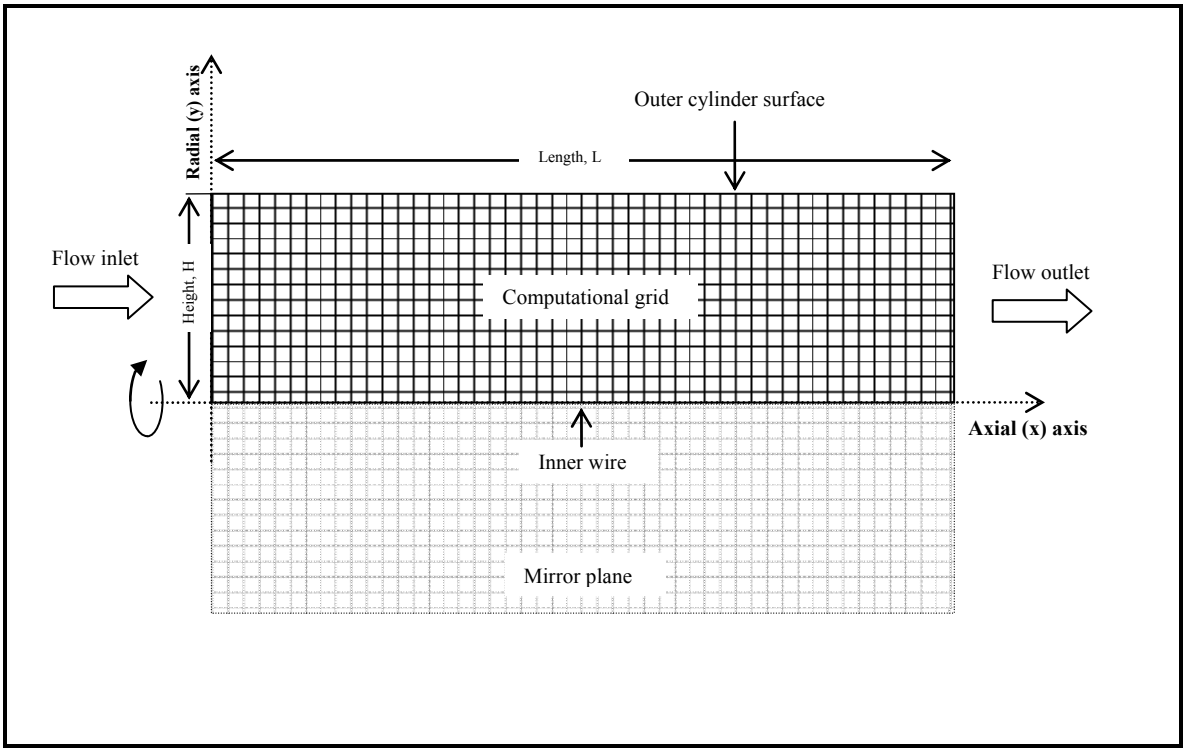

Figure 2.4 Schematic view of the 2-D axisymmetric computational domain.

The domain has four boundaries, namely the flow inlet, flow outlet, outer cylinder, and the inner wire surface. The computational grid is composed of a large number of quadrilateral cells, whose area varies depending on where they are in the domain. The grid is more refined near boundaries where higher gradients and boundary layers are expected. In the case of the ESP, it is the outer cylinder wall boundary and the inner wire surface boundary that have a more refined grid nearby, as can be seen in Figure 2.5. The cell size is chosen according to the size of the domain and the computer processing power available, and should be refined enough to accurately capture the behaviour of the gas and particle flow. For example, in the case of the reference model (see section 2.3.1) a normal cell size of 2mm x 2mm with refined cells at two boundaries leads to a total of 18 375 cells in the domain. The mirror plane is simply a reflection of the computational plane along the x-axis to aid visualization of the results.

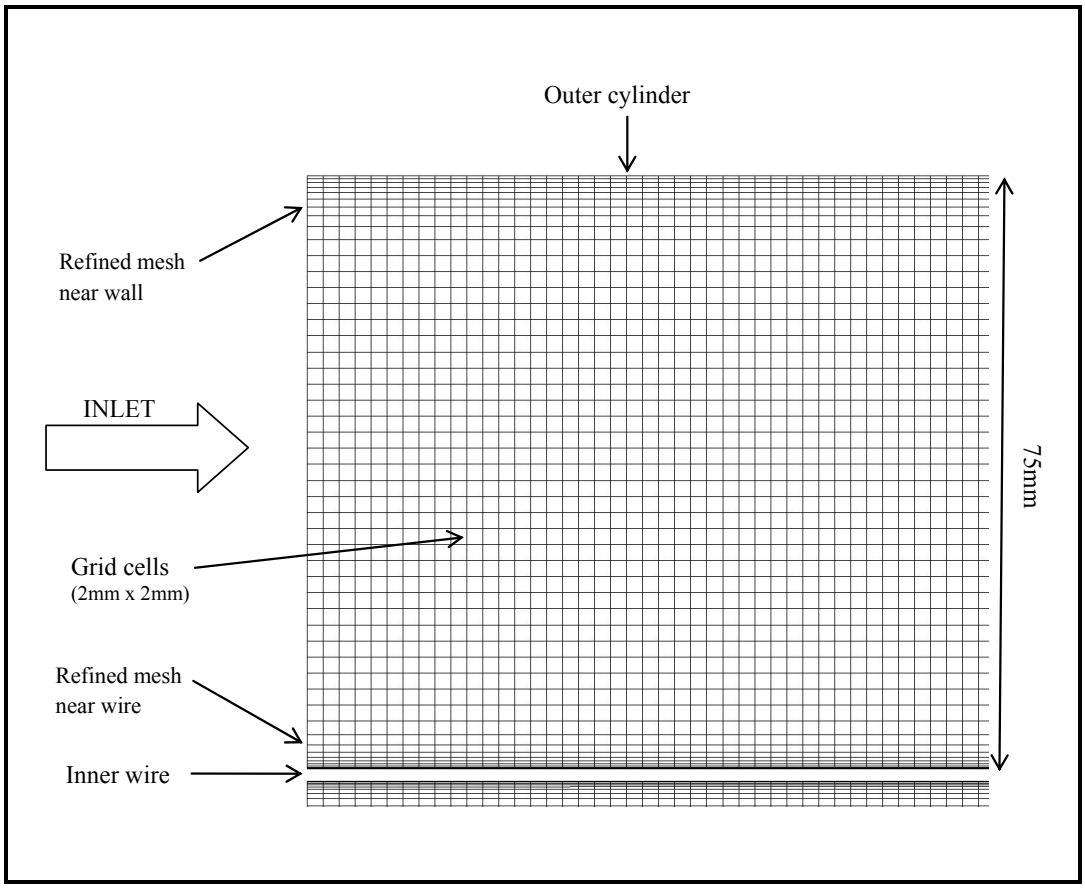

Figure 2.5 The computational grid of the reference model near the inlet.

The abovementioned plane is applicable to symmetrical geometries such as cylinders and provides nearly all the information that a full 3-D model would provide, but with much faster computations due to the reduced number of cells required (an order of magnitude less for 2-D compared to 3-D). A specialized software package named GAMBIT (2006b) was used in order to generate the grid according to the required specifications. Once the grid is generated, it can be imported into FLUENT to be used for simulation. For more details on the grid generation, please refer to the GAMBIT User Guide.

2.1.6 Model creation using UDF macros

In order to build the complete ESP model, a number of UDF macros (or UDFs) were written for various purposes and will be described in this section. All of the UDF macros were written in the C programming language, and were linked and compiled using Microsoft Visual C++ Express 2008. A complete listing of the source code can be found in Appendix I. Once compiled, the UDF macros become part of the FLUENT program, and the various components can be activated/de-activated using the FLUENT graphical user interface (GUI).

The electrostatic components of the ESP are not standard functions in FLUENT and had to be added using UDF macros. Firstly, several UDF macros were written in order to set variable names and to initialize the variables. The components of the E-field were calculated after each iteration using equation 2.9 programmed into a UDF macro. In order to get the program to solve the potential field V and the ion charge density ρ_{ion} variables, two new scalar variables were introduced as User Defined Scalars (UDS) in the program. The standard FLUENT UDS transport equation is given by Fluent Inc. (2006a) as

$$\nabla \cdot (\rho \mathbf{U} \varphi - D_e \nabla \varphi) = S_\varphi \tag{2.30}$$

where φ is the scalar variable to be solved. In the case of the potential, the convective term in the above equation is equal to zero, and D_e is set to unity. The source term on the right hand side (S_φ) is set to ρ_{tot}/ε_0. This allows the Poisson equation (2.8) to be solved by the program.

For the ion charge density ρ_{ion}, we expand equation 2.13 and substitute it into equation 2.30. After re-arranging, we get the following transport equation

$$\nabla \cdot \left(\rho \rho_{ion} \mathbf{U} - D_{\rho_{ion}} \nabla \rho_{ion}\right) = S_{\rho_{ion}} \tag{2.31}$$

where $D_{\rho_{ion}}$ is the ion diffusion coefficient (ρD_e), and $S_{\rho_{ion}}$ is the source term, given by

$$S_{\rho_{ion}} = -\rho \nabla \cdot \left(\rho_{ion} b_{ion} \mathbf{E} + \rho_{pc} \mathbf{V}^{cell}\right) \tag{2.32}$$

where the first term in brackets is the ion current density, $\mathbf{j}_{\text{ion}}$ (A/m^2) and the second term is the particle current density, $\mathbf{j}_{\text{p}}$ (A/m^2).

Table 2.1 shows a list of all the UDFs that were written for this project, including a short description of their purpose.

Table 2.1 List of FLUENT UDF macros written to build the ESP model

UDF name	Purpose
DEFINE_EXECUTE_ON_LOADING(on_loading)	Set user defined scalar and memory names
DEFINE_INIT(particle_setup)	Initialize particle user memory and names
DEFINE_DPM_INJECTION_INIT(Init_V_T)	Set initial particle velocity and temperature equal to gas values
DEFINE_ADJUST(Calc_E_xy)	Calculate E-field using equation 2.9
DEFINE_SOURCE(phi_source)	Calculate source term for the potential, V (eqn. 2.8)
DEFINE_SOURCE(rho_source)	Calculate source term for ion charge density, ρ_{ion} (eqn. 2.32)
DEFINE_SOURCE(x_mom_source)	Calculate source term for axial momentum, $\rho_{ion}\mathbf{E}_x$ (eqn. 2.4)
DEFINE_SOURCE(y_mom_source)	Calculate source term for radial momentum, $\rho_{ion}\mathbf{E}_y$ (eqn. 2.4)
DEFINE_DPM_SCALAR_UPDATE (particle_charge)	Calculate particle charge along trajectory (Lagrangian variable)
DEFINE_DPM_SOURCE(q_source)	Sum particle variables (charge, mass, number) in each cell
DEFINE_ADJUST(rho_particle)	Calculate Eulerian variables (ρ_p, ρ_{pc}, V^{cell}) from Lagrangians
DEFINE_DPM_BODY_FORCE(body_force)	Calculate body force on particles using equation 2.29

Two UDFs were written to calculate the gas momentum source terms, one for the axial component and one for the radial component of the electrostatic momentum force ($\rho_{ion}\mathbf{E}$), as described by equation 2.3. Lastly, several UDFs were written to deal with the particle phase, including one to calculate the charge accumulated by each particle using the model described

in section 2.1.3, two UDFs were needed to calculate particle charge, number and mass densities, and one UDF to calculate the body force on the particles using equation 2.29.

2.2 Simulation procedure

Once the ESP model has been built and tested, the complete simulation can be carried out by bringing together all the components of the model, namely the gas flow variables, the electrostatic components, and the DPM components. As was explained in section 2.1, all the model components are coupled hence it is necessary to run the simulation with all the variables being solved simultaneously. The basic procedure is to initialize the variables, set the number of iterations required for the flow variables, and set the number of flow variable iterations per DPM injection, then launch the solver. After each iteration the convergence of each variable being solved is displayed numerically and graphically, and the iteration procedure is automatically stopped once all the convergence criteria are met. This will be described in more detail below.

2.2.1 Initial values and boundary conditions

The solver requires that initial values for all the variables being solved be set prior to launching the iteration process. The values can be set manually, or the solver can use values from the various boundaries as initial values. The boundary condition must be known for all the variables at boundaries in order for the solver to be able to reach a solution. These conditions are set for each boundary and each variable in FLUENT prior to launching the solution process. The boundary conditions used for this project are shown in Table 2.2.

Due to the no-slip boundary condition at the cylinder wall, the constant axial velocity at the inlet does not hold further into the domain. The radial velocity profile changes shape with distance along the axial direction, and eventually a stable profile will be reached. This is referred to as a fully developed duct flow profile. Over short distances however, the flow does not have time to reach this state, and is referred to as partially developed flow, which is the case we are dealing with.

Table 2.2 ESP model boundary conditions used during the simulation

Boundary	Gas velocity	Particle behaviour	Electric potential	Ion charge density
Inlet	U_x=constant or profile [a] U_y=0	v_x=gas velocity[e] v_y=0	Neumann[f]	Neumann
Outlet	Variable[b]	Escape	Neumann	Neumann
Wire surface	No-shear[c]	Reflect	Constant[g]	Manual adj.[h]
Cylinder surface	No-slip[d]	Trap	0	Neumann

a – either a constant axial gas velocity or a velocity profile, but different simulations can have different velocity magnitudes.
b – the outlet gas velocity profile depends on the conditions of the simulation, but mass is conserved.
c – the no-shear condition means the wire does not affect the gas flow, due to its small size.
d – the no-slip boundary condition means that the gas velocity at the cylinder surface is zero.
e – the particle velocity at the inlet is set equal to the gas velocity.
f – Neumann boundary condition states the dot product of the flux and the normal vector into the domain is 0.
g – a constant applied voltage on the inner wire surface, but different simulations can have different voltages.
h – the ion charge density at the wire surface was varied manually to reach the desired current flow.

Initial values for the electrostatic variables are all set to zero. During the first few iterations the values will rapidly reach their proper levels, based on the set boundary conditions.

2.2.2 DPM injection setup

For simulation purposes, it is convenient to use a series of monodisperse particle distributions (with only a single uniform particle diameter) to represent a realistic poly-disperse distribution of particles. The particle diameters can easily be varied and this allows a complete particle diameter vs. particle collection efficiency curve to be produced from the model. Since experimental particle distributions can often be classified simply by their CMD and σ_g, it is straightforward to re-create number distributions for a given set of particle sizes that can then be set up in the simulation software.

It is necessary to define the injection parameters for each of the DPM injections created in FLUENT at the inlet to the computational domain. Each injection is set to be mono-disperse since for sub-micron sized particles the Cunningham slip correction factor must be applied (see section 2.1.4) for each particle size (injection) individually. Experimental results usually provide a value for the CMD or MMD of the particle distribution, along with a value for σ_g. Based on this knowledge, it is possible to create a fractional number distribution for any

given series of particle diameters using the properties of the log-normal distribution described in section 1.2.2.

Once the fractional number distribution is found, it can be used to calculate the mass flow rate of particles in each size range. The volume flow rate in the ESP can be estimated by

$$\dot{V}_{flow} = \overline{U}_x A_{xs} \tag{2.33}$$

where $\dot{V}_{flow}$ is the volume flow rate in the ESP (m^3/s), $\overline{U}_x$ is the mean axial gas flow speed (m/s) and A_{xs} is the cross-sectional area of the ESP (m^2). Next, the mass concentration (kg/m^3) of the particles in each size range can be calculated from

$$\rho_p = n_p m_p \tag{2.34}$$

where n_p is the fractional number density for the given particle diameter (m^{-3}). The mass flow rate (kg/s) of the particles in each size range can then be calculated using the following relation

$$\dot{m}_p = \rho_p \dot{V}_{flow} \tag{2.35}$$

The sum of all the fractional number densities used should equal the total global number density, N_p (m^{-3}). The value of N_p is known from experimental results, and is in the range 10^{10} to 10^{14} as measured by Hueglin (1997) and Hedberg (2002). In a similar fashion, the overall particle mass concentration can be calculated by summing the values of ρ_p for each size range. A DPM injection was created for each particle size to be simulated and the mass flow rates at the inlet calculated from the above equations were set in the program.

2.2.3 Solution process

Once the boundary conditions and the initial values have been set, the solution process can be initiated by launching the required number of iterations. The FLUENT solver monitors the

convergence progress of each of the variables that are currently being solved. A list of these variables is provided in Table 2.3. A nominal convergence criterion of 0,1% was used for the flow variables, and 0,001% for the electrostatic variables. A flow diagram of the solution process is shown in Figure 2.6.

The DPM injection of particles into the domain can be set to occur at a chosen interval of flow field iterations. During the iteration process, all of the injections are applied, thus simulating the real-world situation of a log-normal distribution of particles at the inlet. It was assumed that the particles are evenly distributed across the inlet, and the mass flow rate of each injection was scaled according to the area of the face in which the injection resides. If the particles are injected at short intervals, the flow field may not have time to reach a stable convergence.

Table 2.3 List of variables solved during the iteration process

N°	**Variable**
1	Mass continuity (kg)
2	Axial (x) gas velocity, U_x (m/s)
3	Radial (y) gas velocity, U_y (m/s)
4	Energy (J)
5	Turbulent kinetic energy (m^2/s^2)
6	Turbulent dissipation rate (m^2/s^3)
7	Electric potential, V (V)
8	Ion charge density, ρ_{ion} (C/m^3)

An interval of 100 flow field iterations per DPM iteration produces convergence but is slower due to the increased number of iterations performed. The effect of the DPM injections on the convergence depends on the mass flow rate of the injections, the higher the mass flow rate, the greater the effect on convergence of all the variables.

Another parameter that must be monitored is the total current flow in the ESP, as determined by equation 2.12. The FLUENT program was configured to calculate the total current flow I, and display the value after each iteration. The reason that this parameter is important is that

manual adjustment of the ion charge density value at the wire surface was required to obtain the target current flow as determined from equation 2.14.

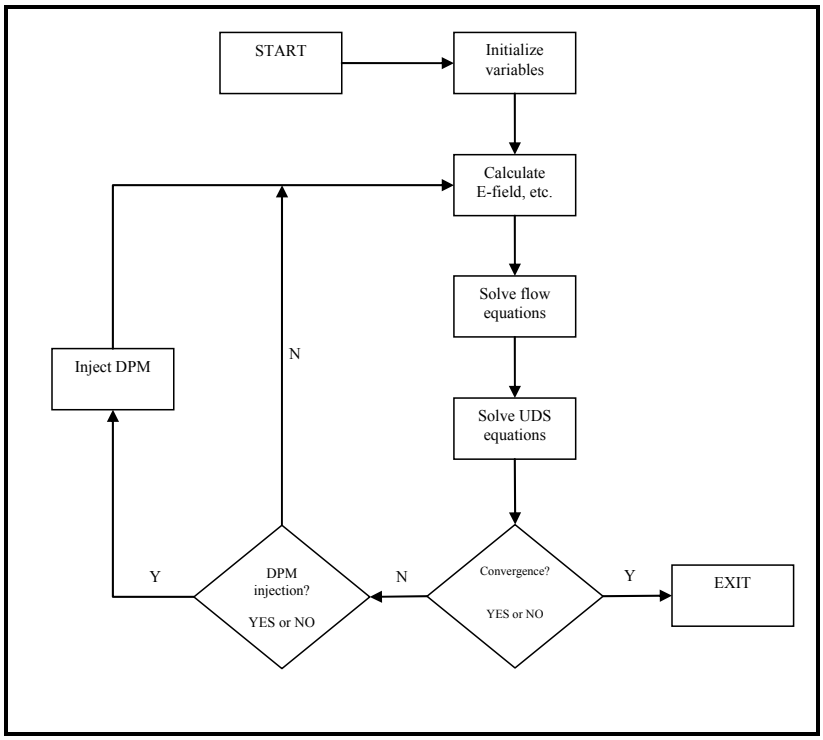

Figure 2.6 Flow chart of the FLUENT solution process for the ESP simulation.

In order to reach a converged solution, a minimum of 500 iterations was usually required and sometimes as many as 2 000. Once an acceptable convergence was obtained, the data file was saved so that the various flow and field variables could be restored at a future date if necessary. Each of the variables could be displayed on screen as contours or profiles for verification. The ESP can be said to be in a steady-state resulting from the initial and boundary conditions applied at the beginning, and the various variables accurately represent the conditions inside the ESP. It is under these conditions that the ESP collection efficiency must be tested, as will be described in the following section.

2.2.4 ESP collection efficiency evaluation

The ESP particle collection efficiency can be tested for a given particle diameter by injecting a given number of such particles and tracking their progress through the ESP. Particles that pass through the outlet are said to have escaped the domain, while particles which touch the outer collection cylinder are said to have been captured. Thus, the collection efficiency for a given particle diameter can be readily calculated by

$$\eta = {}^{n_{cap}}/_{N_{tot}} \tag{2.36}$$

where η is the collection efficiency, n_{cap} is the number of particles captured for each tracking sample, and N_{tot} is the total number of particles injected into the domain. Note that due to symmetry, the value of η calculated for the 2-D axisymmetric geometry is equal to the 3-D or real-world value. Note also that this is a number-based collection efficiency, as opposed to a mass-based efficiency that is often quoted in the literature. The mass-based efficiency is the mass of particles captured divided by the total mass of particles flowing through the ESP. However, for typical sub-micron particle distributions, mass-based efficiency values are of the same order of magnitude as number-based efficiencies.

In order to simulate the turbulent dispersion of the particles, a stochastic tracking model was activated during the collection efficiency tests. This model works by integrating the instantaneous value of the fluctuating gas flow velocity (which includes turbulence effects) to predict particle trajectories. This process in repeated for a user-defined number of tries (n_t), and each try will include the random effects of turbulence on the trajectory. For example, if we have 30 inlet faces with 1 injection each, and we set the value of n_t to be 20, then the total number of particles tracked during a DPM tracking sample (N_{tot}) is the product of these three quantities, i.e. 600 stochastic particles. If this procedure is repeated 5 times, we have a total of 3 000 stochastic particles. We can obtain an idea of the variation that the stochastic model introduces by calculating the standard deviation of five sample repeats.

The above testing was carried out automatically by launching a "Journal" file for the procedure, which is basically a script file that provides commands to FLUENT in the proper sequence. The sequence followed by the Journal file is the following:

A. Set the appropriate value for the Cunningham slip correction;
B. Select the particle diameter (injection) to be tested;
C. Track the particles using the stochastic model for the required number of repeats.

The results of the particle tracking are displayed on the console screen, and consist of the number of particles captured, escaped, incomplete and the total. This information was saved to a raw data file in text format. The raw data was subsequently analyzed and read into a Microsoft Excel file via a macro (see Appendix II). The ESP collection efficiency data was then graphed as a function of particle diameter for comparison and presentation.

Each of the collection efficiency curves described above is valid only for a given set of parameters used for that simulation. It is useful, however, to re-run the simulation over a range of values of a given parameter (applied voltage, for example). It is then possible to calculate an overall weighted-average collection efficiency (η_{ov}) based on the particle number flow rate (NFR) for all the particle diameters tested, using the following expression

$$\eta_{ov} = \sum \eta_{d_p} \left(\frac{\dot{n}_{d_p}}{\sum \dot{n}_{d_p}}\right) \tag{2.37}$$

where η_{d_p} is the fractional collection efficiency and $\dot{n}_{d_p}$ is the particle NFR (s^{-1}) for particle size d_p. This value can then be plotted against the parameter being varied in order to visualize its effect on overall collection efficiency, as shown in the results section.

2.2.5 Model validation

Before the model can be applied to simulate the collection efficiency of an ESP for wood stove applications, it must be validated using experimental data from a similar system. The

system that most closely resembled the proposed ESP and provided most of the parameters and data required for validation was that produced by Zhuang *et al.* (2000). This experimental setup was briefly described in section 1.2.4.

Although their study was aimed at examining the behaviour of ultra-fine particles in a bench scale ESP, they did provide some data in the sub-micron size range (0,1 – 1,0 μm). They measured the collection efficiency of a single-stage ESP at certain applied voltages, using alumina particles of a given CMD. The physical and electrical properties of alumina are relatively well known. Experimental voltage-current curves for the ESP were available that could be used to test the validity of equation 2.14. Details of the gas flow field were sparse however, and only a uniform inlet gas flow velocity was specified. There were no details of the ion charge density distribution, and they assumed a uniform constant value across the ESP. However, these data were not essential for comparison with their experimental data.

The geometry of the Zhuang *et al.* bench scale ESP was replicated and a 2-D axisymmetric computational grid was created using the method described above. Then the appropriate initial and boundary conditions were selected for the flow variables, the electrostatic variables and the DPM model. Then the simulation was run until convergence was reached. The ESP collection efficiency for each particle diameter was then obtained using the method described in section 2.2.4. The resulting efficiency curve could then be compared with the experimental data.

2.2.6 Assumptions & limitations

The main assumptions that apply to the simulations are as follows:

A. Particle-particle collisions are neglected;
B. Particles are considered to be solid and spherical in shape;
C. The gravitational force is neglected;

D. Particle re-entrainment (particles that detach from the collection cylinder surface) is neglected;
E. The gas flow is incompressible (valid for low-velocity flows);
F. The carrier gas is dry air (no modification of constituents due to combustion).

The limitations of the simulations can be summarized as follows:

A. The particle charging model is not valid for particle sizes less than 0,1 μm;
B. The effects of coagulation and condensation of particles are neglected, but these may be of importance in the case of simulating wood burning flue gases;
C. The exact composition of the particles has been simplified to a single molecular constituent, whose physical and electrical properties may differ somewhat from the actual;
D. The stochastic tracking scheme is based on the quantity of turbulence in the domain, which is arbitrarily set at the inlet, but in reality turbulence is a random phenomenon.

2.3 Electrostatic precipitator simulation models

Once the simulation procedure has been validated against experimental data, it can be applied to any number of different geometries under operating conditions which are likely to be present in the flue pipe of a wood burning stove. In addition to the validation model, two additional models were built and simulated using the above procedure, as described in this section.

2.3.1 Reference model

The reference model is based on the simplest possible geometry for an ESP that fits directly into a standard steel flue pipe of diameter 0,15 m. The length of the ESP was selected based on a criterion of ratio of length to diameter of 20 (as for the validation model). A set of reference operating conditions was determined for this model, including flue gas temperature and velocity, particle composition and number distribution, and electrostatic parameters.

These parameters were based on experimental data, but for cases where no data were readily available, values were determined by theoretical calculation.

2.3.2 Prototype model

A prototype ESP model was devised and evaluated, based on the results of the validation and reference models. The objective was to obtain a prototype ESP model that is capable of operating at an overall efficiency of at least 75% at the lowest possible operating values for voltage and power. There are evidently many possible geometries that could meet the required specifications. However this study is limited to studying one such geometry in detail using the simulation procedures developed above. The details of the prototype model are presented in section 3.3.

The reasons for carrying out the optimised model simulation are firstly to demonstrate the usefulness of the simulation technique, and secondly to provide a comparison to the reference model.

CHAPTER 3

RESULTS

3.1 Validation model results

In this section we will present the results of the validation model, based on the data of Zhuang *et al.* (2000). Firstly, the model geometry and the various parameters will be presented, along with the measured and calculated V-I curves. This will be followed by graphical plots of the converged solution for the flow, particle and electrostatic variables. Finally the ESP efficiency vs. particle diameter curve obtained from the model will be presented and compared with the experimental data, along with curves showing the variation of the overall ESP efficiency with applied voltage and inlet gas flow velocity.

3.1.1 Model geometry and parameters

The model geometry, constant values, initial values and particle parameters are presented in Table 3.1.

Table 3.1 Validation ESP model parameters and constants

ESP MODEL GEOMETRY & GLOBAL CONSTANTS		FIXED BOUNDARY CONDITION VALUES		PARTICLE PARAMETERS	
Length, L (x-axis) (m)	0,15	U_x - inlet (m/s) U_y - inlet	0,35 0	Material	Alumina (Al_2O_3)
Height, H (y-axis) (m)	0,015	Turbulence Intensity – inlet (%)	10	Mass density (kg/m^3)	4 000
Wire radius (m)	$2{,}5\times10^{-4}$	Ion charge density – wire (C/m^3)	$1{,}6\times10^{-5}$	Dielectric constant, ε_r	9,34
Ion mobility, b_{ion} (m^2/V/s)	$1{,}9\times10^{-4}$	Applied voltage - wire (kV)	-9	CMD (μm)	0,25
Pressure (kPa)	101	Potential – cylinder (kV)	0	σ_g	1,7
Temperature (K)	296	Corona inception voltage (kV)	-8,8	Particle number density – inlet (m^{-3})	5×10^{13}
Gas density (kg/m^3)	1,23			Particle mass concentration (kg/m^3)	$6{,}6\times10^{-3}$
Total current (μA)	5,8			Number of injections – inlet surface	36
Number of 2-D cells	10 800				

The grid cell size was set to 0,5 mm x 0,5 mm, with refinements near the outer cylinder wall and the inner wire surface, for a total of 10 800 2-D cells.

3.1.2 Voltage-current curves

In Figure 3.1, the experimental V-I data points obtained by Zhuang *et. al.* were plotted alongside theoretical curves produced by Oglesby and Nichols (1970) (equation 2.14) and Waters and Stark (1975). The Waters and Stark equation is not presented here, but is similar in form to equation 2.14. Note that for ease of viewing the negative sign on the applied potential has been omitted from the curves in Figure 3.1. In the figure we notice that there is a discrepancy between the measured curve (triangular points) and the theoretical curves (dashed line and thick solid line) for the air load condition (no particle load).

In order to verify the theoretical curves, they were compared with experimental data from Cobine (1978), and were found to match the data. Since we are only interested in the corona current under loaded conditions at an applied voltage of -9 kV (the voltage used by Zhuang *et al*. for their efficiency measurements), we can ignore the air-load curve and use only the particle-loaded curve (thin solid line), which can be seen to be in reasonable agreement with the data at that voltage. The magnitude of the corona current at an applied voltage of -9 kV is approximately 6,5 μA, though there is most likely a large uncertainty in this value due to the fact that the applied voltage is very close to the CIV (-8,8 kV), where the corona discharge can be unstable, especially for negative corona.

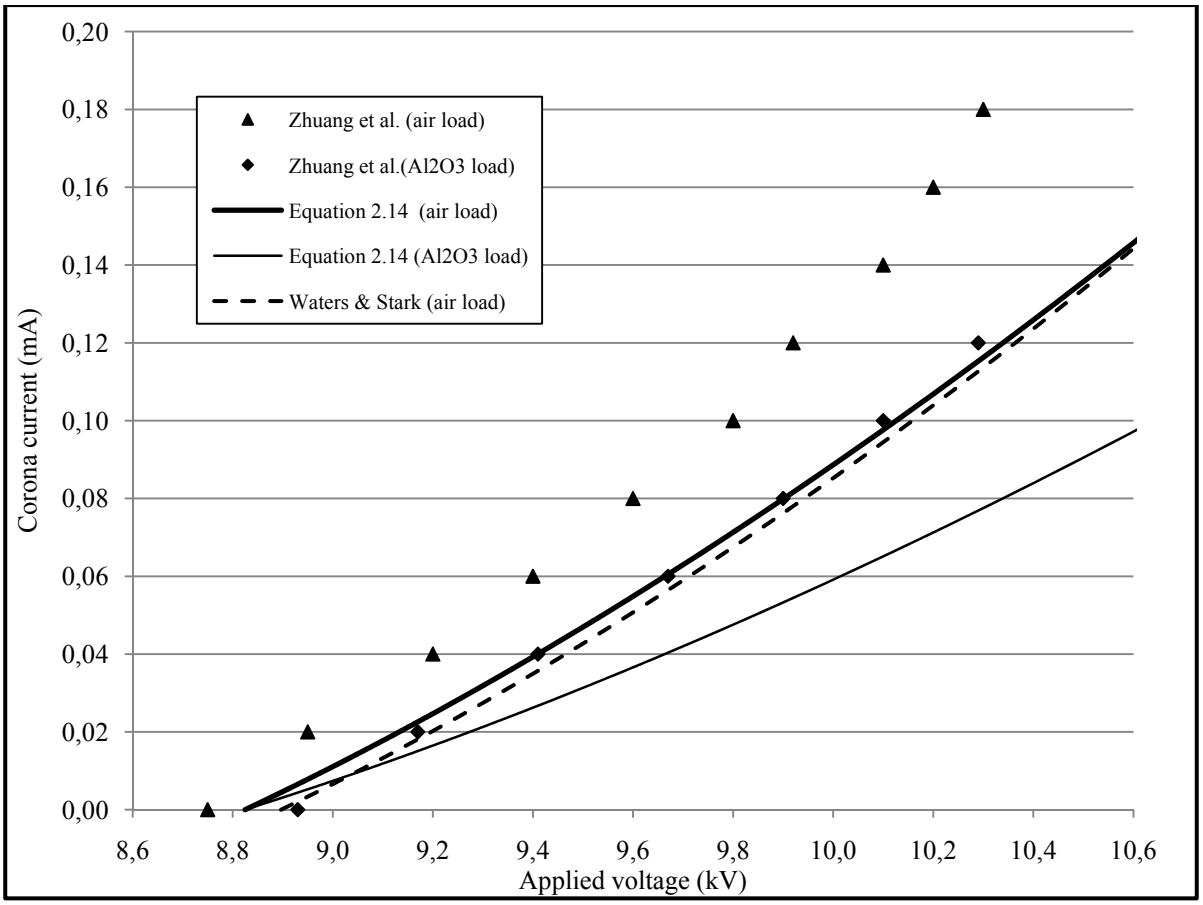

Figure 3.1 Corona current as a function of applied voltage, as measured by Zhuang *et al.* and from theoretical relations by Waters and Stark (1975) and Oglesby and Nichols (1970) for the validation model.
Data from Zhuang *et al.* (2000, p. 255, Fig. 3(b))

3.1.3 Simulation results

The validation model was simulated using the parameters shown in Table 3.1. A total of 1 000 iterations were required for convergence. Figure 3.2 shows the converged gas flow field features, namely: static pressure (Pa), axial and radial gas velocities (m/s), and the turbulence intensity (%) for the converged simulation of the validation model. Firstly it is clear that the flow field is not simply laminar, and has a rather complex distribution for all four of the variables. The reason for this complex field distribution is the coupling of the flow, electrostatic and particle variables, as described in Chapter 2 (refer to Figure 2.1). The particles are injected through the inlet on the left of the domain and are immediately

influenced by the electrostatic field and begin to deviate from their axial paths. The addition of a variable space charge due to the particles can influence the gas flow and electrostatic variables in a complex way, as seen in the CFD simulation results. For example, the gas momentum source due to the product of the ion charge density and the E-field (the $\rho_{ion}\mathbf{E}$ term in equation 2.3) acts on the gas flow to create a negative pressure zone near the inner wire. Finally, the turbulence distribution shows that its intensity is greatest in the centre of the ESP at around 10 %.

The converged electrostatic field variable distributions for the validation model are presented in Figure 3.3. Here we notice that the distributions are more uniform, especially the electric potential, which shows insignificant axial variation. The ion charge density is slightly lower on the left side of the domain, where the effect of the particle charge density is greatest.

Finally, the particle Eulerian variable distributions for the validation model can be seen in Figure 3.4. Here we can clearly see the effect of the ESP on the particles as they enter the inlet. The number concentration at the inlet was uniform at 5×10^{13} m^{-3}, but almost instantaneously the particles are forced outwards towards the outer cylinder by the effect of the electrostatic force.

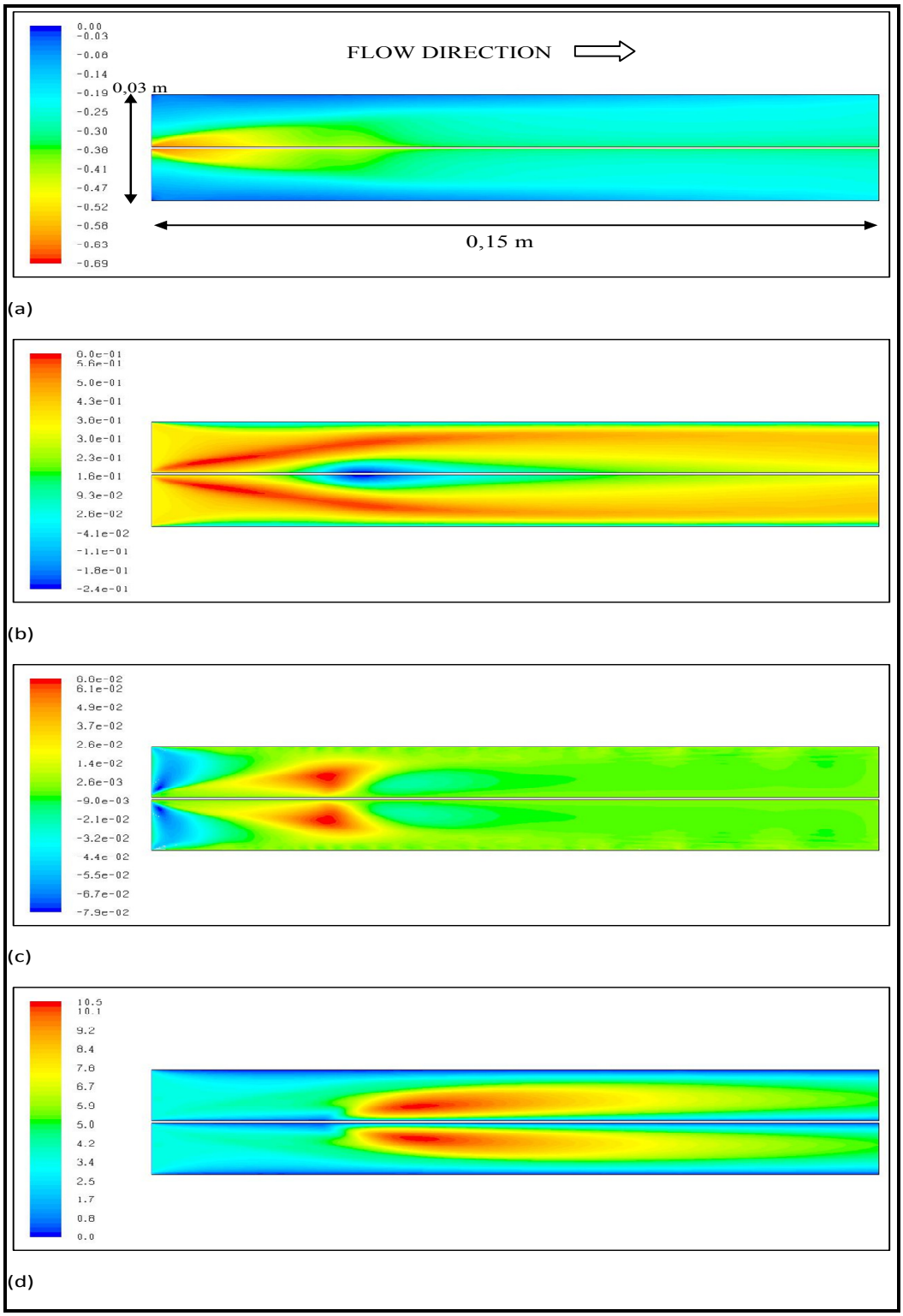

Figure 3.2 Gas flow variables for the validation model simulation: (a) Static pressure field (Pa), (b) Axial gas velocity (m/s), (c) Radial gas velocity (m/s), (d) Turbulence intensity (%).

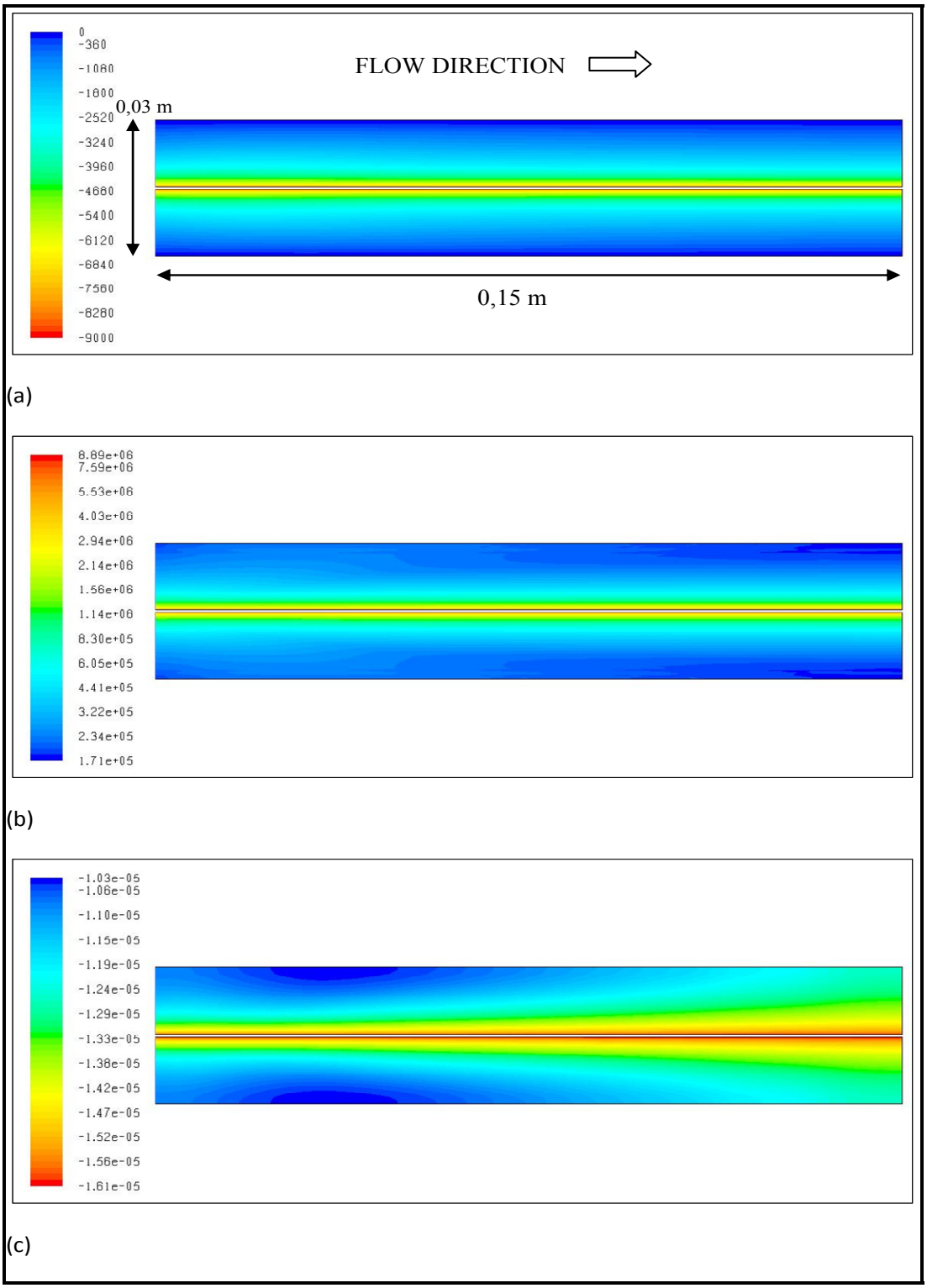

Figure 3.3 Electrostatic variables for the validation model simulation: (a) Electric potential (V), (b) Electric field strength (V/m), (c) Ion charge density (C/m^3).

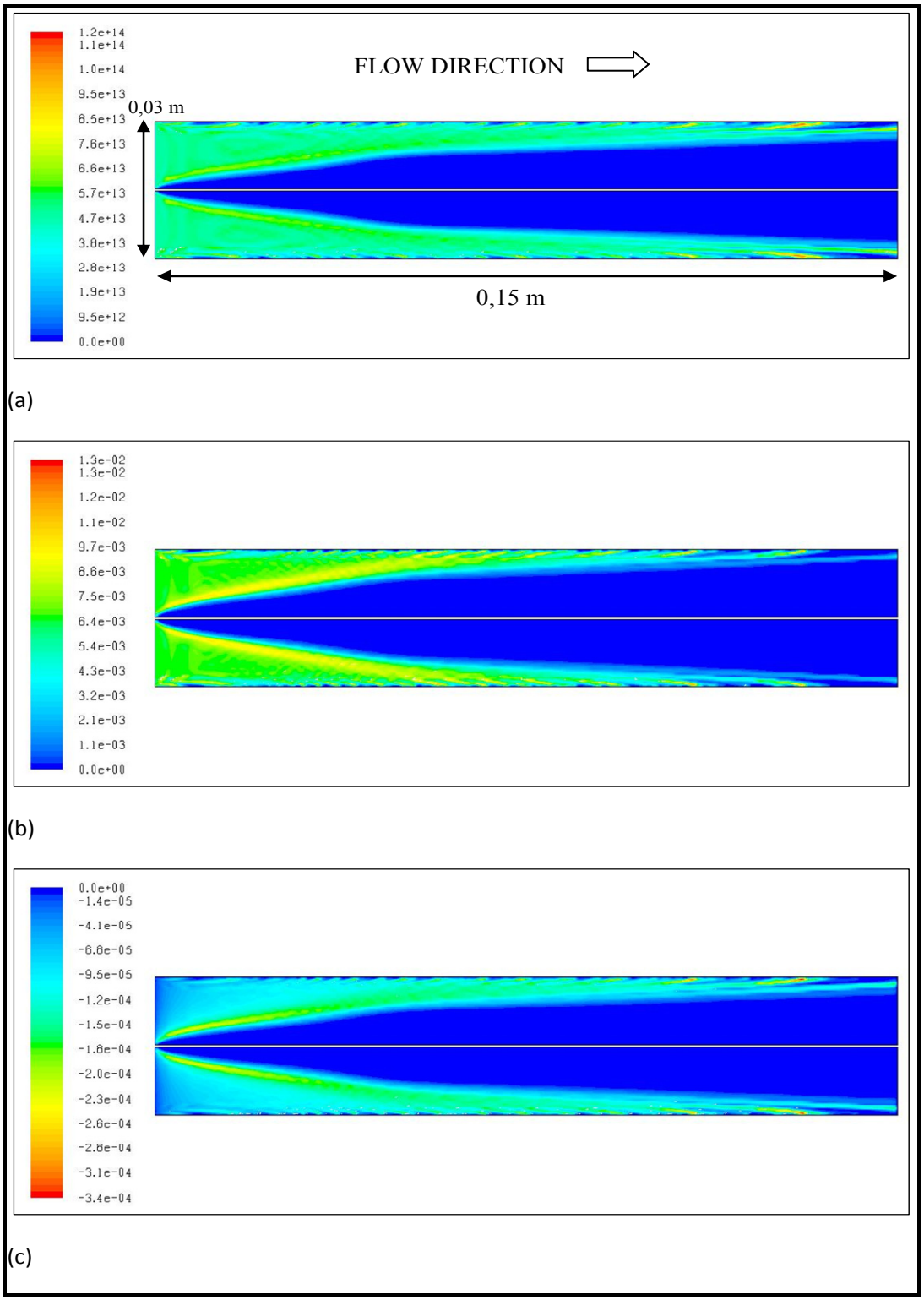

Figure 3.4 Particle Eulerian variables for the validation model simulation: (a) particle number concentration (m^{-3}), (b) particle mass concentration (kg/m^3), (c) particle charge density (C/m^3).

As can be seen, the highest concentrations of number, mass and charge are found near the inlet in a diagonal band from the inner wire towards the outer cylinder. There are also isolated accumulations of charge near the outer cylinder closer to the outlet, where the effect of the electrostatic body force on the particles is lowest, and the particles reach the gas flow velocity which approaches zero at the outer cylinder.

3.1.4 ESP collection efficiency curve

The ESP collection efficiency curve for the validation model was obtained by carrying out repeated particle injections into the converged steady-state simulation model described above, and observing the number of particles that were trapped in the ESP. This was performed for a range of particle diameters (d_p). The resulting efficiency curve was plotted alongside the experimental results of Zhuang *et al.* (2006) as shown in Figure 3.5.

Although experimental data from Zhuang *et al.* (2006) is not available beyond d_p = 0,19 μm, it can be seen that the validation model curve is within 5% of the experimental data points available for comparison. A minimum in the collection efficiency curve is observed at d_p = 0,25 μm. This is the so-called penetration window in the submicron size range that was discussed in section 1.2.4.

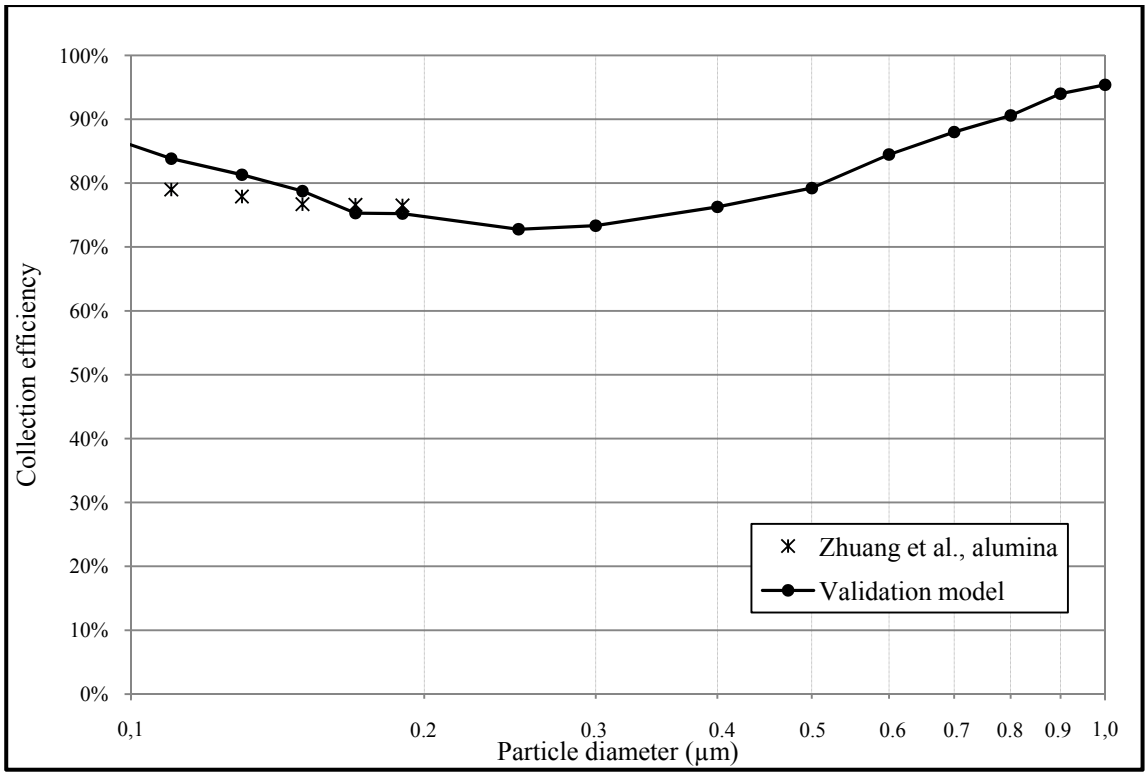

Figure 3.5 ESP collection efficiency curves as measured by Zhuang *et al.* and as obtained from the validation model simulation.
Data from Zhuang *et al.* (2000, p. 256, Fig. 4(b))

3.1.5 Variation of η_{ov} with applied voltage and gas flow velocity

Following the validation procedure, a new series of simulations were run with varying values of applied voltage and gas flow velocity in order to assess the effects of these parameters on the overall collection efficiency of the validation model, as described in section 2.2.4. A graph of the overall collection efficiency variation with applied voltage can be seen in Figure 3.6. All of these simulations had a constant gas flow velocity at the inlet of 0,53 m/s and constant turbulence intensity at the inlet of 10%. We observe that the overall efficiency increases rapidly with increasing voltage up until 9,5 kV, and subsequently the rate of increase drops off somewhat, but an efficiency of 90% is achieved at a voltage of 10,05 kV. In the opposite direction, the efficiency is expected to drop to zero at voltages equal to or less than the corona inception voltage (V_c), which is 8,8 kV in this case.

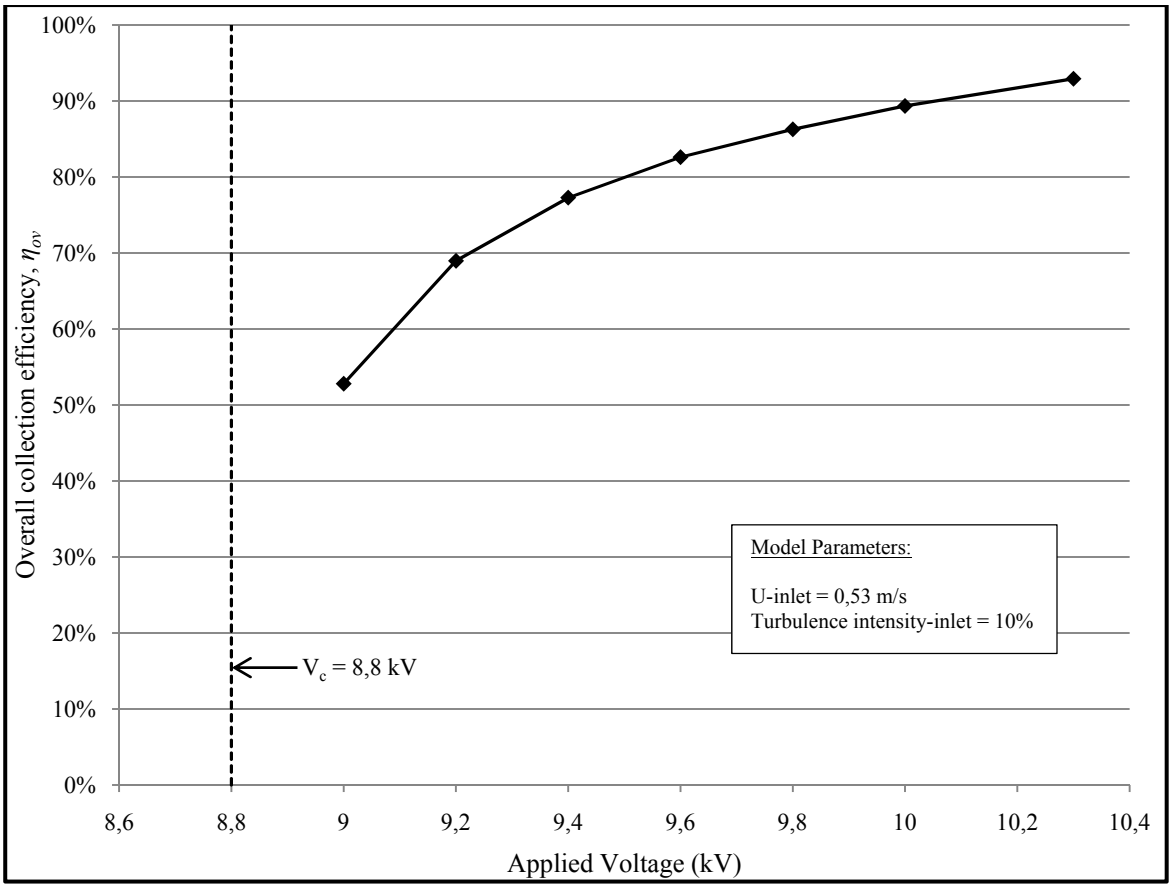

Figure 3.6 Overall ESP collection efficiency of the validation model as a function of applied voltage for the given model parameters.

In a similar fashion, the inlet gas flow velocity was varied, while keeping all other parameters fixed. The variation of overall collection efficiency with inlet gas flow velocity can be seen in Figure 3.7. We see that the overall collection efficiency is inversely proportional to the inlet gas flow velocity; the faster the flow, the lower the efficiency, as would be expected since the particles spend less time in the ESP and therefore do not reach the collection cylinder before exiting the pipe.

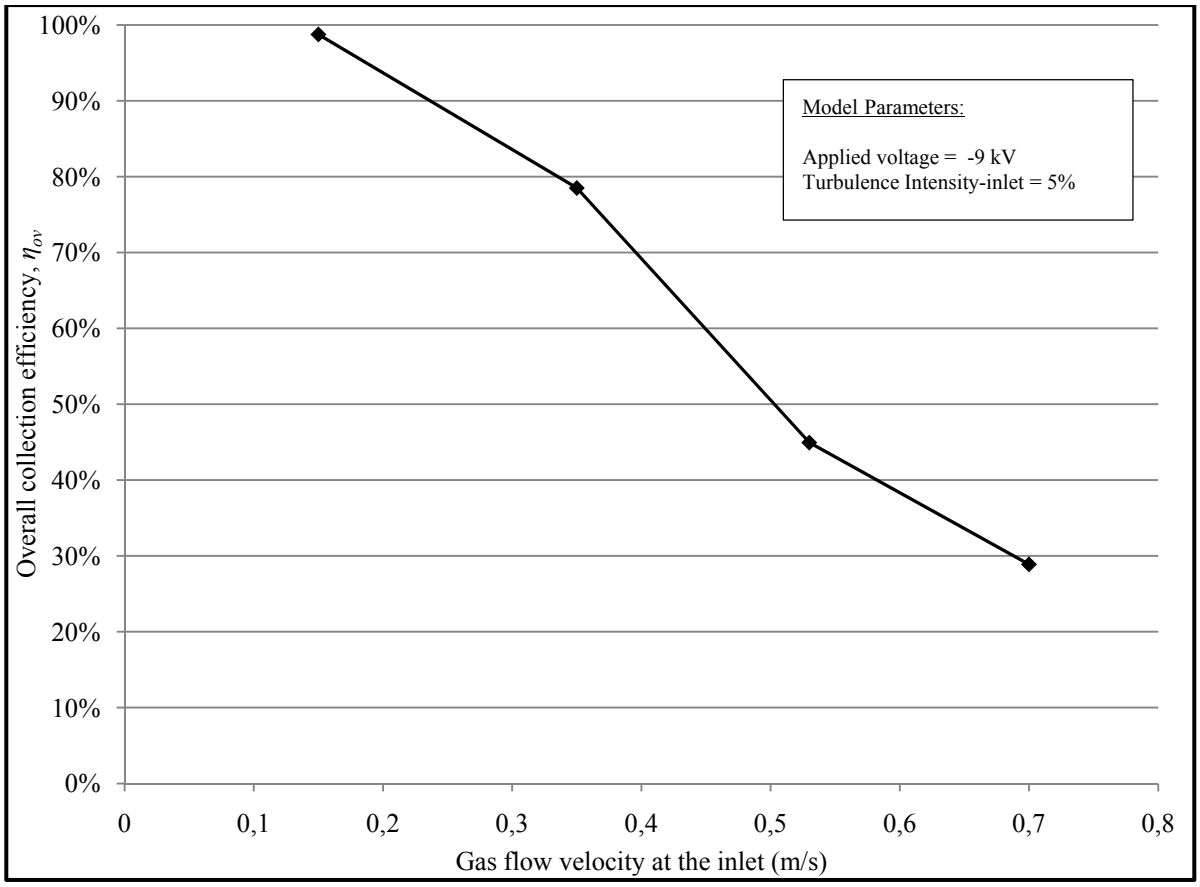

Figure 3.7 Overall ESP collection efficiency of the validation model as a function of the inlet gas flow velocity for the given model parameters.

3.2 Reference model results

The reference model was simulated in a similar manner to the validation model, as described in the previous section. This model is the simplest configuration of the 2-D axisymmetric geometry that is applicable to a residential flue pipe. The aim of the reference model is to simulate the conditions likely to be found at the top of a residential flue pipe during operation of the wood stove, i.e. a partially developed gas flow laden with combustion particles at a temperature higher than the standard temperature of 296 K. The model geometry, parameters and results of the simulations will be presented in this section.

3.2.1 Model geometry and parameters

The model geometry, constant values, initial values and particle parameters are presented in Table 3.2. The proportions of the model geometry are similar to the validation model, but scaled up to attain an outer cylinder radius of 0,075 m, which is that of a standard flue pipe. Similarly, the inner wire radius ratio was selected to maintain a ratio (R/r_w) of 100, leading to a wire radius of 7,5 x 10^{-4} m. The grid cell size was set to 2mm x 2mm, with near-wall refinements at the cylinder and inner wire surfaces, for a total of 18 375 2-D cells.

A positive wire potential was used for the reference model, since the use of negative wire potential results in a much greater rate of ozone production. The main consequence is that the positive ions produced drift towards the collection cylinder more slowly than negative ions, therefore according to Hinds (1999) the ion mobility should be reduced to a value of 1,5 x 10^{-4} m^2/V/s. This in turn reduces the ion current and hence the charging capacity of the ions at a given voltage is reduced.

Table 3.2 Reference ESP model parameters and constants

ESP MODEL GEOMETRY & GLOBAL CONSTANTS		FIXED BOUNDARY CONDITION VALUES		PARTICLE PARAMETERS	
Length, L (x-axis) (m)	0,75	U_x - inlet (m/s) U_y - inlet	0,84 (ave.) 0	Material	Soot
Height, H (y-axis) (m)	0,075	Turbulence Intensity – inlet (%)	5	Mass density (kg/m^3)	2 000
Wire radius (m)	7,5x10^{-4}	Ion charge density – wire (C/m^3)	7,5x10^{-5}	Dielectric constant, ε_r	2,4
Ion mobility, b_{ion} (m^2/V/s)	1,5x10^{-4}	Applied voltage - wire kV	+30,0	CMD (μm)	0,22
Pressure (kPa)	101	Potential – cylinder (kV)	0	σ_g	1,5
Temperature (K)	375	Corona inception voltage (kV)	+20,3	Inlet particle number density (m^{-3})	1x10^{13}
Gas density (kg/m^3)	0,94			Inlet particle mass concentration (kg/m^3)	2,8x10^{-4}
Total current (mA)	0,23			Number of injections – inlet surface	49
Number of 2-D cells	18 375				

The gas temperature of the reference model was determined by carrying out a basic CFD simulation of flue gas flowing up a vertical flue pipe 8 m tall and 0,15 m diameter. A

representative value of the gas as it exits the woodstove firebox is about 500 K according to Schmatloch and Rauch (2005). The gas is seen to cool to an average temperature of 375 K, which is the constant temperature used for this model.

Since the combustion gas from the woodstove will have travelled approximately 8 m in the flue pipe before reaching the ESP, a partially developed gas velocity profile should be used at the inlet. A graph showing the velocity profile used can be found in Appendix III.

The properties of the combustion particles, which we will call "soot" were then applied to the reference model. The values for the mass density and dielectric constant were determined from the literature and an analysis of particle composition, as described in section 1.2.2. In addition, experimental particle number distribution data from Hueglin *et al.* (1997) were analysed to determine a theoretical log-normal distribution of particles, with appropriate values for the CMD and σ_g. Graphs showing the particle number distribution and the theoretical best-fit line can be found in Appendix IV.

3.2.2 Voltage-current curves

The voltage-current relationship for the reference model was determined by applying equation 2.14, for an air load and for a particle load condition, as shown in Figure 3.8. The theoretical curve from Waters and Stark (1975) is shown for reference (air load condition only). In this case the corona inception voltage is 20,3 kV. For the particle load curve, the average space charge ratio varies with applied voltage and particle charge density, which is time-variant and also spatially non-uniform within the ESP, hence a value of 2 was used as an estimate.

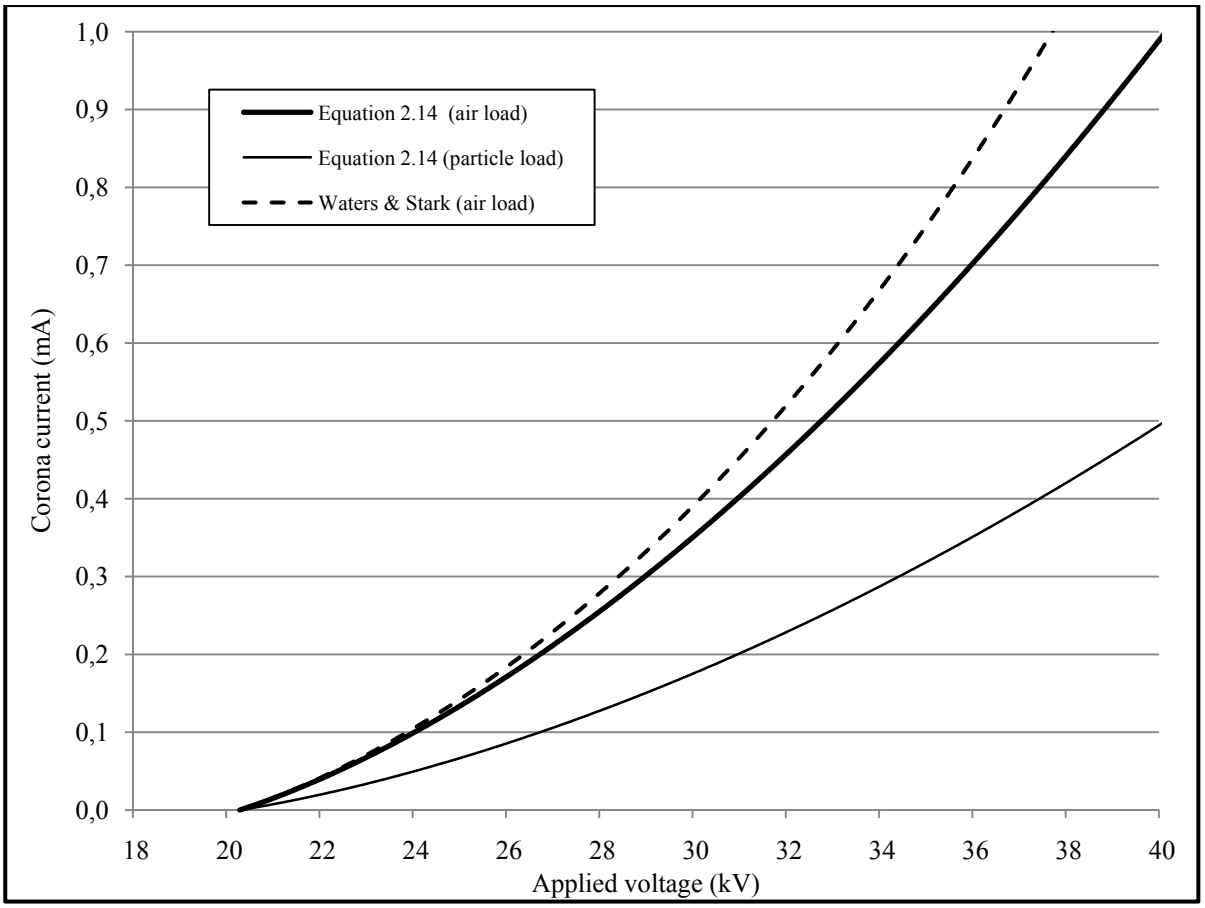

Figure 3.8 Corona current as a function of applied voltage for the reference model, from theoretical relations by Waters and Stark (1975) and Oglesby and Nichols (1970).

3.2.3 Simulation results

The graphical results of the simulation from the reference model will be presented here in the same sequence as those for the validation model (section 3.1.3). The model parameters of the simulation selected for presentation are shown in section 3.2.1.

The gas flow field results are presented in Figure 3.9. The pressure field (Figure 3.9 (a)) shows a similar gradient towards the inner wire as was seen in the validation model result. The axial gas velocity field (Figure 3.9 (b)) shows the radial profile at the inlet, which reduces to zero at the outer cylinder surface. This profile is maintained through the domain,

with some local variations in velocity. The radial gas velocity field (Figure 3.9 (c)) shows a negative region near the inlet, where the gas is moving towards the centre. Note the velocity magnitudes are small compared to the axial velocity, as expected. The turbulence intensity field can be seen in Figure 3.9 (d), and we note that most of the turbulence is found near the outer cylinder, with a maximum value of 10 % near the mid-point along the domain.

The electrostatic field variables can be seen in Figure 3.10. The electric potential (Figure 3.10 (a)) shows a smooth variation from +30 kV at the wire surface, to 0 kV at the outer cylinder. The corresponding E-field can be seen in Figure 3.10 (b), where the maximum value is $6{,}4 \times 10^{6}$ V/m at the wire surface, and the minimum is $2{,}3 \times 10^{5}$ V/m at the outer cylinder. The ion charge density is shown in Figure 3.10 (c), and is quite uniform over the length of the ESP, with a maximum value of $7{,}5 \times 10^{-5}$ C/m^3 at the wire surface.

Lastly, the particle Eulerian variables are presented in Figure 3.11. We notice here the effect of the electrostatic body force on the particle number, mass and charge density distributions through the domain. It is clear that a significant quantity of particles (and hence charge) remain in the domain and is not captured. The highest concentrations of particle mass and charge are found along the outer cylinder wall, near the inlet, where the gas and particle velocities are low, allowing particles to accumulate there. There are also zones of higher charge density in the centre of the domain, as can be seen in Figure 3.11 (c), most likely due to an accumulation of particles that were deviated from near the centre of the ESP.

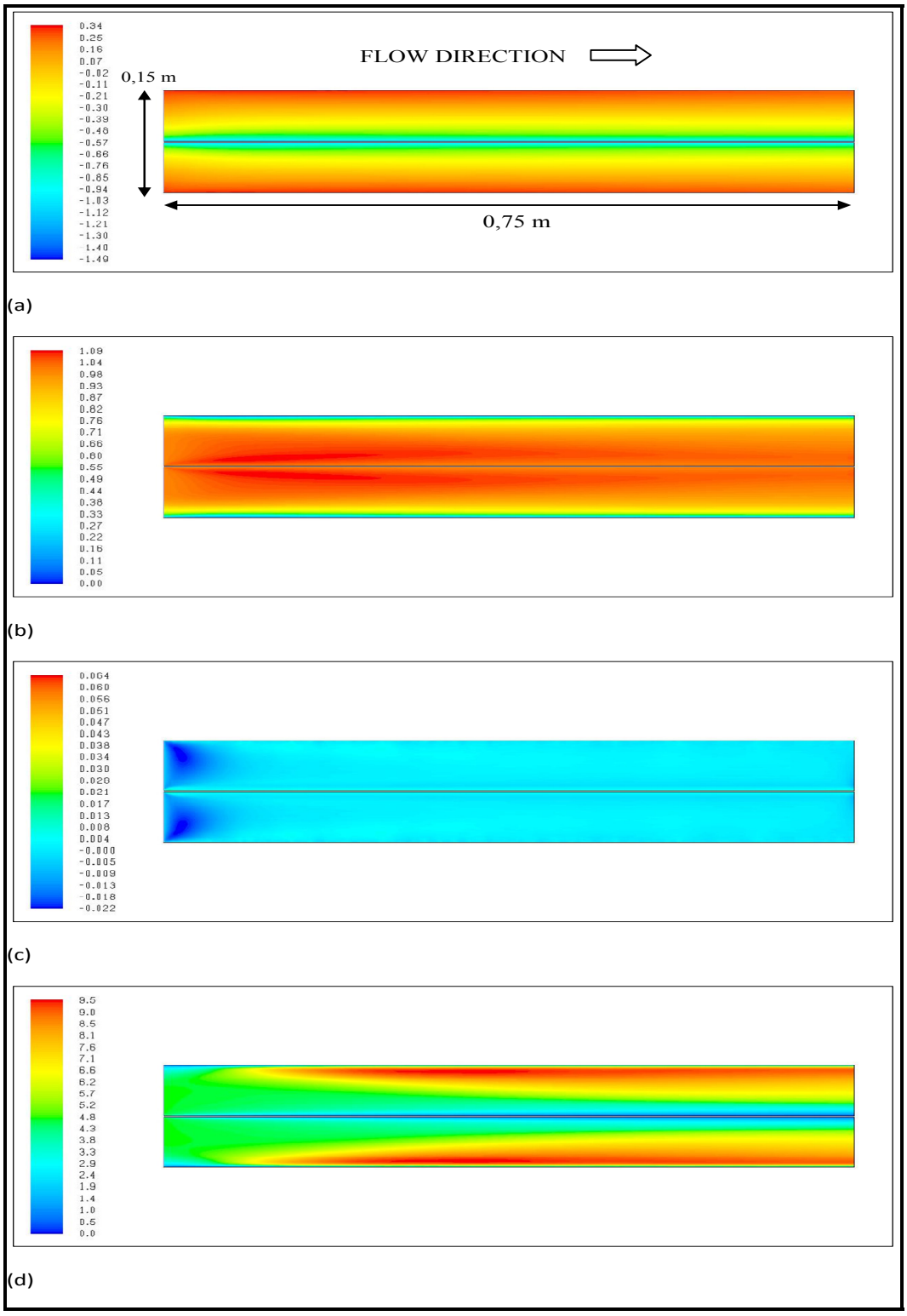

Figure 3.9 Gas flow variables for the reference model simulation: (a) Static pressure field (Pa), (b) Axial gas velocity (m/s), (c) Radial gas velocity (m/s), (d) Turbulence intensity (%).

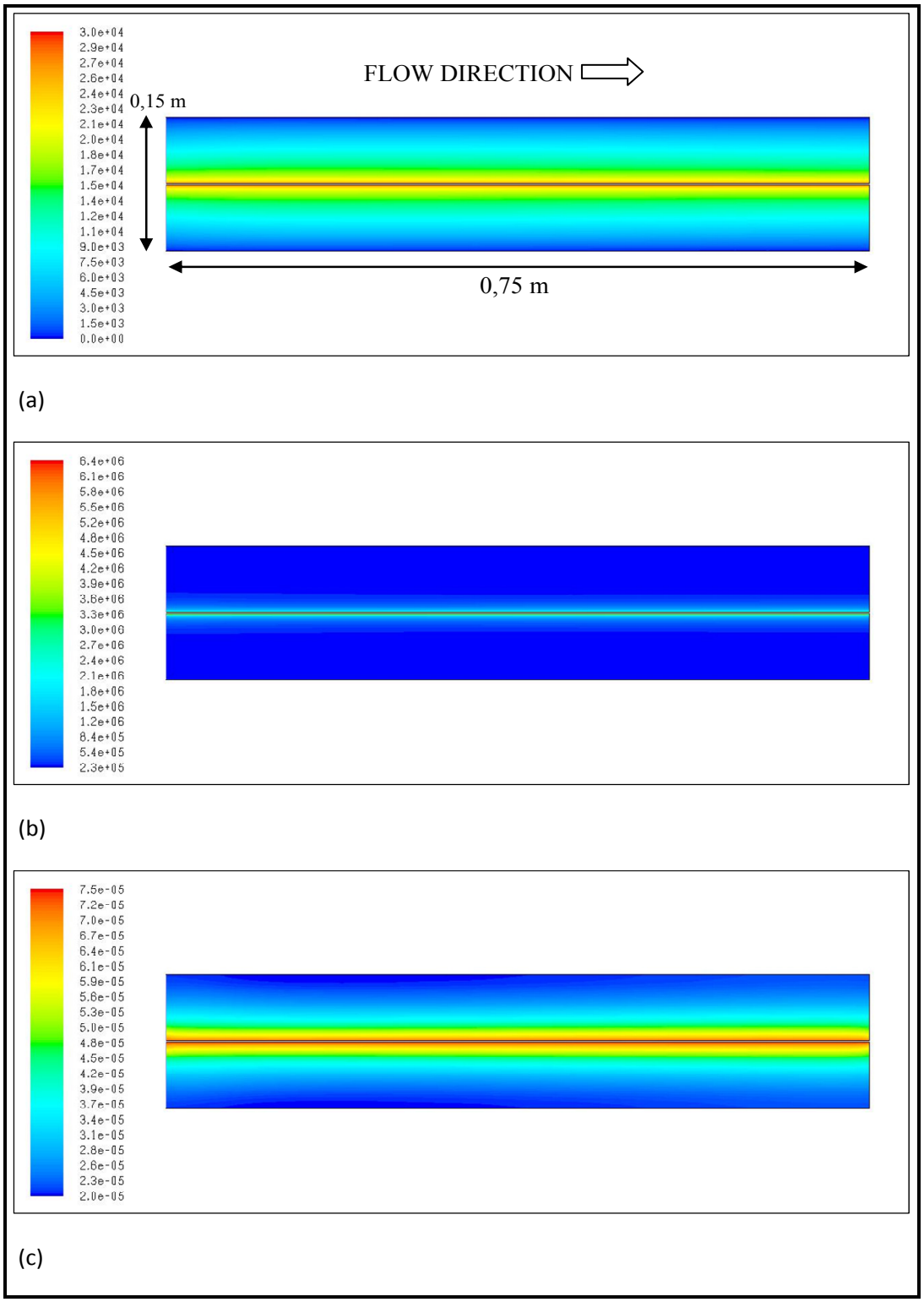

Figure 3.10 Electrostatic variables for the reference model simulation: (a) Electric potential (V), (b) Electric field strength (V/m), (c) Ion charge density (C/m^3).

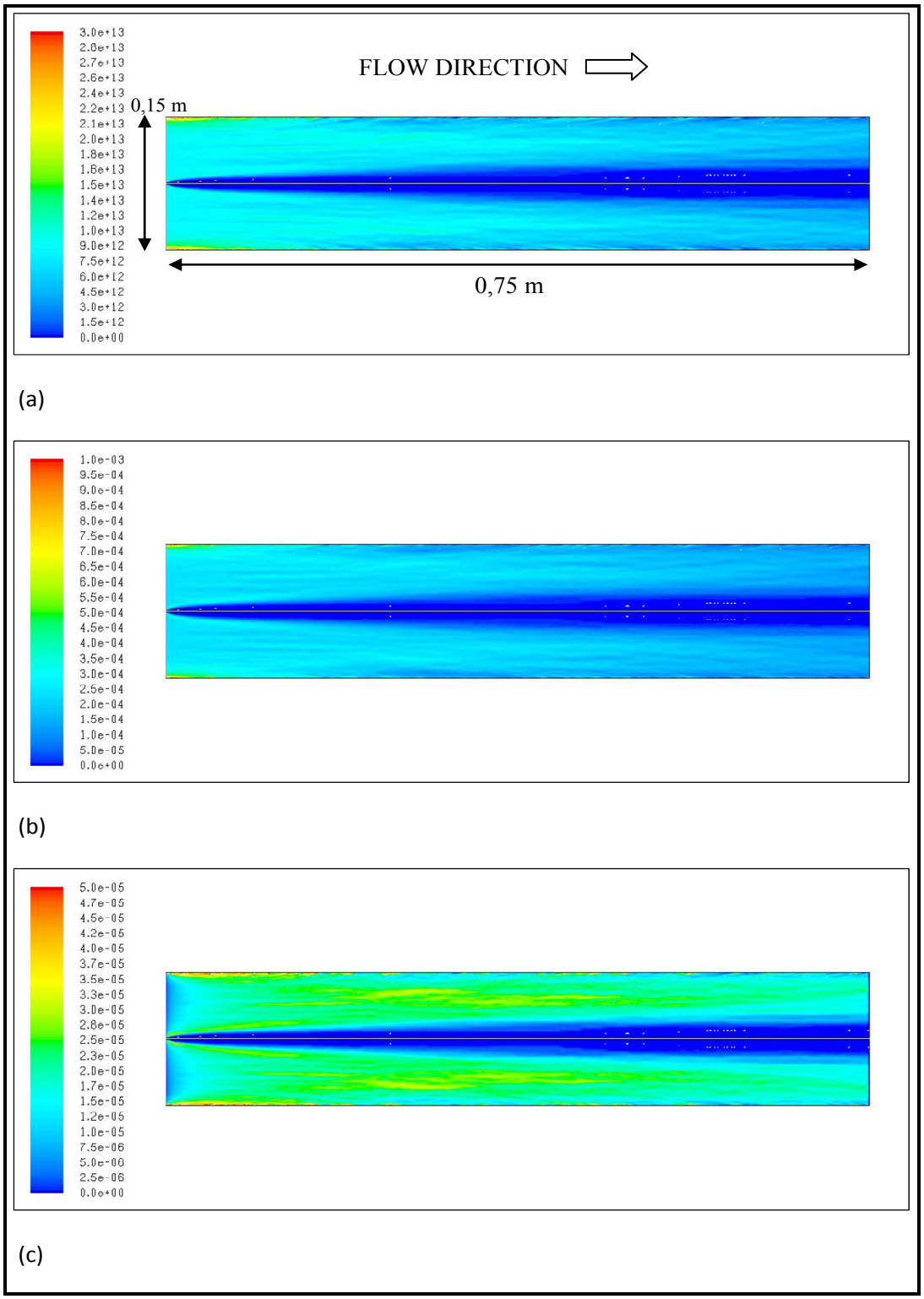

Figure 3.11 Particle Eulerian variables for the reference model simulation: (a) particle number concentration (m^{-3}), (b) particle mass concentration (kg/m^3), (c) particle charge density (C/m^3).

3.2.4 ESP collection efficiency curve

As with the validation model, the reference model ESP collection efficiency curve as a function of particle diameter was produced by injecting particle streams of each in a series of particle diameters into the converged model ESP, and counting the number of particles that were trapped by the ESP.

The range of particle sizes in the curve is from 0,1 to 1,0 µm. This size range includes over 99% of the particles (by number). The collection efficiency curve can be seen in Figure 3.12. The collection efficiency curve for the reference model at an applied potential of +30 kV and an average gas flow velocity at the inlet of 0,84 m/s is a very shallow U-shaped curve, with an average value of 47% (NFR-weighted average).

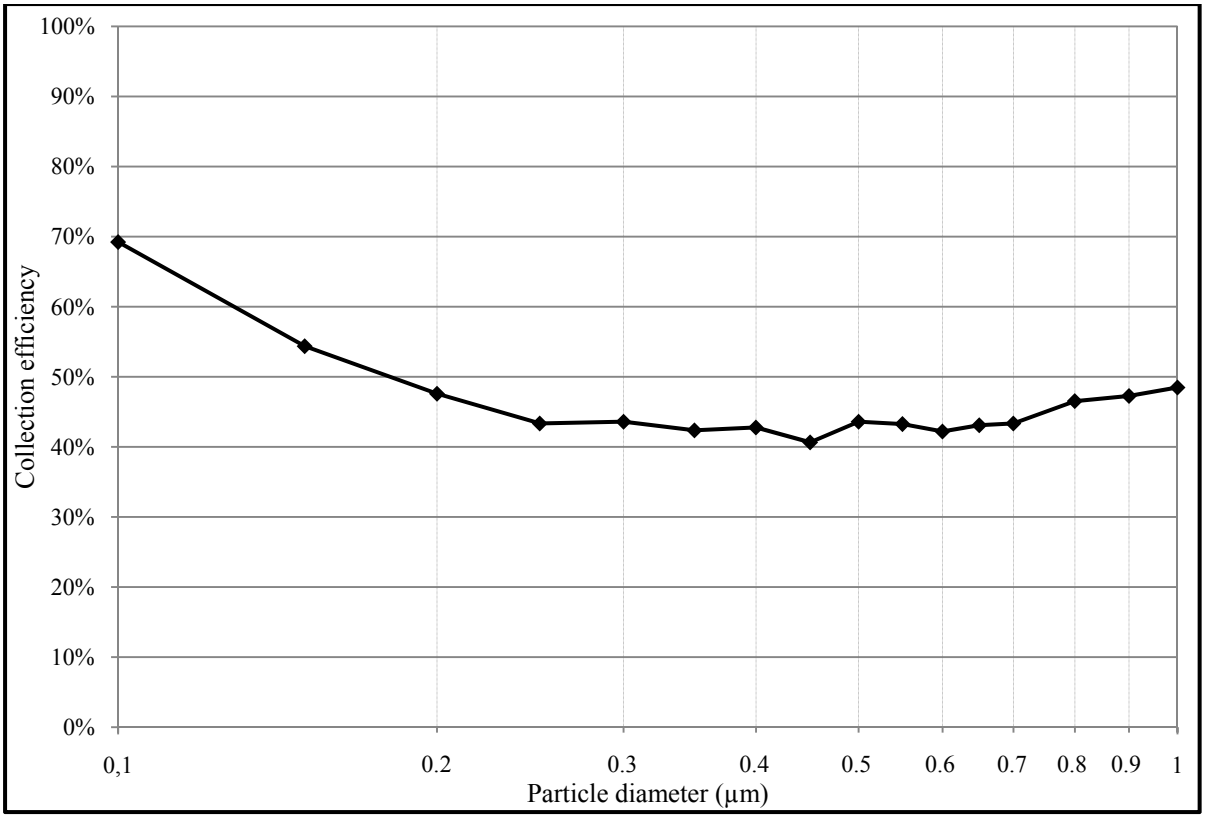

Figure 3.12 The ESP collection efficiency curve as a function of particle diameter obtained from the reference model simulation.

3.2.5 Variation of η_{ov} with applied voltage and gas flow velocity

The overall collection efficiency was calculated for a series of simulations of the reference model, in the same way as described in section 3.1.5. Firstly, the applied voltage was varied between 22,5 kV and 40 kV, and the overall collection efficiency was calculated using a weighted average based on the particle NFR. This procedure was repeated for three (3) different gas flow velocity profiles at the inlet, namely 0,21, 0,42 & 0,84 m/s on average. The resulting curves can be seen in Figure 3.13. We notice that the curve for each of the gas flow velocity profiles is very different in nature. At the lowest average velocity of 0,21 m/s, overall efficiency is high even at low applied voltage, and quickly rises to nearly 100%. In contrast, the curve for average gas inlet velocity of 0,84 m/s is almost linear from low to high applied voltage.

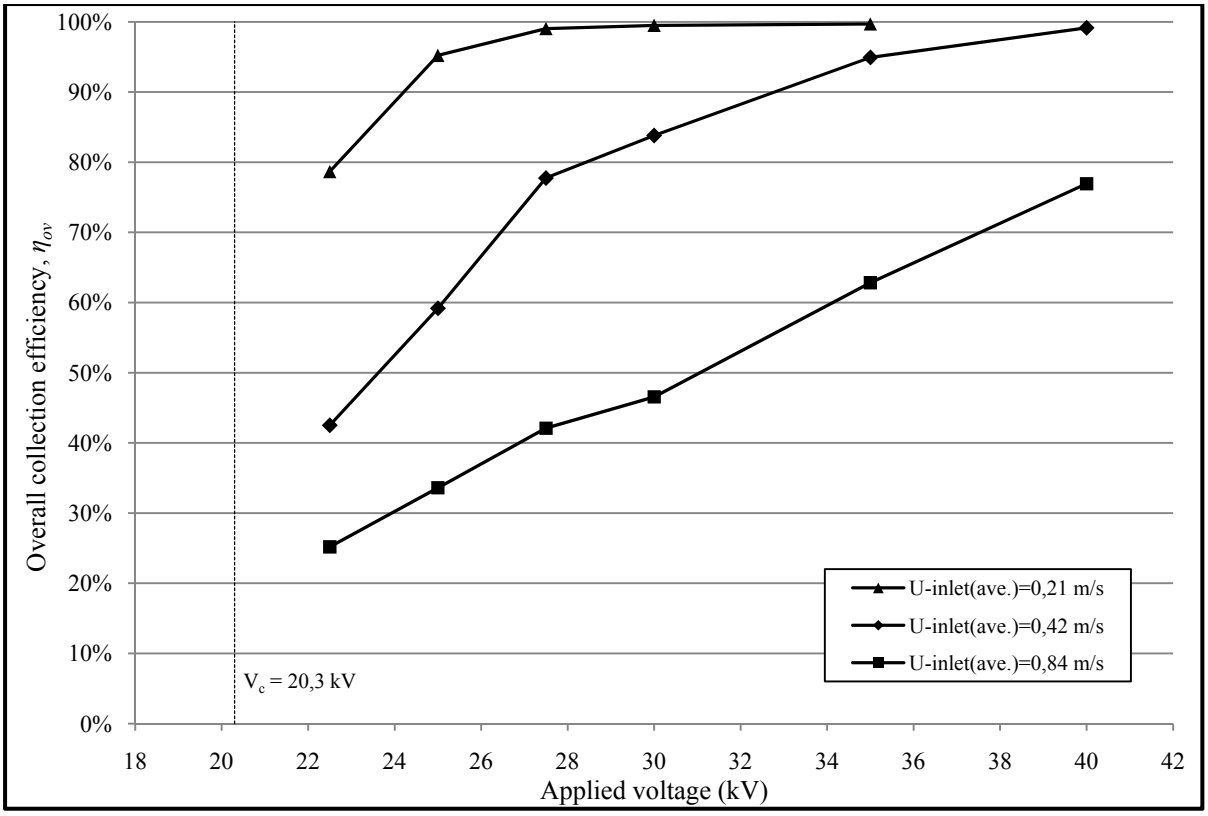

Figure 3.13 Overall ESP collection efficiency curves for the reference model as a function of applied voltage for three gas flow velocities at the inlet.

3.3 Prototype model results

The final model that was simulated in this work was the prototype model. A description of the model, along with the results of the simulations, will be presented in this section.

3.3.1 Model geometry and parameters

The prototype model was devised in order to obtain collection efficiency results for a device comprised of several ESPs working in parallel inside a standard residential flue pipe. These results can then be compared to those from the reference model to determine if such a design provides improved operational performance. Since the validation model geometry has already been simulated and was shown to obtain high overall collection efficiencies for alumina particles, it was chosen as the basic component of the prototype device. A cross-section schematic view of the proposed device can be seen in Figure 3.14. The prototype device is composed of nineteen (19) identical ESP tubes inserted into a section of standard diameter (0,15 m) steel flue pipe. The dimensions of the ESP tubes are identical to those of the validation model ESP. The gaps between the ESP tubes are left open to not restrict the flow of the flue gas and thus create a pressure differential. This will effectively limit the overall collection efficiency of the device to a maximum value of 76% (the ratio of the ESP tube area to the total flue pipe area).

It was necessary to carry out simulations at two (2) different gas inlet velocities in order to account for the gas velocity profile in the flue pipe, as described in section 3.2.1. Based on the profile shown in Figure 3.14, the majority of the flow at the inlet is constant at 1,0 m/s, and this applies to the inner core of seven (7) ESPs. Since the velocity falls off to zero near the flue pipe walls, this value is not valid for the outer layer of ESPs. The effective area-weighted average flow velocity in the outer layer of twelve (12) ESPs was calculated as being 0,77 m/s. The geometry and parameters used for the prototype model simulations are shown in Table 3.3.

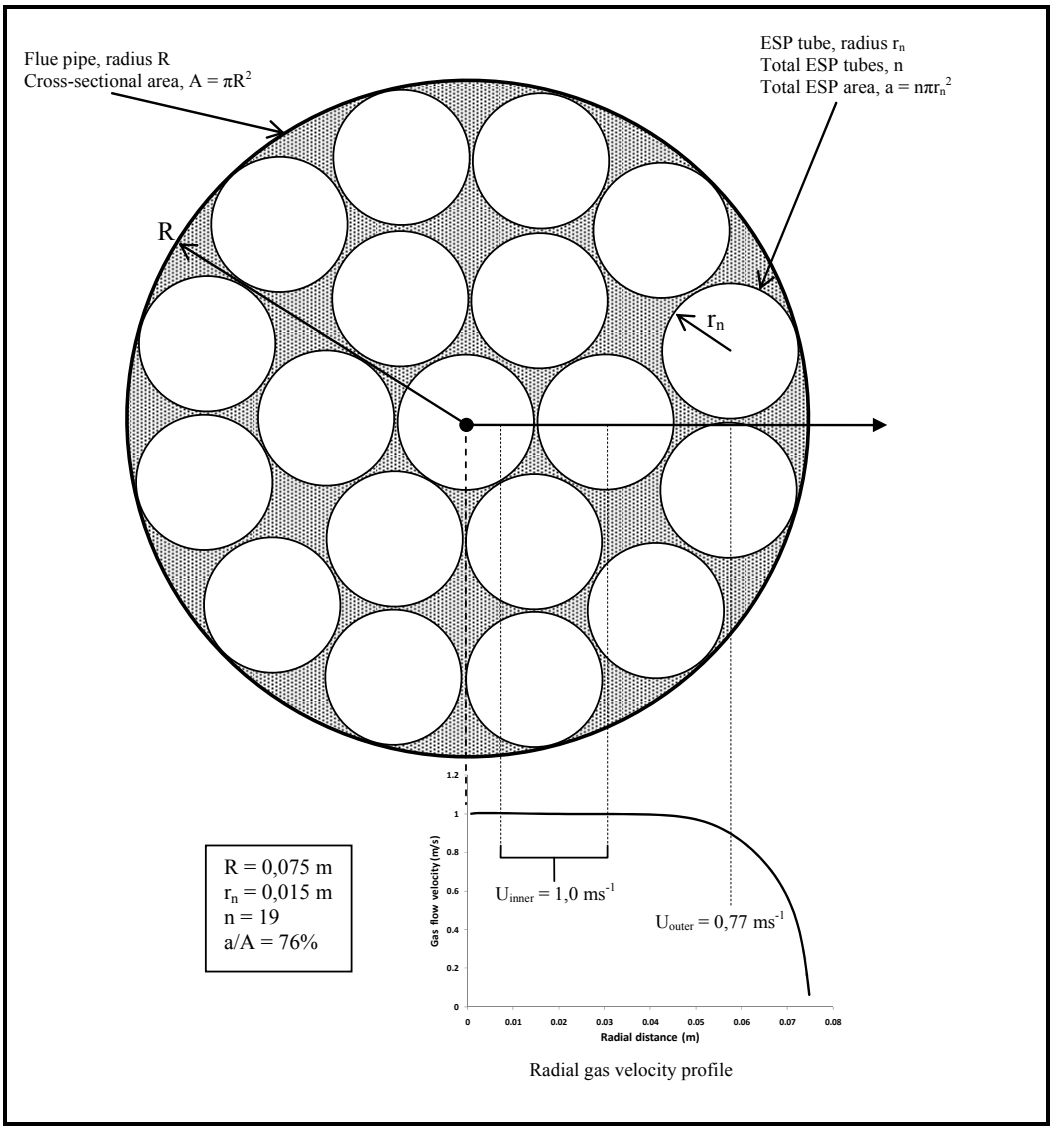

Figure 3.14 Cross-sectional view of the prototype ESP geometry, showing multiple ESP tubes inside the main flue pipe, and the gas velocity profile used in the simulation.

Table 3.3 Prototype ESP model parameters and constants

ESP MODEL GEOMETRY & GLOBAL CONSTANTS		FIXED BOUNDARY CONDITION VALUES		PARTICLE PARAMETERS	
Length, L, per ESP (x-axis) (m)	0,15	Inner ESPs: U_x - inlet (m/s) U_y – inlet Outer ESPs: U_x - inlet (m/s) U_y – inlet	 1,0 0 0,77 0	Material	Soot
Height, H, per ESP (y-axis) (m)	0,015	Turbulence Intensity – inlet (%)	5	Mass density (kg/m^3)	2 000
Wire radius (m)	2,5x10^{-4}	Ion charge density – wire (C/m^3)	5,9x10^{-5}	Dielectric constant, ε_r	2,4
Ion mobility, b_{ion} (m^2/V/s)	1,5x10^{-4}	Applied voltage - wire (kV)	+10,5	CMD (μm)	0,22
Pressure (kPa)	101	Potential – cylinder (kV)	0	σ_g	1,5
Temperature (K)	375	Corona inception voltage (kV)	+8,2	Inlet particle number density (m^{-3})	1x10^{13}
Gas density (kg/m^3)	0,94			Inlet particle mass concentration (kg/m^3)	2,7x10^{-4}
Total current (mA) Inner ESPs: Outer ESPs:	 0,13 0,14			Number of injections – inlet surface	36
Number of 2-D cells per ESP	10 800				

3.3.2 Voltage-current curves

The voltage-current curves calculated for the simulation model are shown in Figure 3.15. They are similar to those for the validation model, since the geometries are identical. The main difference is due to the different temperature between the models, which has the effect of reducing the corona inception voltage, V_c to a value from 8,8 kV to 8,2 kV. The space charge ratio applied to the particle load (thin curve) was 1,2.

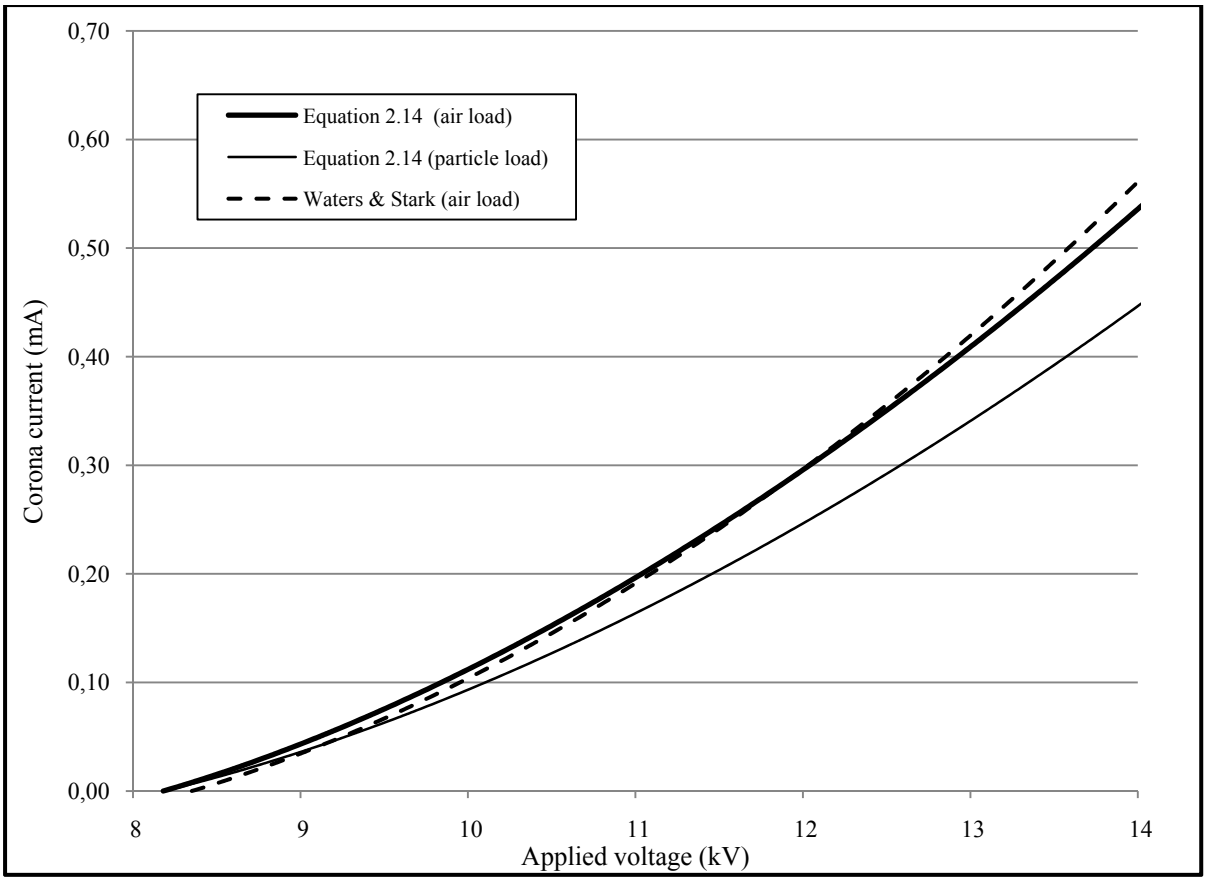

Figure 3.15 Corona current as a function of applied voltage for the prototype model, from theoretical relations by Waters and Stark (1975) and Oglesby and Nichols (1970).

3.3.3 Simulation results

Two (2) sets of simulations were carried out for the prototype model; one for each of the average gas flow velocities calculated in the previous section. Each simulation was carried out in the same manner as for those previously described. Since the differences in the field variable distributions for the two sets are small, only one set of simulation results will be displayed in this section, namely that for an inlet gas velocity of 1,0 m/s. The coloured contour results for the simulation with a gas inlet velocity of 0,77 m/s can be found in Appendix V.

The gas flow field variables for the prototype model with an inlet gas velocity of 1,0 m/s are shown in Figure 3.16. Since we have assumed a uniform inlet velocity, there is substantial variation in the axial velocity profile along the domain (Figure 3.16 (b)). Also of interest is the higher level of turbulence near the outlet of the domain, as seen in Figure 3.16 (d).

The electrostatic field variable results are presented in Figure 3.17. The profiles for the electric potential and E-field (Figure 3.17 (a) & (b)) are uniform along the domain. The ion charge density (Figure 3.17 (c)) shows some small variation near the outer cylinder, but is nonetheless quite uniform.

Finally, Figure 3.18 shows the Eulerian particulate variable results for the prototype model simulation. Of note here is the high concentration of particles (number, mass and charge) in a thin layer next to the outer cylinder, about a quarter of the way through the domain.

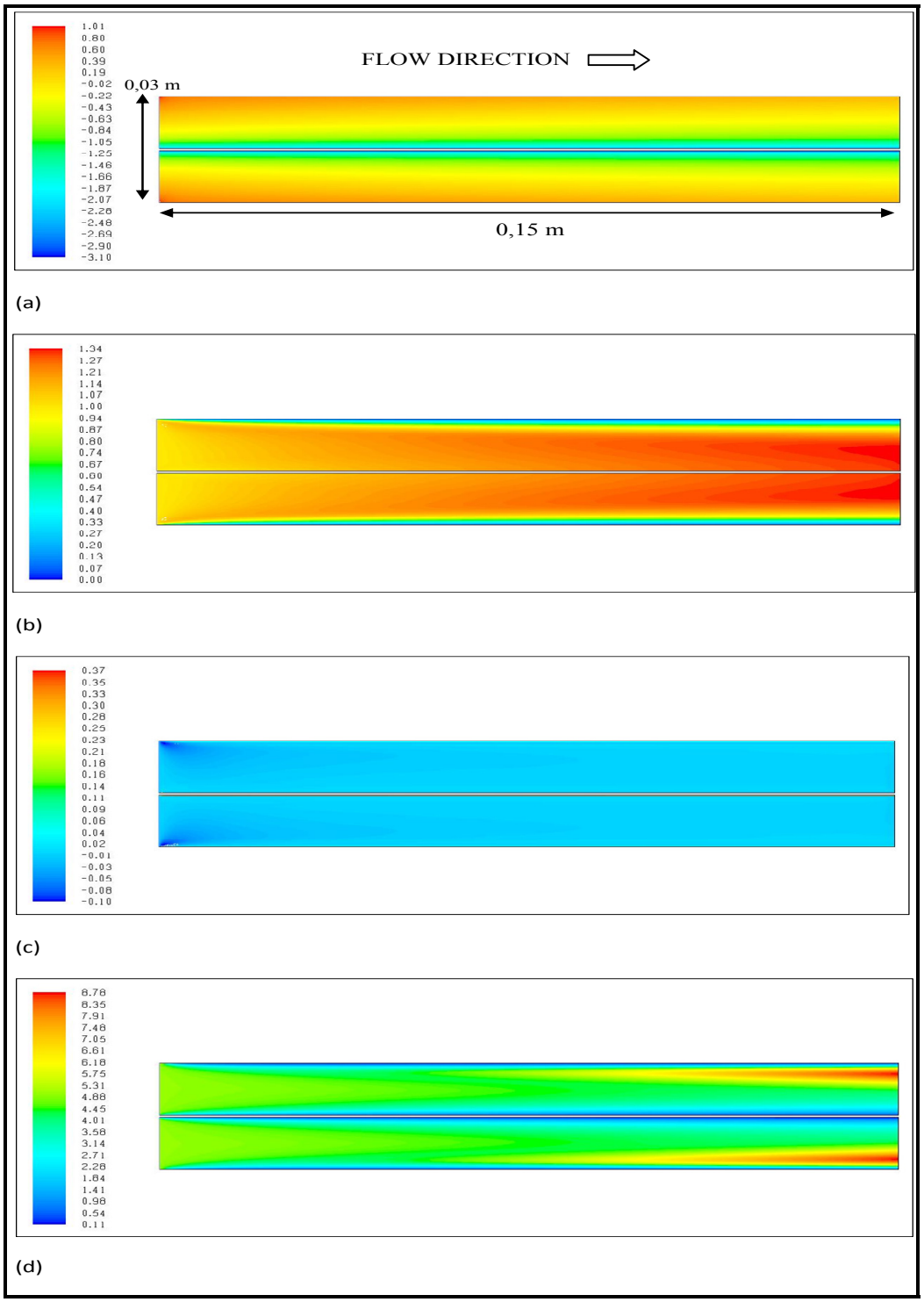

Figure 3.16 Gas flow variables for the prototype model simulation with an inlet gas velocity of 1,0 m/s : (a) Static pressure field (Pa), (b) Axial gas velocity (m/s), (c) Radial gas velocity (m/s), (d) Turbulence intensity (%).

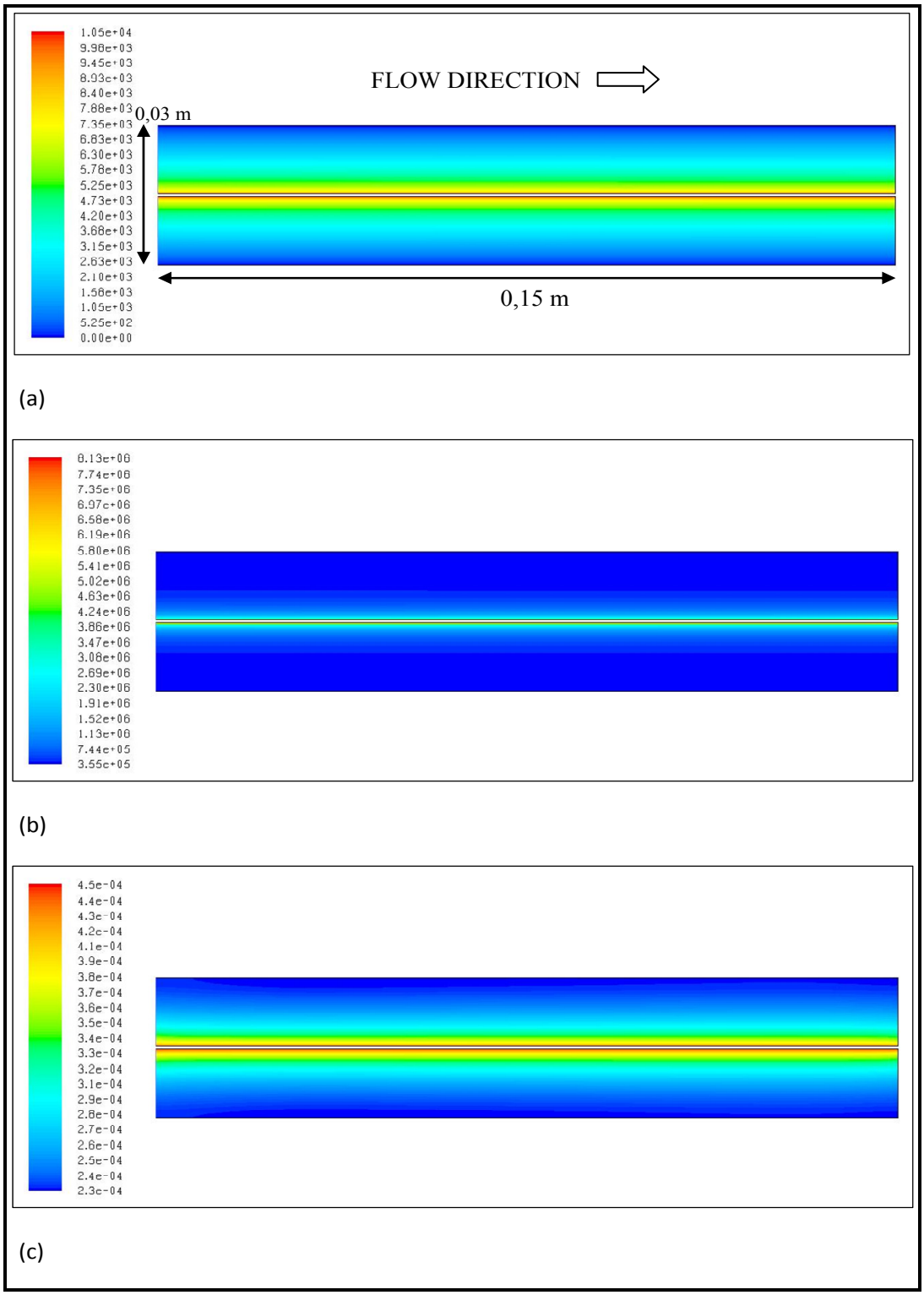

Figure 3.17 Electrostatic variables for the prototype model simulation with an inlet gas flow velocity of 1,0 m/s : (a) Electric potential (V), (b) Electric field strength (V/m), (c) Ion charge density (C/m^3).

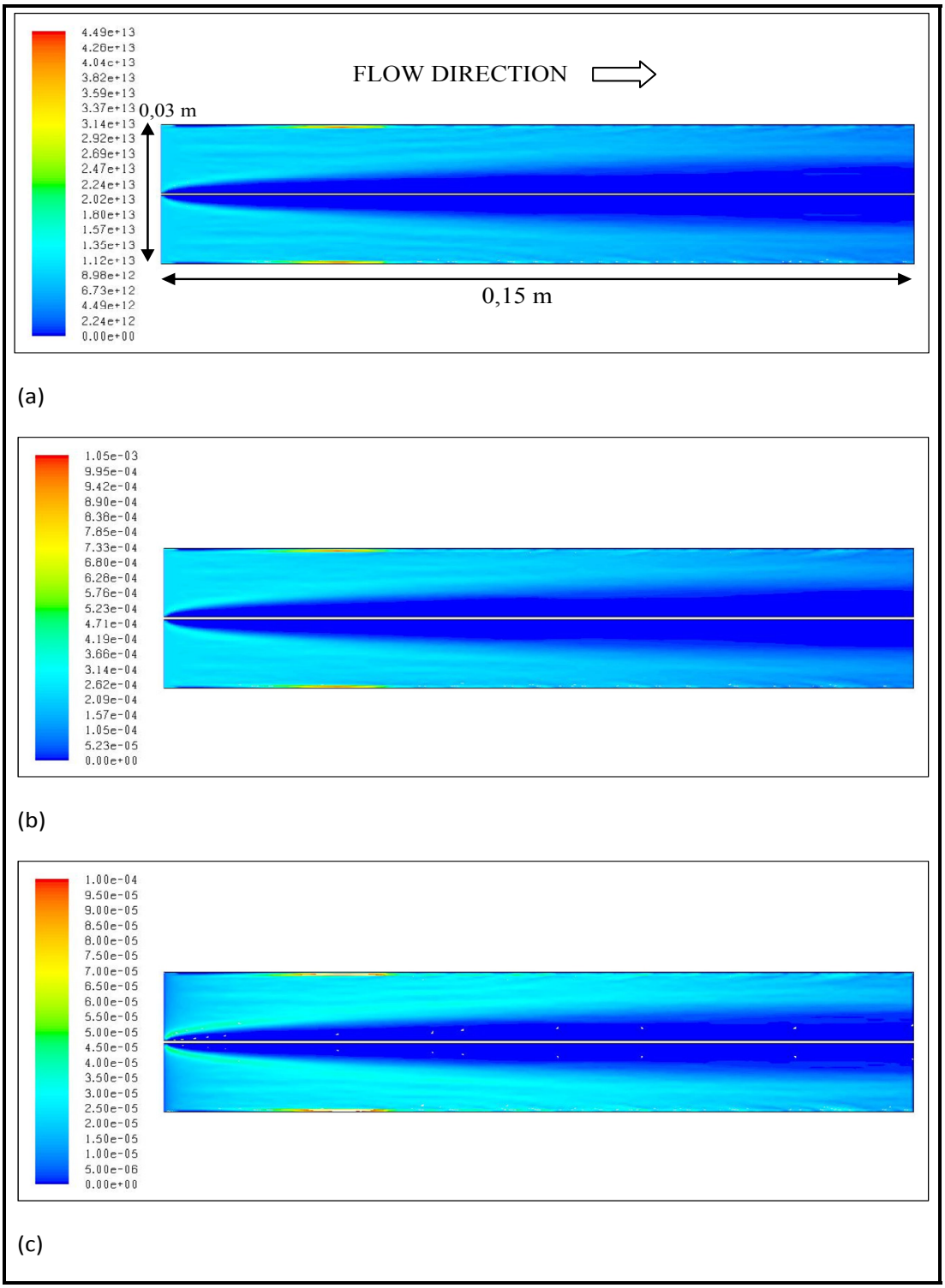

Figure 3.18 **Particle Eulerian variables for the prototype model simulation with an inlet gas flow velocity of 1,0 m/s : (a) particle number concentration (m^{-3}), (b) particle mass concentration (kg/m^3), (c) particle charge density (C/m^3).**

3.3.4 ESP collection efficiency curves

The collection efficiency curves for the prototype model simulation with an inlet gas velocities of 0,77 & 1,0 m/s can be seen in Figure 3.19. We notice the U-shaped curves, as with the validation model. The curve for the inlet gas velocity of 0,77 m/s has a minimum efficiency of 71% at a particle diameter of 0,55 μm, while the curve for the inlet gas velocity of 1,0 m/s is flat-bottomed with a minimum efficiency of 55% between particle diameters from 0,35 to 0,5 μm.

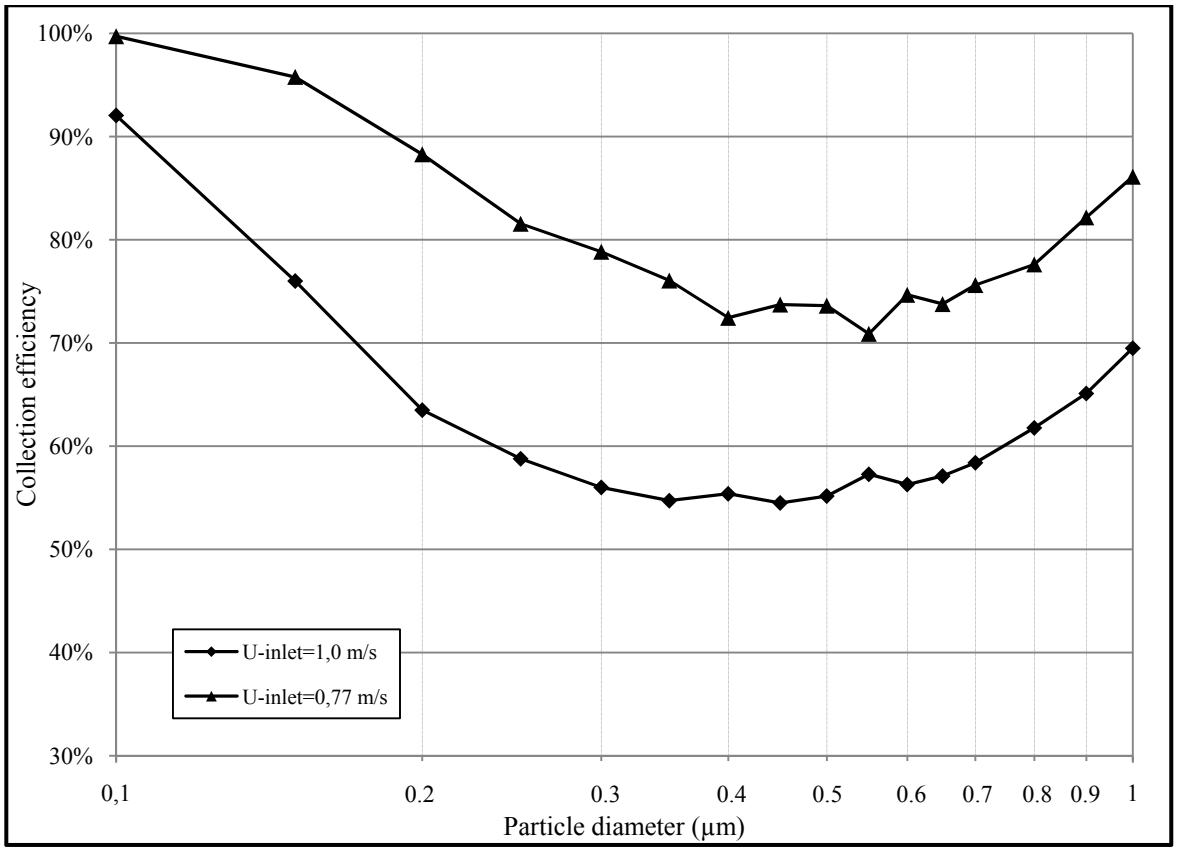

Figure 3.19 The ESP collection efficiency curve as obtained from the prototype model simulation for two inlet gas flow velocities.

3.3.5 Variation of η_{ov} with applied voltage and gas flow velocity

As with the previous models, the overall collection efficiency (η_{ov}) was calculated for each simulation in a series with varying applied voltage and gas flow velocity at the inlet. The variation of η_{ov} with applied voltage is shown in Figure 3.20. We notice that the curve for inlet gas velocity of 0,77 m/s is steeper at lower applied voltages, but reaches a plateau at higher voltages, greater than 11,5 kV. The curve for inlet gas velocity of 1,0 m/s is more linear and only begins to flatten out slightly above an applied voltage of 10,5 kV.

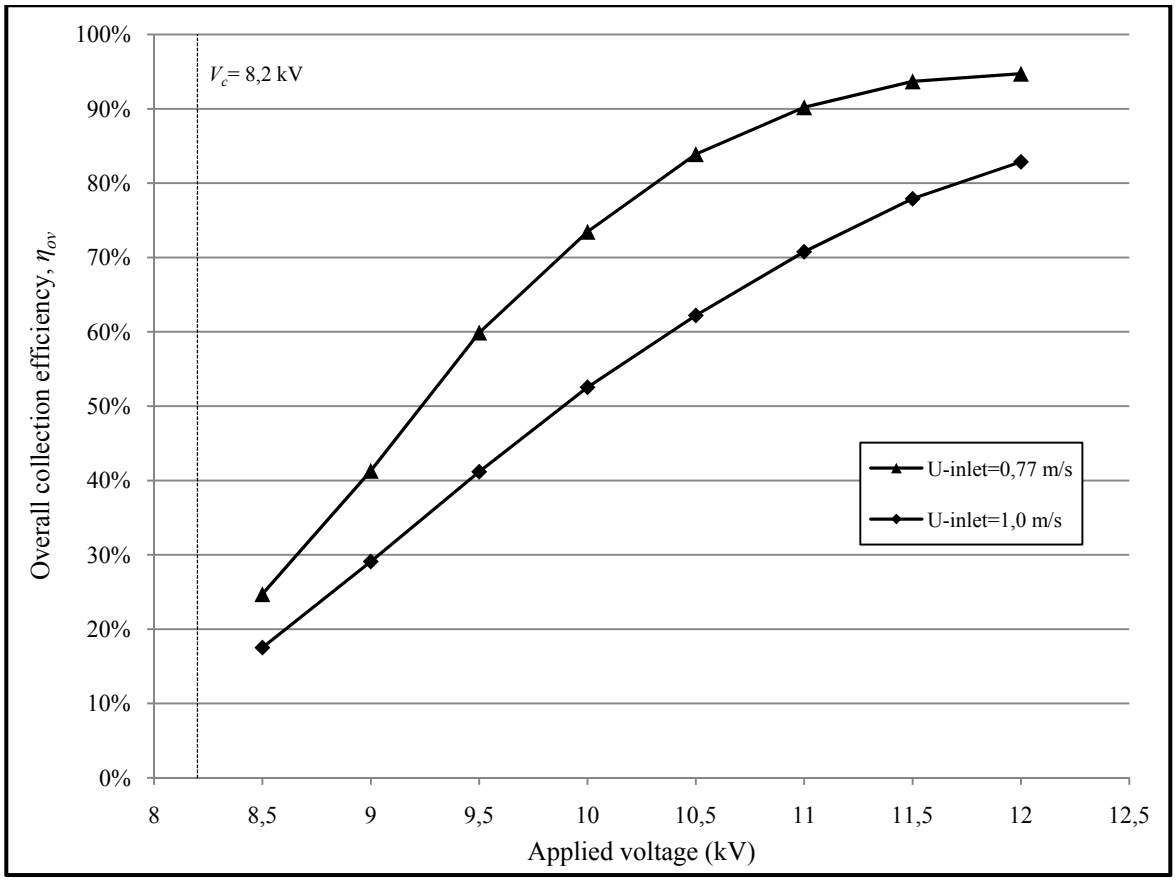

Figure 3.20 Overall ESP collection efficiency of the prototype model as a function of applied voltage for the two simulations with inlet gas velocities of 0,77 and 1,0 m/s.

The variation of η_{ov} with inlet gas velocity for an applied voltage of 10,5 kV is shown in Figure 3.21. The overall collection efficiency is seen to decrease with increasing gas flow

velocity at the inlet, in a similar fashion to the validation model simulation. This is caused by the reduced residence time of the particles in the ESP allowing them to escape before they can migrate to the collection cylinder.

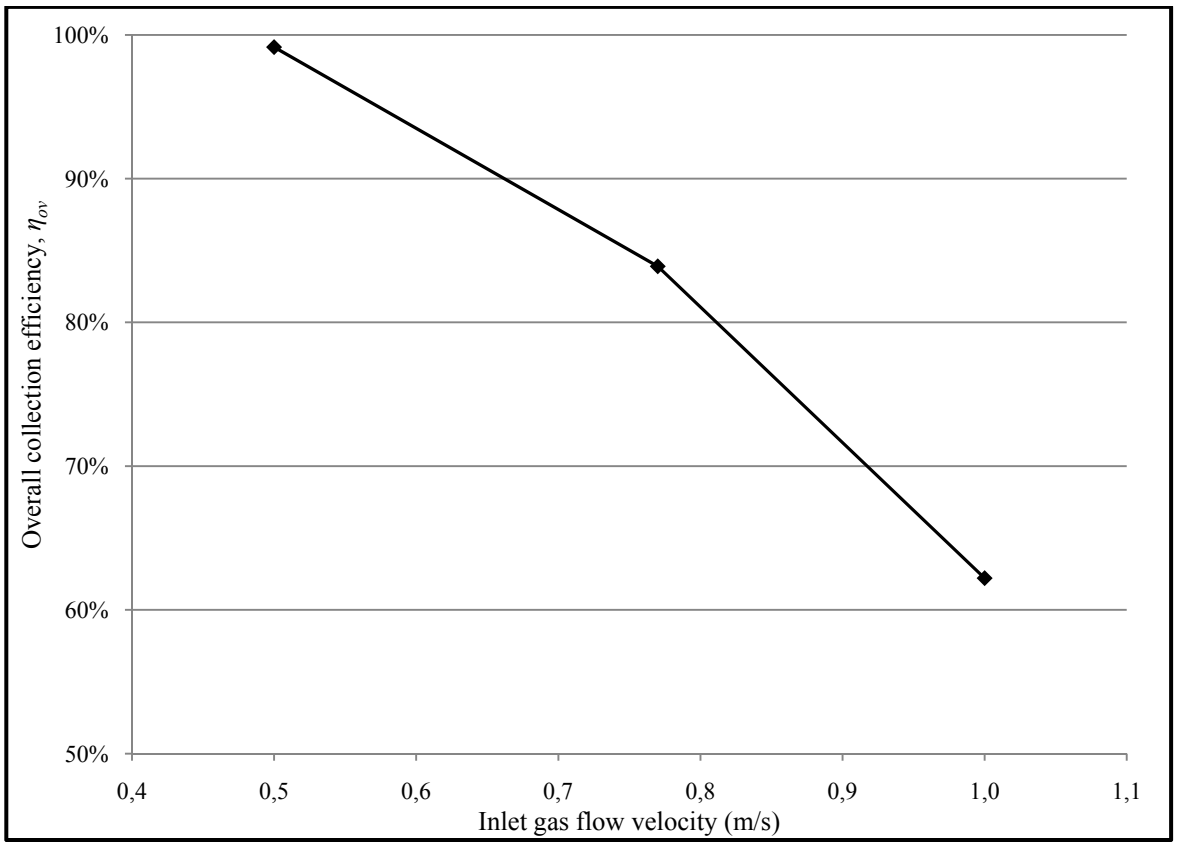

Figure 3.21 Overall ESP collection efficiency of the prototype model as a function of the average inlet gas flow velocity for an applied voltage of 10,5 kV.

3.3.6 Total performance characteristics of the prototype model

The total performance characteristics of the prototype model described in section 3.3.1 will be presented in this section. The total performance is the combined overall collection efficiencies for the two simulations having inlet gas flow velocities, 1,0 m/s for the inner section, and 0,77 m/s for the outer section, as described previously. The total performance of the prototype ESP device was calculated using an area-weighted average method. The total efficiency of the device as a function of applied voltage is shown in Figure 3.22. The

efficiency curve climbs steadily with increasing applied voltage, and begins to flatten out above 10,5 kV. An increase in voltage from 11,5 to 12,0 kV results in only a 2,1% increase in efficiency. The maximum possible efficiency for the prototype device is 76 % as described previously.

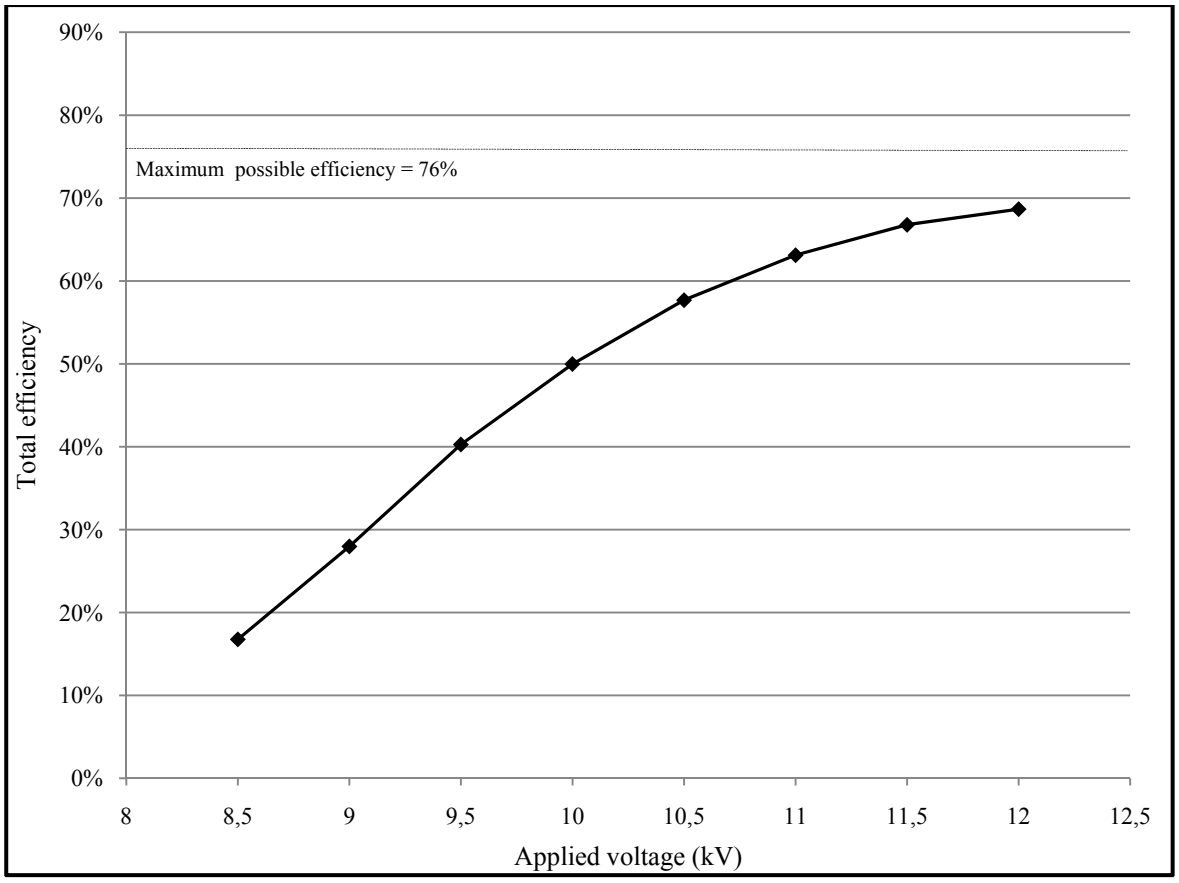

Figure 3.22 Total ESP collection efficiency of the prototype device as a function of the applied voltage, based on a velocity profile with a maximum value of 1,0 m/s.

3.4 Model performance comparison

Since the reference and prototype models operate at different applied voltages, the overall efficiency curves cannot be directly compared as a function of voltage. A useful approach to compare the models' performance is to calculate the total power consumption for each from its current and voltage parameters, and then to plot the overall efficiency curves on a single

graph. A curve showing the relation between total efficiency and power consumption for both models is shown in Figure 3.23.

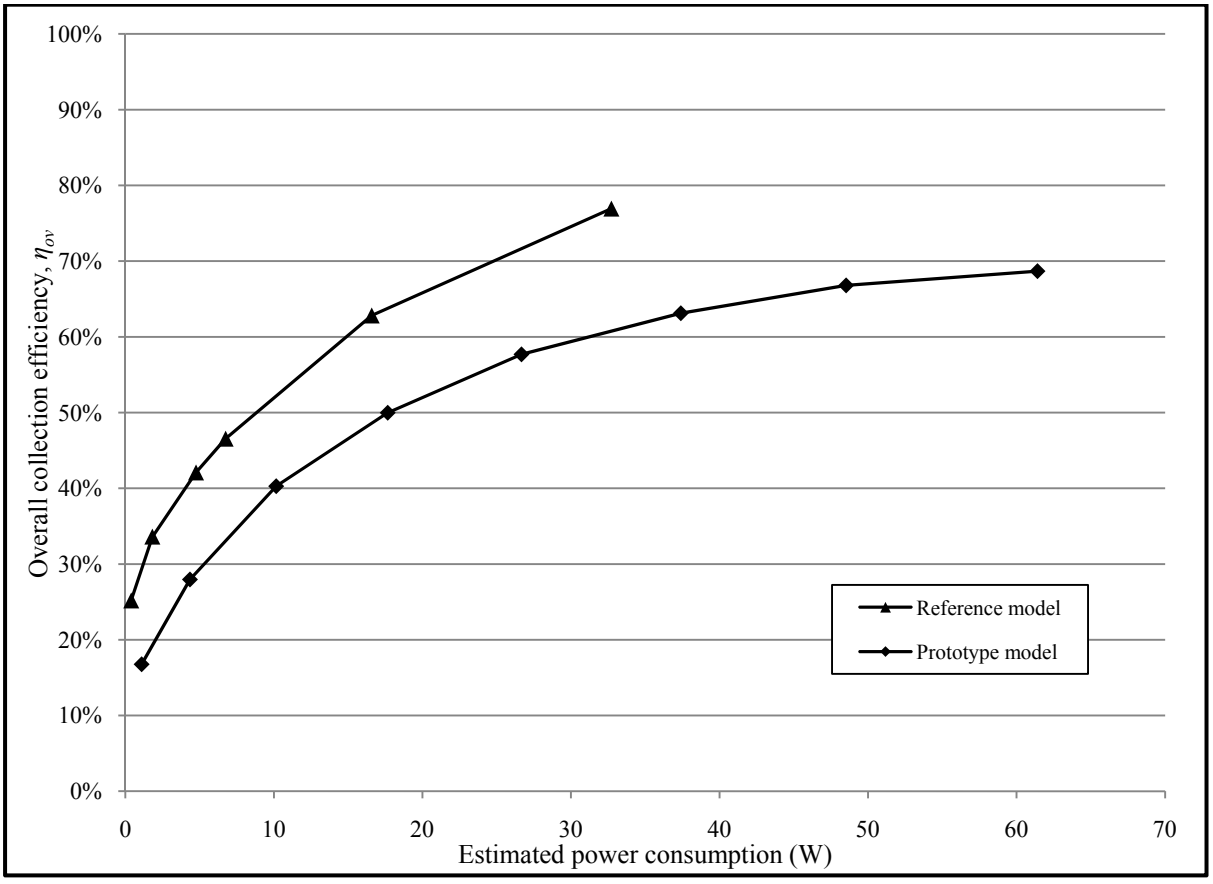

Figure 3.23 Overall ESP collection efficiency as a function of the estimated power consumption for the reference and prototype models, based on a velocity profile with an average value of 0,84 m/s.

Both the curves have a similar shape, being steep at lower power consumption, but flattening out at higher power levels. The main difference is that the overall efficiency of the reference model is approximately 15% higher than that of the prototype model for all power levels. In addition, for the prototype model, a 6% increase in total efficiency (from 63% to 69%) requires a 64% increase in total power consumption (from 37 to 61 W).

CHAPTER 4

DISCUSSION

4.1 Modeling techniques

The aim of this study was to investigate the performance of a wire-cylinder ESP for PM emissions reduction in small-scale wood stove installations. The majority of the research literature concerning ESPs is concerned with their operation in large industrial-sized systems such as those used in coal-fired power stations worldwide. So, in a sense the challenge of this study was to develop an improved modeling technique and apply it at a suitable scale and geometry, using an appropriate type of particulate matter. Most studies use fly-ash from pulverised coal burning, where only 5% of particles are smaller than 2 μm in diameter according to Parker (2000) and has physical properties that are better known than those of PM produced by wood burning stoves, most likely due to greater research funding provided by the power generation industry.

A number of refinements were made to the simulations in this study in order to improve the accuracy of the results compared to similar modeling studies that focussed on fly-ash particle capture. Firstly, the model employs a poly-disperse particle distribution based on experimental data instead of a simplifying mono-disperse distribution of particles, as used by Skodras *et al.* (2006) and Choi and Fletcher (1997) for example. The use of a more realistic poly-disperse particle distribution in the model means that the particle charge distribution within the domain is more accurate, and likewise for its effect on the electrostatic field and gas flow variables.

Secondly, the simulations in this study take into account the effects of non-standard temperature conditions likely to be found in a real ESP device as opposed to standard temperature and pressure conditions assumed in the studies mentioned above. The effects of higher temperature include: decreased corona initiation voltage, decreased gas pressure, increased gas viscosity and increased Cunningham slip correction factor. Each of these

factors will produce an effect on the overall ESP performance, thus leading to a more accurate model.

The model also made use of more accurate physical properties of the particles. When available, they are based on published studies and not merely assumed without justification as in other studies (such as the mass density for example). Obviously, a precise knowledge of the properties of PM produced by wood burning is essential for an accurate simulation. As discussed in Chapter 2, however, the constituents of these particles are rather complex organic molecules many of which remain unidentified, and hence some simplifications had to be made for this simulation.

The reference model employed a partially-developed gas flow velocity profile at the inlet, as opposed to a constant velocity. Such a profile is observed to develop in any duct flow situation, and thus represents a refinement over a constant velocity that is used in other studies. The obvious effect of this on ESP performance is that particles will slow their axial velocity as they approach the outer wall of the ESP. Thus, the probability of a particle being captured (hitting the outer collection cylinder) increases as its axial velocity decreases since the electrostatic body force has more time to act on the particle. This also leads to an accumulation of particles near the outer wall, and hence an accumulation of charge which can affect the electrostatic field and ion current flow.

Finally, the simulations employ a sum-of-charges particle charging model that combines the diffusion and field charging mechanisms. This model has been shown by Lawless (1996) to fit experimental data at least as well as several more sophisticated charging schemes. The inclusion of diffusion charging is essential for the modeling of sub-micron particles or even particles below 5 μm in diameter since the diffusion charging component is not negligible for these sizes. However, often modeling studies dealing with fly-ash tend to neglect the diffusion charging component.

Despite the refinements to the model and simulation technique described above, it must be borne in mind that no simulation of complex interdependent systems such as those operating within an ESP can ever perfectly describe it. Due to the random nature of turbulence, the variable nature of the corona discharge and the transient nature of the particle charge density there is always likely to be some discrepancy between experimental results and the simulations.

There are a number of possible factors that can influence the simulation results. Most are real (physical) factors such as the temperature or inlet gas velocity for example, but others are artificial effects caused by the way the numerical simulation is designed and run. One such factor is the grid cell size of the domain. If the cell size is too coarse, important features in the simulation may not appear, or even worse that artificial features are introduced into the results. The cell size employed in this study was chosen by comparing similar studies and limited by the available computer processing power. The study by Skodras et al. (2006) initially employed a grid with a total of 3 852 cells, subsequently increased to 16 480 cells. This is less than the number of cells in the reference model grid used in this study (18 375). The study by Choi and Fletcher (1997) employed a finite volume grid containing only 4 148 cells for a geometry of greater dimensions than the validation model. Hence, although no exhaustive study on the effect of grid cell size was carried out in this study, the values used compare favourably to those used in other studies.

Another factor is the type of turbulence model employed in the study. We used the realizable k-epsilon model proposed by Shih *et al.* (1995). This model was designed to address certain weaknesses in the standard k-epsilon turbulence model, and tests carried out by Fluent Inc. (2006a) showed that it performs substantially better than the standard model. It is possible that other turbulence models could provide better results in the simulations, for example the k-omega model. However, a study by Schmid (2003) showed that although turbulence has an effect on the ESP performance, the E-field is what dominates.

Finally, it should be mentioned that the boundary layer in the gas flow is not present at the inner wire surface. This was set accordingly in the model with the justification that in an axisymmetric geometry such as the one used in this study, the ratio of the surface area of the outer cylinder to the inner wire is 60, hence boundary layer effects at the wire were negligible.

4.2 The simulations

In this section, the results obtained from the models that were simulated in this study will be discussed, namely the validation model, the reference model and the prototype model.

4.2.1 Validation model

The objective of the validation model was to reproduce experimental collection efficiency results from a known set of conditions and ESP geometry. The main result from the validation model was the collection efficiency curve for a range of particle diameters (Figure 3.5). Over the particle diameter range from 0,1 to 0,19 μm, the simulation results show agreement with the experimental data to within 5%. Unfortunately, data was not available beyond a diameter of 0,19 μm.

As mentioned in the results section, several difficulties were encountered while trying to simulate the validation model. Firstly, the discrepancy between the theoretical V-I curves and those presented by Zhuang *et al.* could not be resolved without significant modification of the parameters. The theoretical curves can be made to match the data by changing the value of the ion mobility to 2,9 x 10^{-4} m^2/V/s, however there is no physical justification for such a change, moreover this value is well out of the range of values found in the literature (between to 1,6 x 10^{-4} and 2,2 x 10^{-4} m^2/V/s for negative ions). Fortunately, the difference between the measured and theoretical currents at low applied voltages is small, and the measured collection efficiency curve was obtained at a low applied voltage of -9 kV. The other discrepancy between the model and the experimental data was due to the number density of particles at the inlet. Zhuang *et al.* only mention this value once in their paper (a value of

10^{10} m^{-3}), in a manner that implies that this parameter was estimated. However, running the simulations using this value produced no effect on the total space charge distribution, which is inconsistent with their experimental results, as can be seen in the V-I curve in Figure 3.1. A value of 5 x 10^{13} m^{-3} was found to produce an effect of the desired magnitude, as hence was used for the simulations.

Despite these discrepancies, we can conclude that the validation model has demonstrated the ability of the simulation technique developed in this work to reproduce the experimental collection efficiency curve to within 5%.

4.2.2 Reference model

The reference model was produced and simulated in order to provide results for the collection efficiency of a simple wire-cylinder ESP scaled to the size of a residential flue pipe. Excepting the scale, major differences between the validation and reference models include the flue gas temperature, the inlet gas velocity profile and of course the physical properties of the PM and its size distribution.

The mass density of the PM produced by wood combustion was determined by Coudray *et al.* (2009) to be 2 000 kg/m^3, compared to 4 000 kg/m^3 for the alumina particles used in the validation model. Thus the combustion particles have half the mass of equivalent sized alumina particles, meaning that for a given force acting, the acceleration of combustion particles will be twice that for the alumina particles. Also, the dielectric constant of the combustion particles was estimated to be 2,4 as opposed to 9,34 for alumina. This has the effect of reducing the saturation charge on the particles by 34% (see equation 2.22). Since the electrostatic body force on the particle is directly proportional to its charge, the net effect of these two property changes should be a 34% increase in the electrostatic body force at saturation charge.

The overall collection efficiency of the reference model at an applied potential of +25 kV and for an average inlet gas velocity of 0,21 m/s was found to be 95%. No direct comparison of this result was possible due to a lack of studies with similar set-ups, however a study by Asbach *et al.* (2004) of a tubular two-stage ESP with positive wire potential used for ambient air particle filtering (particle diameters 0,3 – 13 μm) showed a collection efficiency of up to 96% for a low gas flow velocity (0,04 m/s). Hence, high collection efficiencies are possible for sub-micron sized particles, as long as the gas flow velocity remains low.

The most interesting result from the reference model is the overall collection efficiency curves as a function of applied voltage for three inlet gas flow velocities (Figure 3.13). Here we notice the large effect of the inlet gas velocity on the collection efficiency. The curves for the three values of inlet gas velocity are quite different in shape. At a low inlet gas flow velocity of 0,21 m/s on average, the efficiency curve is initially very steep as the applied voltage is increased, and soon reaches nearly 100%. In contrast, the curve for high inlet gas flow velocity of 0,84 m/s is nearly linear in shape, with efficiency increasing only slowly with applied voltage. This can be explained by the fact that particles in a fast-moving gas flow have less time to migrate to the collection surface, and also they may not become fully charged before they reach the exit, hence the body force acting on them will be lower. This result is confirmed by Skodras *et al.* (2006), who showed that a quadrupling of inlet gas velocity leads to a reduction in collection efficiency from 80% to 20% in a wire-plate ESP.

An ESP of similar scale to the reference model was built and tested experimentally by Schmatloch and Rauch (2005), and the results show an overall efficiency curve as a function of applied voltage that qualitatively matches the curve for an average inlet gas flow velocity of 0,42 m/s in Figure 3.13. An efficiency of approximately 75% was achieved for an electrode length of 0,2 m. However, since they do not provide a precise value for the inlet gas flow velocity or the particle number distribution at the inlet, it is not possible to compare the results quantitatively.

4.2.3 Prototype model

The prototype model was devised to test the collection efficiency of a multiple ESP tube configuration located inside a standard flue pipe. One advantage of such a device would be a much more compact size as compared to the reference model. The main disadvantages of the prototype model are that its overall collection efficiency is limited to 76% due to the gaps between the ESP tubes, as well as its rather complex design. These gaps could be filled of course, but this would lead to an increased gas flow velocity in each of the ESP tubes, resulting in reduced collection efficiency. It is also possible that under certain operating conditions (cold temperature starting), the ESP could restrict the chimney draft sufficiently to cause smoke back-draft into the room when the stove is located.

The graph of interest here is the total collection efficiency of the prototype device as a function of applied voltage (Figure 3.22). Initially the efficiency rises quite linearly with applied voltage, but beyond 10 kV the curve begins to flatten out towards the asymptotic value of 76%. Hence it is clear that the target efficiency of 75% is only attainable by such a device operating at very high voltages with corresponding high power consumption levels.

4.2.4 Model comparison

The reference and prototype model performance comparison in terms of estimated power consumption was presented in Figure 3.23. From this graph it is clear that the reference model out-performs the prototype model in terms of its collection efficiency for a given power consumption. It may be possible to improve the performance of the prototype by filling the gaps between the ESP tubes and increasing the applied voltage to overcome the significant decrease in efficiency that would arise from an increased gas flow velocity in the tubes. However, this would result in a significant increase in the power consumption of the device, which is already higher than the reference model. From this comparison we can conclude that the prototype model does not represent an improvement over the reference model, even prior to discussing the design considerations.

4.3 PM emissions reduction estimate

The results of this study can be used to produce an estimate of $PM_{2.5}$ emissions reduction that could theoretically result from the widespread use of a device such as the one described by the reference model (assuming that all the practical, safety and technical issued discussed in the previous section have been successfully resolved). This estimate is based on the $PM_{2.5}$ emissions data for residential fuel wood combustion in Quebec for 2007, as provided by Environment Canada (2009) and on the heating stock statistics for the same year provided by Natural Resources Canada (2010). We will assume that the device is installed in all of the residences that use wood as a primary heating fuel (112 000 units), and in 50% of the residences that use wood as a secondary heating fuel (467 000 units). Then assuming that secondary usage residences only use the woodstove for 10% of the heating season, whose duration is approximately 2 400 hours, we can attribute the $PM_{2.5}$ emissions to each sector according to its usage rate. Next, we assume an operating efficiency of 75%, which we have determined to be feasible from the results of the simulations. In such a scenario, total $PM_{2.5}$ emissions from residential fuel wood combustion in Quebec would be reduced from 47 437 tonnes (or 60% of the total $PM_{2.5}$ emissions, excluding open and natural sources) to 17 094 tonnes (or 38% of the total $PM_{2.5}$ emissions). This represents a reduction of 64%.

Whether or not such a target is attainable will depend on the affordability of the device. This, in turn, will depend on the willingness of government to tackle the problem of air pollution produced by woodstoves, possibly by providing a subsidy for the installation of the device, or funding R&D projects of this nature in the future. Considering the potential reduction in health problems (and therefore costs) associated with poor air quality that would result from using the device, it would appear to be in the interest of the government to pursue such projects.

4.4 Practical & design considerations

Numerical simulation studies such as this one are useful in testing many possible designs to determine the theoretical optimum design that satisfies given performance criteria. It must

always be remembered however that any such model must eventually be built and bench-tested before it can progress to the next development phase. Hence, practical and design considerations are very important and should not be ignored even at the simulation stage of product development. The main practical and design considerations for a small-scale ESP device can be listed as follows:

A. Performance;
B. Safety;
C. Durability & reliability;
D. Manufacture & installation;
E. Maintenance requirements;
F. Operating costs.

A serious issue that must be addressed is the rate of ozone production in the device. The use of a positive corona will minimise the production of ozone (compared to negative corona), however further experimental studies are required to determine the exact rates of production for such a device, and if necessary to devise a means to reduce the rate below acceptable standards.

Another important factor to consider is the power consumption of such a device. As we have seen, the reference model can operate at an efficiency of over 75% while consuming approximately 30 W (for a gas velocity at the inlet of 0,84 m/s). Assuming the device uses 100 W in total, including transformer losses and other electronic power requirements, at current electricity prices in Quebec, the annual bill for the device in the case of a residence that uses wood as its primary fuel source would be around $ 17.

CONCLUSION

In this study we have identified the widespread use of woodstoves for home heating as one of the major causes of urban and suburban air pollution during winter, leading to smog events. This pollution has also been identified as being a leading cause of adverse health effects, mainly affecting the respiratory system. This is a problem that is widespread in North America and northern Europe. After a review of the possible solutions to this problem, we focussed our attention on one particular particulate removal technology, namely electrostatic precipitation.

The potential collection efficiency of a small-scale ESP device suitable for installation in residential flue pipes was evaluated by means of a sophisticated numerical model and simulation. The numerical simulation technique used for this study was based on previous work by other researchers, but includes several enhancements that improved the accuracy of the simulation results.

After carrying out multiple simulations on various models, some general conclusions about the results can be made. First of all, the model was validated using experimental data, and the collection efficiency was found to correspond to within 5% over a range of particle sizes. The so-called penetration window in the sub-micron particle size range, where collection efficiency shows a minimum, was well reproduced by the simulations, especially for the validation model. The most important factors influencing the overall collection efficiency are the applied voltage and the inlet gas flow velocity. The overall collection efficiency was seen to increase rapidly at low applied voltages, and then more slowly at higher voltages. The collection efficiency was seen to be very sensitive to the value of the inlet gas flow velocity, which determines the amount of time the particles spend inside the ESP. Other factors which influence the results are the value of the turbulence intensity at the inlet, the ion mobility, gas temperature, the space charge distribution, as well as the particle properties. These factors are outside our direct control in real-life situations, however.

The results of simulations of a prototype model show that the model proposed is not a suitable candidate for a commercial device due to its lower cleaning efficiency and its more complex design that will lead to higher production and maintenance costs. The reference model, in contrast, is a very simple design that demonstrates an acceptable collection efficiency (75%) of sub-micron particles with low power consumption (30 W for an average gas velocity at the inlet of 0,84 m/s).

The results of this modeling study show that a technical solution to the problem of $PM_{2.5}$ emissions from wood burning stoves exists, and if the technical and operational issues can be successfully overcome, such a device could be launched commercially. The following hurdle will be to get the device installed in as many residences as possible in a timely manner. This will be directly determined by the cost of the device.

In one potential scenario explored, widespread use of the device in the province of Quebec, Canada during 2007 would have resulted in a reduction in $PM_{2.5}$ emissions from residential fuel wood combustion of 64%. The resulting reduction in health problems related to poor air quality would make the use of such a device worthwhile from a medical perspective, and could possibly pay for itself through reduced health costs into the future. Finally, the repercussions of this study can be stated as follows:

A. The creation of a sophisticated modeling scheme that can be applied to other geometries with little modification;
B. A theoretical proof of concept that a small-scale ESP device is capable of significantly reducing $PM_{2.5}$ emissions from residential wood fuel burning;
C. The identification of the major practical and technical issues that need to be addressed before this concept can progress to the next stage in development.

APPENDIX I

UDF MACRO SOURCE CODE

```
/*****************************************************************************
REFERENCE-MODEL-MASTER-00
Master UDF file containing all the macros for reference model
Ion mobility set as a global static variable, B_ION
UDS scalars used: 0-9
UDMs used: 23
*****************************************************************************/

#include "udf.h"

#define B_ION 1.5e-4    /* Ion mobility - positive ion estimate */
#define v_wire 25000.0  /* APPLIED VOLTAGE AT WIRE */
#define CURR  1.76e-4 /* CURRENT/UNIT LENGTH (Am-1) SRI 1.10  - NOT USED IN THIS VERSION!!! */
#define REL_PERM 2.4                    /* Estimated relative permittivity of wood combustion particles */
#define E_C 1.602177e-19                /* charge on electron */
#define EPS_0 8.85418717e-12
#define K 13.806505E-24      /* Boltzmann const */
#define DUST_CH_RATIO 2.0

static int flag=0;

/* UDS_E_09.c
contains 3 UDFs:
an on-demand UDF that reserves three UDSs and 1 particle variable and renames the UDMs
an on-demand UDF that sets the initial value of the UDMs,
a define adjust UDF to calculate E field components and magnitude
*/

DEFINE_EXECUTE_ON_LOADING(on_loading, libname)
{
  int i;
  Message("Setting names for %s...\n",libname);

  Set_User_Memory_Name(0,"E-field");
  Set_User_Memory_Name(19,"P-mass-conc");
  Set_User_Memory_Name(13,"P-num-conc");
  Set_User_Memory_Name(1,"Phi-source");
  Set_User_Memory_Name(2,"Rho-source");
  Set_User_Memory_Name(8,"X-mom-source");
  Set_User_Memory_Name(9,"Y-mom-source");
  Set_User_Memory_Name(10,"E-y-SRI");
  Set_User_Memory_Name(22,"d-rho-particle");

  Set_User_Scalar_Name(0,"Phi");
  Set_User_Scalar_Name(1,"Rho-ion");
  Set_User_Scalar_Name(2,"E_x");
  Set_User_Scalar_Name(3,"E_y");
  Set_User_Scalar_Name(4,"Rho-p");
  Set_User_Scalar_Name(5,"Rho-total");
  Set_User_Scalar_Name(6,"V-cell-x");
  Set_User_Scalar_Name(7,"V-cell-y");
  Set_User_Scalar_Name(8,"j-total-x");
  Set_User_Scalar_Name(9,"j-total-y");



  for (i=0;i<=9;i++)
  {
                  Message("Set User scalar name: %d\n",i);
  }

  Message("Done!\n");
}


/* Sets the gradient of phi (UDS-0) to equal E_x (UDS-2) and E_y (UDS-3), and sets face values */

DEFINE_ADJUST(Calc_E_xy,d)
{
  Thread *t;
  cell_t c;
  face_t f;
  Thread *t0;
  cell_t  c0;
  real dr0[ND_ND],dr1[ND_ND], xf[ND_ND], dy;
  real ratio=1.0; /* correction to E(face) calc to match with theory */

  /* Do nothing if gradient isn't allocated yet. */
  if (!Data_Valid_P()) return;


  thread_loop_c(t,d)
                {

    if (NULL != THREAD_STORAGE(t,SV_UDS_I(0)) &&
        NULL != T_STORAGE_R_NV(t,SV_UDSI_G(0)))

                {
                        begin_c_loop(c,t)
                        {
                          C_UDSI(c,t,2) = -1.*C_UDSI_G(c,t,0)[0];
```

```
                C_UDSI(c,t,3) = -1.*C_UDSI_G(c,t,0)[1];
                C_UDMI(c,t,0) = NV_MAG(C_UDSI_G(c,t,0));
              }
              end_c_loop(c,t)
        }
  }

 thread_loop_f(t,d)
  {
   if (NULL != THREAD_STORAGE(t,SV_UDS_I(3)) &&
       NULL != T_STORAGE_R_NV(t->t0,SV_UDSI_G(3)))

        {
              if (BOUNDARY_FACE_THREAD_P(t)) /*extrapolate E-face at boundaries only */
              {
                    /* Message("Boundary Thread no. %d..\n", THREAD_ID(t));                    */
                    begin_f_loop(f,t)
                          {
                                c0 = F_C0(f,t);
                                t0 = THREAD_T0(t);
                                F_CENTROID(xf,f,t);
                                C_CENTROID(dr0,c0,t0);
                                NV_VV(dr1,=,xf,-,dr0);
                                F_UDSI(f,t,2) = C_UDSI(c0,t0,2) + (C_UDSI_G(c0,t0,2)[0]*dr1[0]);
                                F_UDSI(f,t,3) = C_UDSI(c0,t0,3) + (ratio*C_UDSI_G(c0,t0,3)[1]*dr1[1]);
                          }
                    end_f_loop(f,t)
                    }
        }
  }
}
```

```
/************************************************************************/
/* UDF_source_phi_rho_11.c  for specifying the phi and rho source terms for uds-0      */
/************************************************************************/

DEFINE_SOURCE(phi_source,c,t,dS,eqn)
{
        real phi_source;
        dS[eqn] = 0.0;

        phi_source = (C_UDSI(c,t,1)+C_UDSI(c,t,4))/EPS_0;
        C_UDMI(c,t,1) = phi_source;

        return phi_source;
}

DEFINE_SOURCE(rho_source,c,t,dS,eqn)
{
        real rho_source;
        real xc[ND_ND];
        real dens;
        dS[eqn] = 0.0;

        C_CENTROID(xc,c,t);
        dens=C_R(c,t);
        rho_source = C_UDSI(c,t,9)/xc[1] + C_UDSI_G(c,t,9)[1] + C_UDSI_G(c,t,8)[0];
        rho_source = -dens*rho_source;
        C_UDMI(c,t,2) = rho_source; /* rho source */

        return rho_source;
}

/************************************************************************
 UDF_mom_source_01.c for specifying the gas momentum source terms (rho * E)
************************************************************************/

DEFINE_SOURCE(x_mom_source,c,t,dS,eqn)
{
        real x_m_source;
        dS[eqn] = 0.0;

        /* Do nothing if data not valid yet. */
        if (Data_Valid_P())
        {
                x_m_source = C_UDSI(c,t,1)*C_UDSI(c,t,2);
                C_UDMI(c,t,8) = x_m_source; /* store to memory 8 */
                return x_m_source;
        }
        else
        {
                x_m_source = 0.0;
                return x_m_source;
        }
}

DEFINE_SOURCE(y_mom_source,c,t,dS,eqn)
{
        real y_m_source;
        dS[eqn] = 0.0;

        /* Do nothing if data not valid yet. */
        if (Data_Valid_P())
        {
                y_m_source = C_UDSI(c,t,1)*C_UDSI(c,t,3);
                C_UDMI(c,t,9) = y_m_source; /* store to memory 9 */
                return y_m_source;
        }
        else
        {
                y_m_source = 0.0;
                return y_m_source;
        }
}
```

```
/*************************************************************************
  UDF_DPM_charge_11C.c
  UDF for computing the charge acquired (qmax) along a particle trajectory
  Uses an Improved Euler method (2nd order Runge-Kutta)
  Based on Sum of Charges model F(v,w) + D(v) from Lawless (1997)

  UDF for calculating the particle space charge rho-p and store to UDS-4
*************************************************************************/

DEFINE_INIT(particle_setup,domain)
{
      /* if memory for the particle variable titles has not been
       * allocated yet, do it now */

  if (NULLP(user_particle_vars)) Init_User_Particle_Vars();

       /* now set the name and label */

  strcpy(user_particle_vars[0].name,"particle-charge");
  strcpy(user_particle_vars[0].label,"Particle charge");
  strcpy(user_particle_vars[1].name,"total-charges");
  strcpy(user_particle_vars[1].label,"Total charges");
  strcpy(user_particle_vars[2].name,"diff-charge-n");
  strcpy(user_particle_vars[2].label,"Diffusion charges");
  strcpy(user_particle_vars[3].name,"field-charge-n");
  strcpy(user_particle_vars[3].label,"Field charges");
  strcpy(user_particle_vars[4].name,"Particle-BForce");
  strcpy(user_particle_vars[4].label,"Particle Body Force");
  strcpy(user_particle_vars[5].name,"Particle-acc");
  strcpy(user_particle_vars[5].label,"Particle acceleration");

  Message("Initializing Particle memory...\n");
}

/* Set particle velocity and temp equal to flow field at inlet */

DEFINE_DPM_INJECTION_INIT(Init_V_T,I)
{
 Particle *p;
 cell_t cell;
 Thread *cthread;

 /*Message("Initializing Injection: %s\n",I->name); */

 loop(p,I->p)  /* Standard Fluent Looping Macro to get particle
                  streams in an Injection */
 {
  cell = P_CELL(p);   /* Get the cell and thread that the particle
                         is currently in    */
  cthread = P_CELL_THREAD(p);

  P_T(p)=C_T(cell,cthread); /* temperature */

  P_VEL(p)[0]=C_U(cell,cthread); /* x velocity */
  P_VEL(p)[1]=C_V(cell,cthread);  /* y velocity */
  P_VEL(p)[2]=C_W(cell,cthread);  /* z velocity */
 }
}

/* Calculate particle charge as it moves thru ESP, accumulate Eulerian p-charge values */

DEFINE_DPM_SCALAR_UPDATE(particle_charge,cell,thread,initialize,p)
{
  real E_y, diam, p_charge, rho_ion;
  real nc, n_tot,delta_nc;


  /* declare dimensionless variables */

  real w,m,er_f;

  /* declare intergration variables (also dimless) */

  real k1, k2, delt, M_1,M_2;

  real polarity=1;
  static real vc=1e-6;  /* dimless combined charge is non-zero */


  /* set field charge factor */

  er_f=3*REL_PERM/(REL_PERM+2);



  if (initialize)
    {
     /* this is the initialization call, set: initial charge on particle is small */
     P_USER_REAL(p,0) = 0.;
                  vc=1e-6;
```

```
		}
 else
  {
		/* Get solver values */
			E_y = C_UDSI(cell, thread, 3);
			if (E_y < 0)  polarity = -1.; /* set charge polarity */
			rho_ion = fabs(C_UDSI(cell, thread,1));
			diam = P_DIAM(p);

			/* convert w and t to dimless variables */

			w=abs(E_y)*diam*E_C/(2*K*P_T(p));
			m=er_f*w;
			delt = B_ION*rho_ion*P_DT(p)/EPS_0; /* time step */

			/* Apply Euler algorithms for diffusion & field charging */

			if (vc<=m)
			{
				M_1=(m/4*pow(1-vc/m,2))+(vc)/(exp(vc)-1);
				k1=delt/2*M_1;
				M_2=(m/4*pow(1-(vc+k1)/m,2))+(vc+k1)/(exp(vc+k1)-1);
				k2 = delt*M_2;
				vc+=k2;
			}
			else if (vc>m)
			{
				M_1=(vc)/(exp(vc)-1);
				k1=delt/2*M_1;
				M_2=(vc+k1)/(exp(vc+k1)-1);
				k2 = delt*M_2;
				vc+=k2;
			}


			/* convert charges to number of elementary charges */

			nc=2*M_PI*EPS_0*diam*K*P_T(p)*vc/pow(E_C,2);
			delta_nc= 2*M_PI*EPS_0*diam*K*P_T(p)*k2/pow(E_C,2);

			/* calc sum F+D : if diff or field component less than 1 then set to zero */
			if (nc<1) nc=0;

			n_tot=floor(nc);
			P_USER_REAL(p,1) = n_tot;

			/* return particle charge */

			p_charge = polarity*n_tot*E_C; /* particle charge will be NEGATIVE for -ve E */
			P_USER_REAL(p,0) = p_charge;
			P_USER_REAL(p,2) = polarity*delta_nc*E_C;


  }
}

DEFINE_DPM_SOURCE(q_source,c,t,S,strength,p)
{
 real charge,d_charge,delta_qp;
 real t_res, qp;
 real v_cell_x,v_cell_y,dx,dy;
 real mfr,nfr;

 /* charge is the accumulated charge due to the particles in each cell */


 qp=P_USER_REAL(p,0);
 delta_qp=P_USER_REAL(p,2);

 t_res=P_TIME(p)-P_TIME0(p); /* particle residence time */
 dx=P_VEL(p)[0]*t_res;
 dy=P_VEL(p)[1]*t_res;
 nfr=strength*t_res;
 charge=qp*nfr;
 d_charge=delta_qp*nfr*(t_res/P_DT(p));
 mfr=P_MASS(p)*nfr;
 v_cell_x=P_MASS(p)*strength*dx;
 v_cell_y=P_MASS(p)*strength*dy;

 C_UDMI(c,t,11) += charge;
 C_UDMI(c,t,12) += nfr;
 C_UDMI(c,t,18) += mfr;
 C_UDMI(c,t,14)+= v_cell_x;
 C_UDMI(c,t,15)+= v_cell_y;
 C_UDMI(c,t,21)+= d_charge;


 flag=1; /* set flag to 1 */

}
```

```
DEFINE_ADJUST(rho_particle,d)
{
  Thread *t;
  cell_t c;
  face_t f;
  Thread *t0;
  cell_t  c0;
  real dr0[ND_ND],dr1[ND_ND], xf[ND_ND], dy;

  real j_ion,j_load,d_ratio,E_y;

  if (!Data_Valid_P()) return;


  thread_loop_c(t,d)
                {

    if (NULL != THREAD_STORAGE(t,SV_UDS_I(4)))

                {
                                begin_c_loop(c,t)
                                {
                                  if (flag==1)
                                  {
                                                C_UDSI(c,t,4) = C_UDMI(c,t,11)/(C_VOLUME(c,t)); /* rho-particle */
                                                C_UDMI(c,t,22) = C_UDMI(c,t,21)/(C_VOLUME(c,t)); /* delta-rho-particle */
                                                C_UDMI(c,t,13) = C_UDMI(c,t,12)/(C_VOLUME(c,t));/* number conc */
                                                C_UDMI(c,t,19) = C_UDMI(c,t,18)/(C_VOLUME(c,t));/* mass-conc */
                                                if (C_UDMI(c,t,18)==0.)
                                                {
                                                                C_UDSI(c,t,6) = 0.0;
                                                                C_UDSI(c,t,7) = 0.0;
                                                }
                                                else
                                                {
                                                                C_UDSI(c,t,6) = C_UDMI(c,t,14)/C_UDMI(c,t,18); /* V-cell-x */
                                                                C_UDSI(c,t,7) = C_UDMI(c,t,15)/C_UDMI(c,t,18); /* V-cell-y */
                                                }

                                                C_UDMI(c,t,11) = 0.0;
                                                C_UDMI(c,t,12) = 0.0;
                                                C_UDMI(c,t,14) = 0.0;
                                                C_UDMI(c,t,15) = 0.0;
                                                C_UDMI(c,t,18) = 0.0;
                                                C_UDMI(c,t,21) = 0.0;


                                  }

                                  C_UDSI(c,t,5) = C_UDSI(c,t,4)+C_UDSI(c,t,1); /* rho-total */

                                  /* j-total components */
                                  C_UDSI(c,t,8) = B_ION*C_UDSI(c,t,1)*abs(C_UDSI(c,t,2))+abs(C_UDSI(c,t,4))*C_UDSI(c,t,6);
                                  C_UDSI(c,t,9) = B_ION*C_UDSI(c,t,1)*abs(C_UDSI(c,t,3))+abs(C_UDSI(c,t,4))*C_UDSI(c,t,7);




                                }
                                end_c_loop(c,t)
                }
  }
  flag=0;

  thread_loop_f(t,d)
   {
    if (NULL != THREAD_STORAGE(t,SV_UDS_I(9)) &&
        NULL != T_STORAGE_R_NV(t->t0,SV_UDSI_G(9)))

                {
                                if (BOUNDARY_FACE_THREAD_P(t)) /*extrapolate  at boundaries only */
                                {
                                                begin_f_loop(f,t)
                                                                {
                                                                                c0 = F_C0(f,t);
                                                                                t0 = THREAD_T0(t);
                                                                                F_CENTROID(xf,f,t);
                                                                                C_CENTROID(dr0,c0,t0);
                                                                                NV_VV(dr1,=,xf,-,dr0);
                                                                                F_UDSI(f,t,8) = C_UDSI(c0,t0,8) + C_UDSI_G(c0,t0,8)[0]*dr1[0];
                                                                                F_UDSI(f,t,9) = C_UDSI(c0,t0,9) + C_UDSI_G(c0,t0,9)[1]*dr1[1];
                                                                }
                                                end_f_loop(f,t)
                                                }
                }
   }

}
```

```
/* P_body_force_2009_01.c
   UDF for computing the force on a charged particle due to E-field
   Uses UDS variables UDS-2 3 = E_x, E_y, P_USER_REAL(0) = particle charge along track
   Electric force is particle charge times E-field: Fx=q*Ex, Fy=q*Ey */

DEFINE_DPM_BODY_FORCE(body_force,p,i)
{
        real bforce, Ey, Ex, p_charge;
    Thread *t;
    cell_t c;

/* get current cell and thread pointer */
        c = P_CELL(p);
        t = P_CELL_THREAD(p);

/* get particle charge */
        p_charge = P_USER_REAL(p,0);

/* calculate body force */

        if (i==0) /* x component */
        {
                Ex = C_UDSI(c,t,2);
                bforce = Ex*p_charge;
        }
        else if (i==1)  /* y component */
        {
                Ey = C_UDSI(c,t,3);
                bforce = Ey*p_charge;
                P_USER_REAL(p,4)=bforce;
                P_USER_REAL(p,5)=bforce/P_MASS(p);
        }

/* an acceleration should be returned */
        return(bforce/P_MASS(p));
}
```

APPENDIX II

EXAMPLE EXCEL MACRO FOR DATA IMPORT

```
Sub Fluent_import()
'
' Fluent_import Macro
'
    Workbooks.OpenText Filename:= _
        "D:\Fluent data\fluent\2010\Reference\REF_37.txt", Origin:=xlMSDOS, _
        StartRow:=1, DataType:=xlDelimited, TextQualifier:=xlDoubleQuote, _
        ConsecutiveDelimiter:=False, Tab:=False, Semicolon:=False, Comma:=True _
        , Space:=False, Other:=True, OtherChar:="=", FieldInfo:=Array(Array(1, 9 _
        ), Array(2, 1), Array(3, 9), Array(4, 1), Array(5, 9), Array(6, 9), Array(7, 9), Array(8, 1), _
        Array(9, 9), Array(10, 9), Array(11, 9)), TrailingMinusNumbers:=True
    Range("1:21,23:25,27:29,31:33,35:37").Select
    Selection.Delete Shift:=xlUp
    Range("6:29,31:33,35:37,39:41,43:45").Select
    Selection.Delete Shift:=xlUp
    Range("11:34,36:38,40:42,44:46,48:50").Select
    Selection.Delete Shift:=xlUp
    Range("16:39,41:43,45:47,49:51,53:55").Select
    Selection.Delete Shift:=xlUp
    Range("21:44,46:48,50:52,54:56,58:60").Select
    Selection.Delete Shift:=xlUp
    Range("26:49,51:53,55:57,59:61,63:65").Select
    Selection.Delete Shift:=xlUp
    Range("31:54,56:58,60:62,64:66,68:70").Select
    Selection.Delete Shift:=xlUp
    Range("36:59,61:63,65:67,69:71,73:75").Select
    Selection.Delete Shift:=xlUp
    Range("41:62,64:66,68:70,72:74,76:78").Select
    Selection.Delete Shift:=xlUp
    Range("46:69,71:73,75:77,79:81,83:85").Select
    Selection.Delete Shift:=xlUp
    Range("51:74,76:78,80:82,84:86,88:90").Select
    Selection.Delete Shift:=xlUp
    Range("56:79,81:83,85:87,89:91,93:95").Select
    Selection.Delete Shift:=xlUp
    Range("61:82,84:86,88:90,92:94,96:98").Select
    Selection.Delete Shift:=xlUp
    Range("66:89,91:93,95:97,99:101,103:105").Select
    Selection.Delete Shift:=xlUp
    Range("71:94,96:98,100:102,104:106,108:110").Select
    Selection.Delete Shift:=xlUp
    Range("76:99,101:103,105:107,109:111,113:115").Select
    Selection.Delete Shift:=xlUp
    Range("81:104,106:108,110:112,114:116,118:120").Select
    Selection.Delete Shift:=xlUp
    Range("F1").Select
    ActiveCell.FormulaR1C1 = "=1-(AVERAGE(RC[-4]:R[4]C[-4])/R[0]C[-5])"
    Range("F2").Select
    ActiveCell.FormulaR1C1 = "=1-(AVERAGE(R[4]C[-4]:R[8]C[-4])/R[4]C[-5])"
    Range("F3").Select
    ActiveCell.FormulaR1C1 = "=1-(AVERAGE(R[8]C[-4]:R[12]C[-4])/R[8]C[-5])"
    Range("F4").Select
    ActiveCell.FormulaR1C1 = "=1-(AVERAGE(R[12]C[-4]:R[16]C[-4])/R[12]C[-5])"
    Range("F5").Select
    ActiveCell.FormulaR1C1 = "=1-(AVERAGE(R[16]C[-4]:R[20]C[-4])/R[16]C[-5])"
    Range("F6").Select
    ActiveCell.FormulaR1C1 = "=1-(AVERAGE(R[20]C[-4]:R[24]C[-4])/R[20]C[-5])"
    Range("F7").Select
    ActiveCell.FormulaR1C1 = "=1-(AVERAGE(R[24]C[-4]:R[28]C[-4])/R[24]C[-5])"
    Range("F8").Select
    ActiveCell.FormulaR1C1 = "=1-(AVERAGE(R[28]C[-4]:R[32]C[-4])/R[28]C[-5])"
    Range("F9").Select
    ActiveCell.FormulaR1C1 = "=1-(AVERAGE(R[32]C[-4]:R[36]C[-4])/R[32]C[-5])"
    Range("F10").Select
    ActiveCell.FormulaR1C1 = "=1-(AVERAGE(R[36]C[-4]:R[40]C[-4])/R[36]C[-5])"
    Range("F11").Select
    ActiveCell.FormulaR1C1 = "=1-(AVERAGE(R[40]C[-4]:R[44]C[-4])/R[40]C[-5])"
    Range("F12").Select
    ActiveCell.FormulaR1C1 = "=1-(AVERAGE(R[44]C[-4]:R[48]C[-4])/R[44]C[-5])"
    Range("F13").Select
    ActiveCell.FormulaR1C1 = "=1-(AVERAGE(R[48]C[-4]:R[52]C[-4])/R[48]C[-5])"
    Range("F14").Select
    ActiveCell.FormulaR1C1 = "=1-(AVERAGE(R[52]C[-4]:R[56]C[-4])/R[52]C[-5])"
    Range("F15").Select
    ActiveCell.FormulaR1C1 = "=1-(AVERAGE(R[56]C[-4]:R[60]C[-4])/R[56]C[-5])"
    Range("F16").Select
    ActiveCell.FormulaR1C1 = "=1-(AVERAGE(R[60]C[-4]:R[64]C[-4])/R[60]C[-5])"
    Range("F17").Select
```

```
    ActiveCell.FormulaR1C1 = "=1-(AVERAGE(R[64]C[-4]:R[68]C[-4])/R[64]C[-5])"
    Range("F1:F17").Select
    Selection.Copy
    Windows("fluent_data_REF_NEW.xlsm").Activate
    Sheets("MASTER").Select
    Range("w6").Select
    Selection.PasteSpecial Paste:=xlPasteValues, Operation:=xlNone, SkipBlanks _
        :=False, Transpose:=False
    Application.CutCopyMode = False
    Selection.NumberFormat = "0.00"
    Selection.Style = "Percent"
    Windows("REF_37.txt").Activate
    ActiveWorkbook.SaveAs Filename:= _
        "D:\Fluent data\fluent\2010\Reference\REF_37.xlsx", FileFormat:= _
        xlOpenXMLWorkbook, CreateBackup:=False
    Windows("fluent_data_REF_NEW.xlsm").Activate

End Sub
```

APPENDIX III

GAS FLOW VELOCITY PROFILE IN A FLUE PIPE

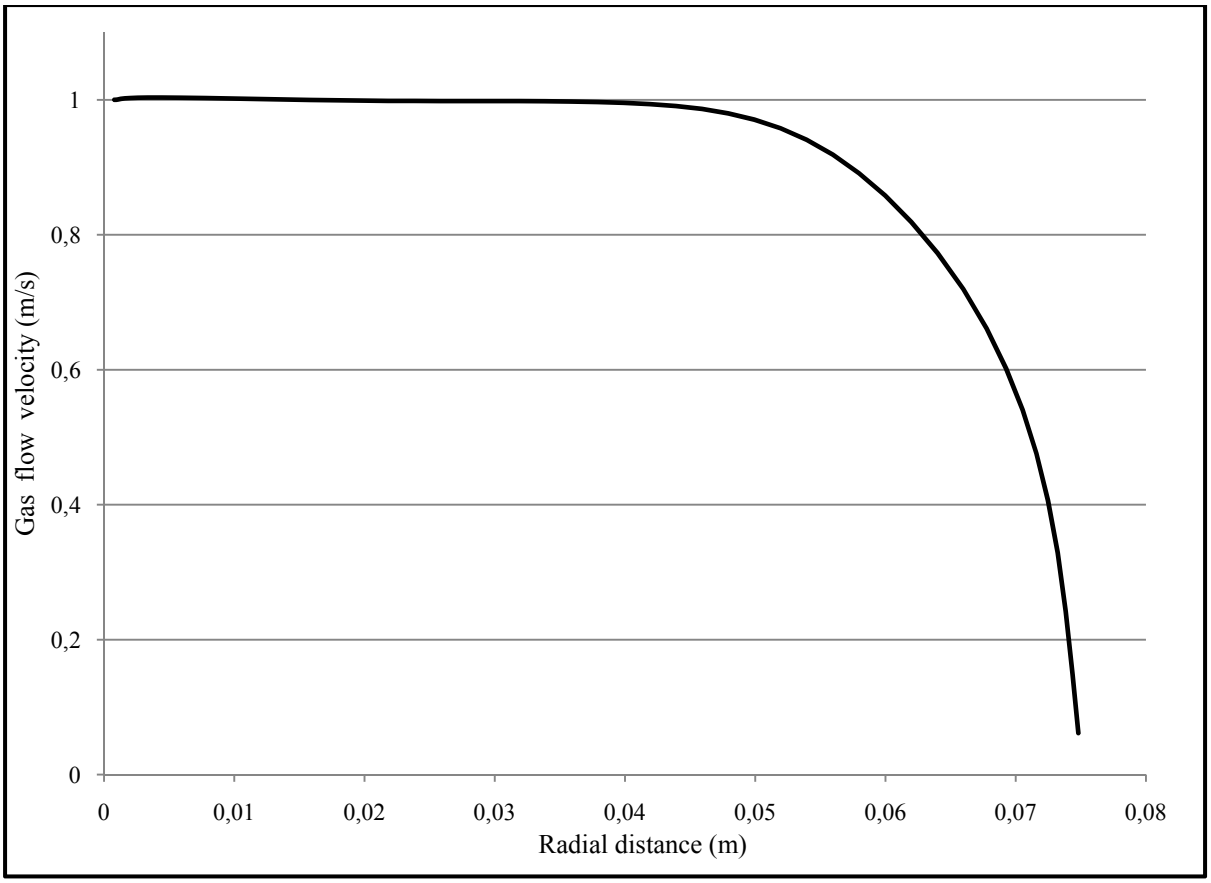

Figure-A III-1 Graph showing the variation of gas flow velocity with radial distance from the center of a flue pipe of radius 0,075 m after a distance of 8 m.

APPENDIX IV

PARTICLE SIZE DISTRIBUTION GRAPHS

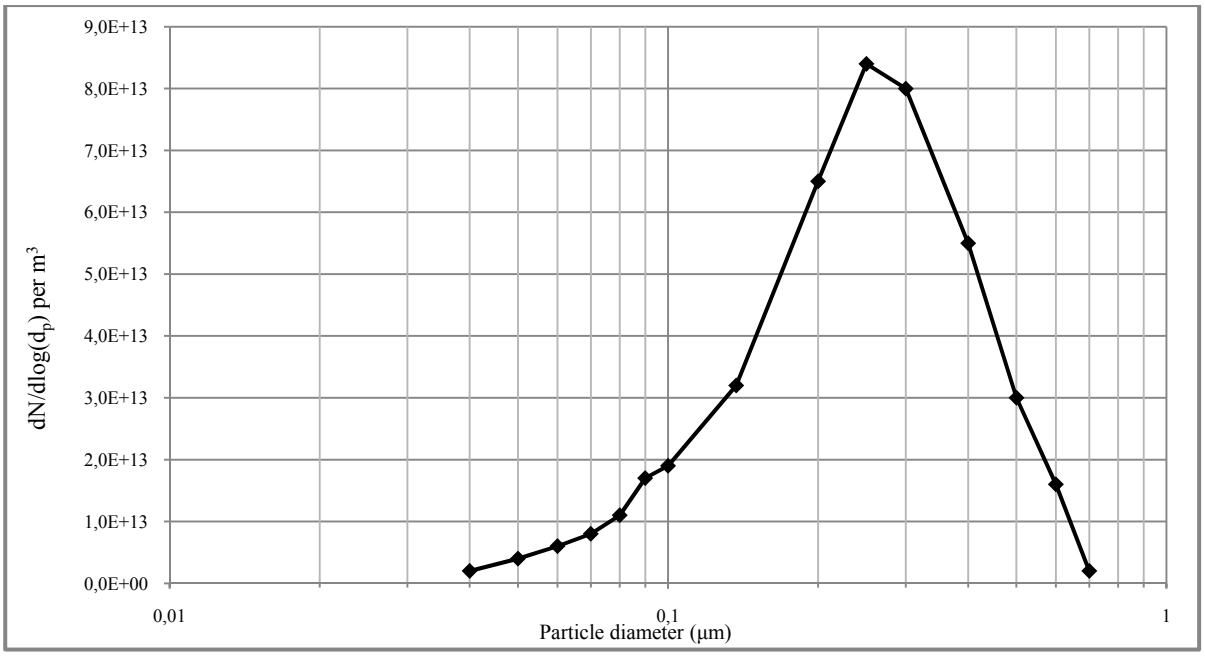

Figure-A IV-1 Experimental particle size distribution as measured during the start-up phase of a woodstove burning cycle, reproduced from data by Hueglin (1997).

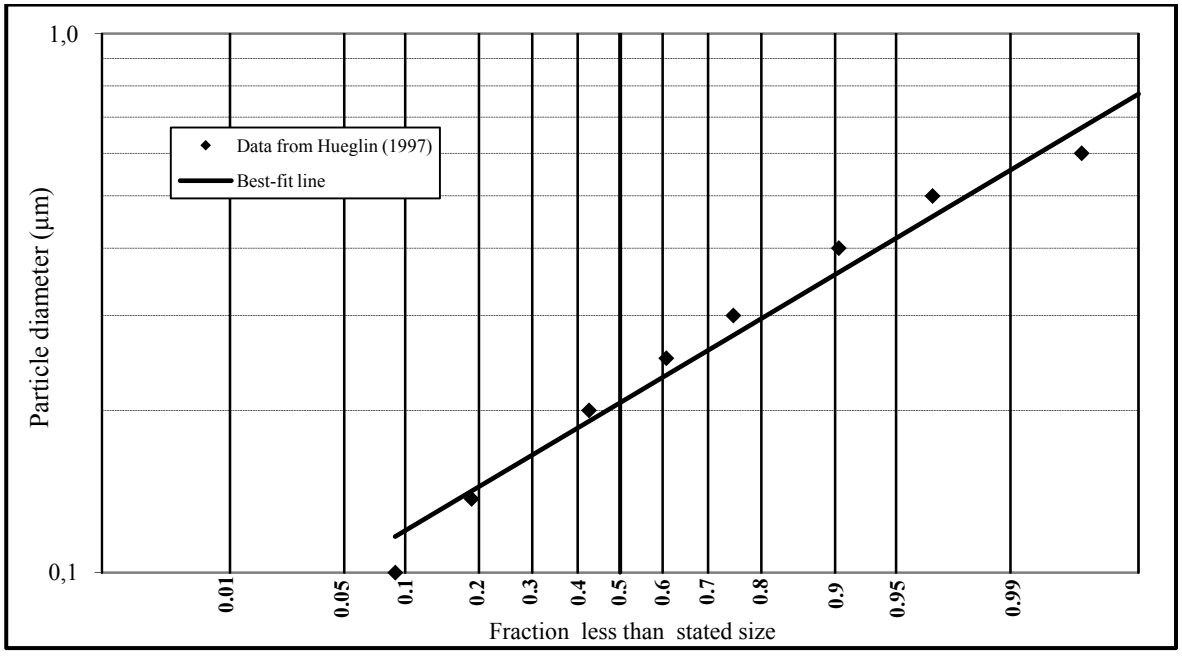

Figure-A IV-2 Log-probability plot of the above size distribution, along with a best-fit theoretical line (CMD = 0,217 µm, σ_g = 1,49).

APPENDIX V

CONTOUR PLOTS FOR THE PROTOTYPE MODEL, U_{INLET} = 0,77 m/s

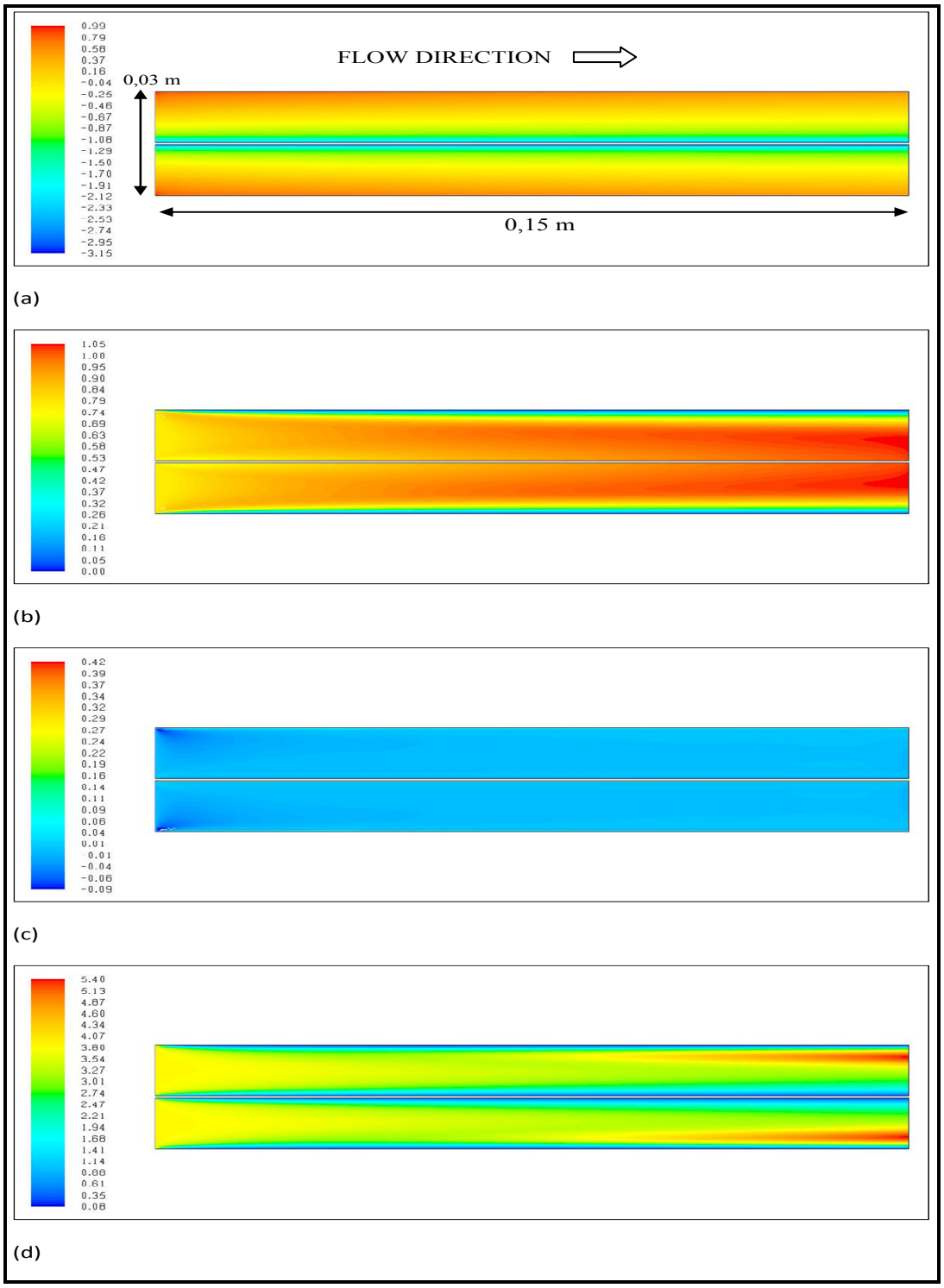

Figure-A V-1 Gas flow variables for the prototype model simulation with a gas flow velocity of 0,77 m/s at the inlet: (a) Static pressure field (Pa), (b) Axial gas velocity (m/s), (c) Radial gas velocity (m/s), (d) Turbulence intensity (%).

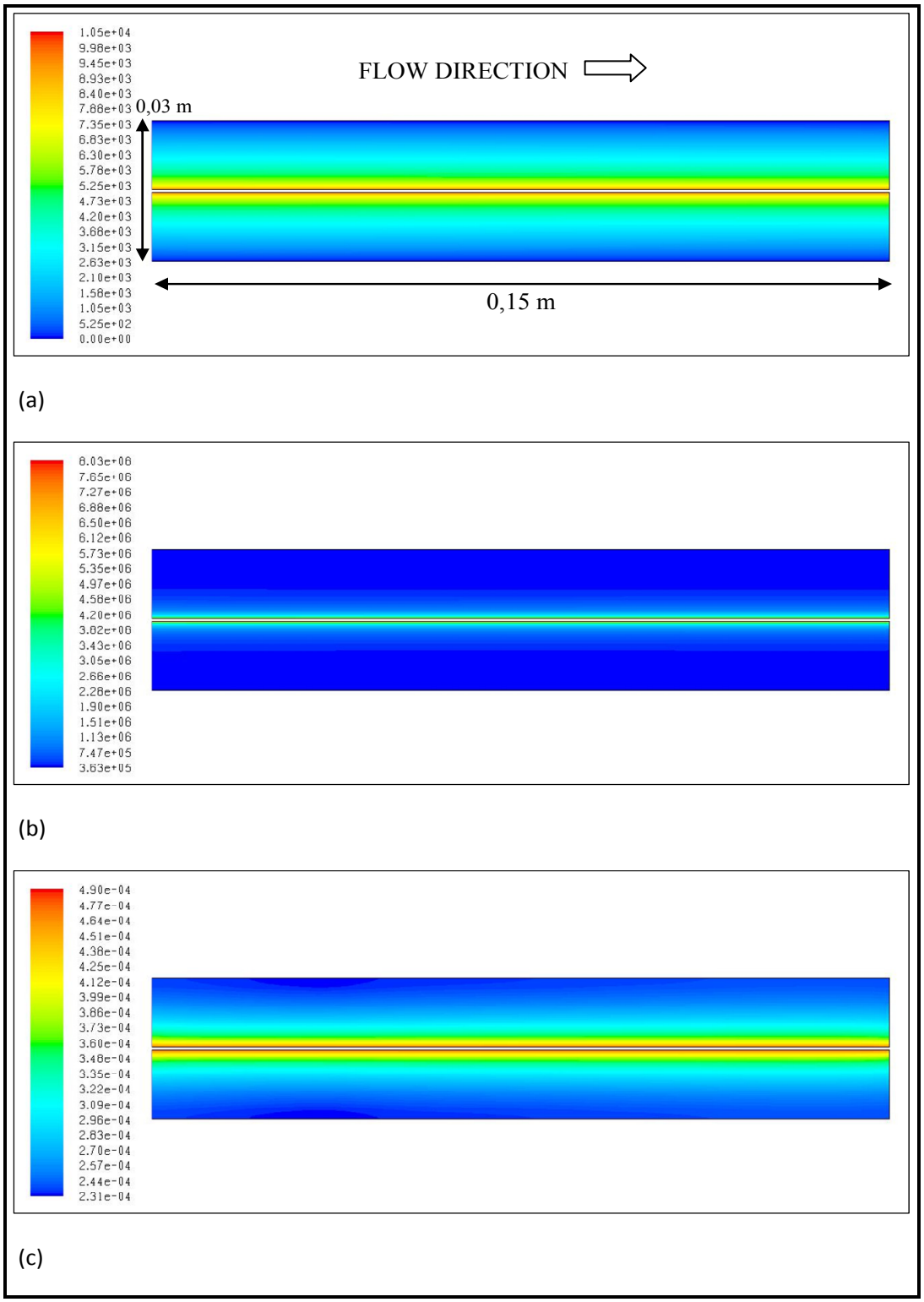

Figure-A V-2 Electrostatic variables for the prototype model simulation with an inlet gas flow velocity of 0,77 m/s : (a) Electric potential (V), (b) Electric field strength (V/m), (c) Ion charge density (C/m^3).

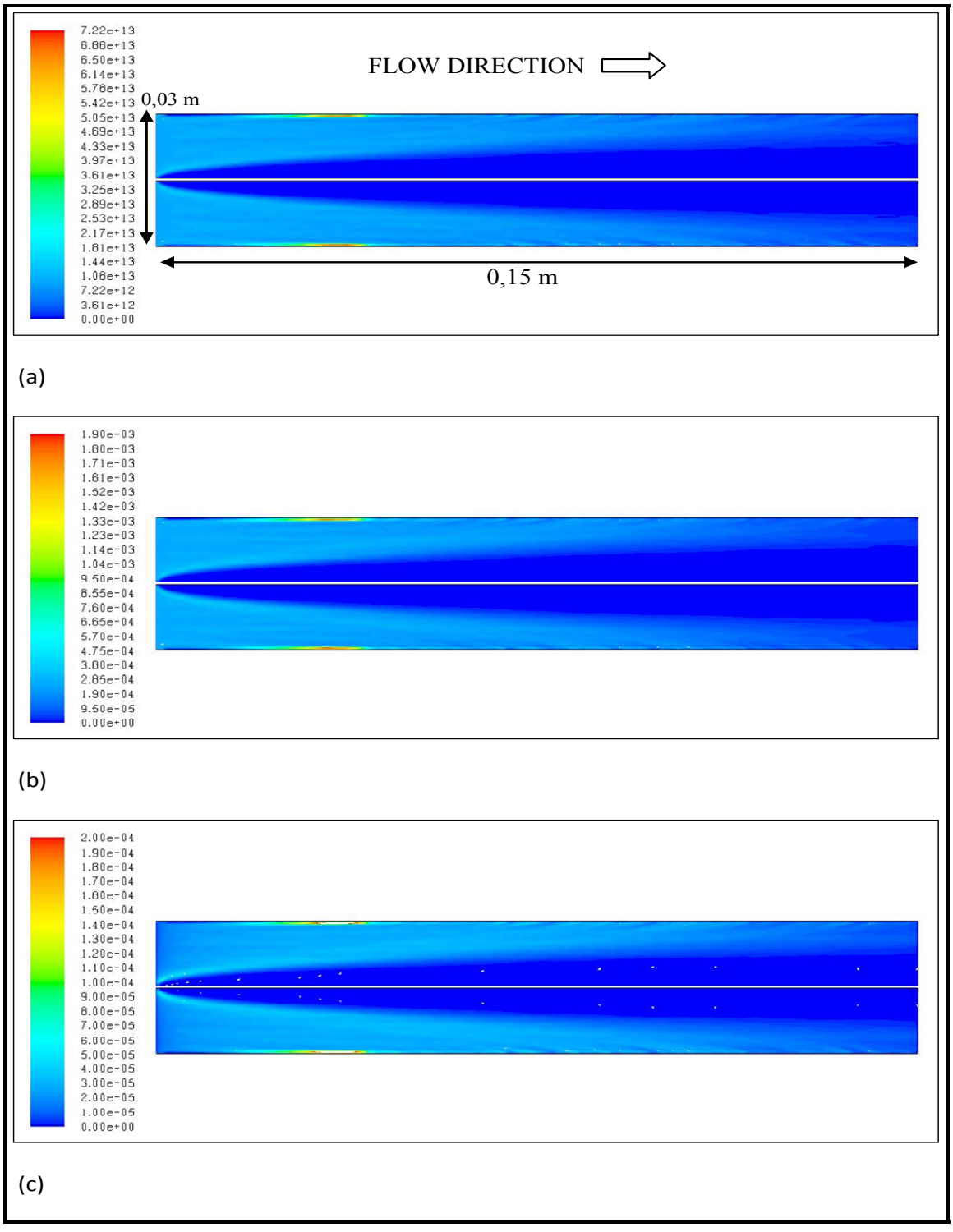

Figure-A V-1 Particle Eulerian variables for the prototype model simulation with an inlet gas flow velocity of 0,77 m/s : (a) particle number concentration (m^{-3}), (b) particle mass concentration (kg/m^3), (c) particle charge density (C/m^3).

REFERENCES

Asbach, C., T. A. J. Kuhlbusch and H. Fissan. 2004. "Development of an electrostatic partitioner for highly efficient partitioning of gas and particles with minimal effect on the gas phase". *Aerosol Science and Technology,* vol. 38, n° 4, p. 322-329.

Bernstein, S. and C. T. Crowe. 1981. "Interaction between electrostatics and fluid dynamics in electrostatic precipitators." *Environment International*, vol. 6, n° 1-6, p. 181-189.

Borman, G. and K.Ragland. 1998. *Combustion Engineering*. USA : McGraw-Hill, 613 p.

Canada Mortgage and Housing Corporation. 2008. *A Guide to Residential Wood Heating*. Ottawa : CMHC. 86 p.

Canadian Council of Ministers of the Environment. 2006. *Canada-wide Standards for Particulate Matter and Ozone: Five Year Report: 2000-2005*.

City of Montreal. 2009. By-law 09-012, *The Gazette*, Montreal, published on April 29, 2009.

Choi, B. S. and C. A. J. Fletcher. 1997. "Computation of particle transport in an electrostatic precipitator". *Journal of Electrostatics,* vol. 40-41, p. 413-418.

Cobine, J. D. 1978. *Gaseous Conductors. Theory and Engineering Applications*. New York : McGraw-Hill, 606 p.

Coudray, N., A. Dieterlen, E. Roth and G. Trouvé. 2009. "Density measurement of fine aerosol fractions from wood combustion sources using ELPI distributions and image processing techniques". *Fuel,* vol. 88, n° 5, p. 947-954.

Davis, D. L., M. L. Bell, and T. Fletcher. 2002. "A Look Back at the London Smog of 1952 and the Half Century Since". *Environmental Health Perspectives*, vol. 110, n° 12, p. A734.

Duffin, W. J. 1990. *Electricity and Magnetism*, 4th ed. London : McGraw-Hill, 437 p.

Environment Canada. 2004. *Residential Wood Heating - summary of results from 1999 to 2002*. Montreal : Public Works and Government Services Canada.

Environment Canada. 2009. *National Pollutant Release Inventory : CAC emissions summaries for 2007.* Ottawa.

Fairley, D. 1990. "The relationship of daily mortality to suspended particulates in Santa Clara County, 1980-1986.". *Environ. Health. Perspect.,* vol. 89, p. 159-168.

Fjeld, R. A., R. O. Gauntt and A. R. McFarland. 1983. "Continuum field-diffusion theory for bipolar charging of aerosols". *Journal of Aerosol Science,* vol. 14, n° 4, p. 541-556.

Fluent. 2006a. *FLUENT*, version. 6.3.26. Laboratory software. Fluent Inc.

Fluent. 2006b. *GAMBIT*, version. 2.4.6. Laboratory software. Fluent Inc.

Fuchs, N.A. 1947. "The Charges on the Particles of Aerocolloids". *Izv. Akad.Nauk. SSSR, Ser. Geogr. Geofiz.,* vol. 11, p. 34.

Government of Quebec. 2009. Law # L.R.Q., c. Q-2, a. 31, 1er al., par. a, c, d, e, h, i, a. 109.1, a. 124.0.1 et a. 124.1. *The Official Gazette.*

Hatch, T. and S. P. Choate. 1929. "Statistical Description of the Size Properties of Non-Uniform Particulate Substances". *J. Franklin Inst.,* vol. 207, p. 369.

Hedberg, E., A. Kristensson, M. Ohlsson, C. Johansson, P. Johansson, E. Swietlicki, V. Vesely, U. Wideqvist and R. Westerholm. 2002. "Chemical and physical characterization of emissions from birch wood combustion in a wood stove". *Atmospheric Environment,* vol. 36, n° 30, p. 4823-4837.

Hinds, W. C. 1999. *Aerosol technology: properties, behavior, and measurement of airborne particles*, 2nd. ed. United States : Wiley-Interscience, New York, N.Y., 483 p.

Hueglin, Ch., Ch. Gaegauf, S. Kunzel and H. Burtscher. 1997. "Characterization of Wood Combustion Particles: Morphology, Mobility, and Photoelectric Activity". *Environ. Sci. Technol.,* vol. 31, n° 12, p. 3439-3447.

Hughes, W. F., and J. A. Brighton. 1999. *Schaum's Outline of Theory and Problems of Fluid Dynamics*, 3rd. ed. New York : McGraw-Hill, 391 p.

Jaworek, A., A. Krupa and T. Czech. 2007. "Modern electrostatic devices and methods for exhaust gas cleaning: A brief review". *Journal of Electrostatics,* vol. 65, n° 3, p. 133-155.

Johansson, L. S., C. Tullin, B. Leckner and P. Sjovall. 2003. "Particle emissions from biomass combustion in small combustors". *Biomass and Bioenergy,* vol. 25, n° 4, p. 435-446.

Johansson, L. S., B. Leckner, L. Gustavsson, D. Cooper, C. Tullin and A. Potter. 2004. "Emission characteristics of modern and old-type residential boilers fired with wood logs and wood pellets". *Atmospheric Environment,* vol. 38, n° 25, p. 4183-4195.

Khalil, M. A. K. and R. A. Rasmussen. 2003. "Tracers of wood smoke." *Atmospheric Environment*, vol. 37, n° 9-10, p. 1211-1222.

Kirsch, A. A. and A. V. Zagnit'ko. 1990. "Field Charging of Fine Aerosol Particles by Unipolar Ions". *Journal of Aerosol Science,* vol. 21, p. 465-470.

Kleeman, M. J., J. J. Schauer and G. R. Cass. 1999. "Size and Composition Distribution of Fine Particulate Matter Emitted from Wood Burning, Meat Charbroiling, and Cigarettes". *Environ. Sci. Technol.,* vol. 33, n^{o} 20, p. 3516-3523.

Larson, T., T. Gould, C. Simpson, J. Liu, C. Claiborn and J. Lewtas. 2004. "Source apportionment of indoor, outdoor, and personal PM2.5 in Seattle, Washington, using positive matrix factorization.". *J. Air Waste Manage. Assoc.,* vol. 54, n^{o} 9, p. 1175-1187.

Lawless, P. A. 1996. "Particle charging bounds, symmetry relations, and an analytic charging rate model for the continuum regime". *Journal of Aerosol Science,* vol. 27, n^{o} 2, p. 191-215.

Lecomte, E. L., A. W. Pang and J. W. Russell. 1998. "Ice storm '98". Institute for Catastrophic Loss Reduction. Research Paper Series no 1, Toronto, 37 p.

McDonald, J. D., B. Zielinska, E. M. Fujita, J. C. Sagebiel, J. C. Chow and J. G. Watson. 2000. "Fine Particle and Gaseous Emission Rates from Residential Wood Combustion". *Environmental Science & Technology,* vol. 34, n^{o} 11, p. 11.

McKendry, P. 2002. "Energy production from biomass (part 1): overview of biomass." *Bioresource Technology*, vol. 83, n^{o} 1, p 37 - 46.

Naeher, L. P., M. Brauer, M. Lipsett, J. T. Zelikoff, C. D. Simpson, J. Q. Koenig and K. R. Smith. 2007. "Woodsmoke Health Effects: A Review". *Inhalation Toxicology,* vol. 19, n^{o} 1, p. 67 - 106.

Natural Resources Canada. 2010. *Energy Use Data Handbook, 1990 - 2007*. Energy publications, Office of Energy Efficiency, 160 p.

Oglesby, S., and G. B. Nichols. 1970. *A Manual of Electrostatic Precipitator Technology : Part 1 - Fundamentals.* . PB 196 380. Birmingham, Alabama : Southern Research Institute ; National Technical Information Service, U.S. Dept. of Commerce, 322 p.

Ounis, H., G. Ahmadi and J. B. McLaughlin. 1991. "Brownian Diffusion of Submicrometer Particles in the Viscous Sublayer. ". *Journal of Colloid and Interface Science,* vol. 143, n^{o} 1, p. 266-277.

Parker, K. R. 2000. "Effective capture of respirable-sized particulates using electrostatic precipitator technology". *Engineering Science and Education Journal*, (February), p. 33-40.

Pauthenier, M. M., and M. Moreau-Hanot. 1932. "Charging of Spherical Particles in an Ionizing Field". *J. Phys. Radium,* vol. 3, p. 590-613.

Peek, F. W. 1929. *Dielectric Phenomena in High Voltage Engineering*. New York : McGraw-Hill.

Perry, R.H. and D. W. Green. 1984. *Perry's Chemical Engineers' Handbook*. 4th ed. New York : McGraw-Hill.

Schauer, J. J., M. J. Kleeman, G. R. Cass and B. R. T. Simoneit. 2001. "Measurement of Emissions from Air Pollution Sources. 3. C1-C29 Organic Compounds from Fireplace Combustion of Wood". *Environmental Science & Technology,* vol. 35, n° 9, p. 1716-1728.

Schmatloch, V., and S. Rauch. 2005. "Design and characterisation of an electrostatic precipitator for small heating appliances". *Journal of Electrostatics,* vol. 63, n° 2, p. 85-100.

Schmid, H-J. 2003. "On the modelling of the particle dynamics in electro-hydrodynamic flow fields: II. Influences of inhomogeneities on electrostatic precipitation". *Powder Technology,* vol. 135-136, p. 136-149.

Shih, T.H., W. W. Liou, A. Shabbir, Z. Yang, and J. Zhu. 1995. "A New k-ε Eddy-Viscosity Model for High Reynolds Number Turbulent Flows - Model Development and Validation". *Computers Fluids*, vol. 24, n° 3, p. 227-238.

Skodras, G., S. P. Kaldis, D. Sofialidis, O. Faltsi, P. Grammelis and G. P. Sakellaropoulos. 2006. "Particulate removal via electrostatic precipitators -- CFD simulation". *Fuel Processing Technology,* vol. 87, n° 7, p. 623-631.

Straif, K., R. Baan, Y. Grosse, B. Secretan, F. El Ghissassi and V. Cogliano. 2006. "Carcinogenicity of household solid fuel combustion and of high-temperature frying". *The Lancet Oncology,* vol. 7, n° 12, p. 977-978.

United States EPA. 1988. *40 CFR 60, subpart AAA, Standards of Performance for New Residential Wood Heaters*, U.S. Government Printing Office.

United States EPA. 2006. National Ambient Air Quality Standards. *Federal Register*, vol. 71, n° 200, p. 61144.

Vallero, D. A. 2008. *Fundamentals of Air Pollution*, 4th ed. Amsterdam : Elsevier, 942 p.

Wark, K., and C. F. Warner. 1981. *Air pollution : its origin and control,* 2nd. ed. New York, N.Y. : HarperCollins., 526 p.

Watanabe, T. 1989. "Calculation of fly ash particle motion and its migration velocity in an electrostatic precipitator". In *Industry Applications Society Annual Meeting, 1989., Conference Record of the 1989 IEEE*. p. 2126-2136 vol.2.

Waters, R. T., and W. B. Stark. 1975. "Characteristics of the stabilized glow discharge in air". *J. Phys. D: Appl. Phys.,* vol. 8, p. 416-426.

Wendt, J. F. 1995. *Computational Fluid Dynamics - An Introduction*, 2nd ed.. Berlin : Springer, 297 p.

Zhuang, Y., Y. J. Kim, T. G. Lee and P. Biswas. 2000. "Experimental and theoretical studies of ultra-fine particle behavior in electrostatic precipitators". *Journal of Electrostatics,* vol. 48, nº 3-4, p. 245-260.